



Max-Planck-Institut für Intelligente Systeme
(ehemals Max-Planck-Institut für Metallforschung)
Stuttgart

Kinetics of phase transformations

Bastian F. Rheingans

Dissertation
an der
Universität Stuttgart

Bericht Nr. 250
Februar 2015

Kinetics of Phase Transformations

Von der Fakultät Chemie der Universität Stuttgart zur Erlangung der
Würde eines Doktors der Naturwissenschaften (Dr. rer. nat.)
genehmigte Abhandlung

vorgelegt von
Bastian F. Rheingans
aus Backnang

Hauptberichter
Mitberichter
Prüfungsausschussvorsitzender

Prof. Dr. Ir. E. J. Mittemeijer
Prof. Dr. Dr. h.c. G. Schmitz
Prof. Dr. Th. Schleid

Tag der mündlichen Prüfung

17.02.2015

INSTITUT FÜR MATERIALWISSENSCHAFT DER UNIVERSITÄT STUTT GART
MAX-PLANCK-INSTITUT FÜR INTELLIGENTE SYSTEME
(EHEMALS MAX-PLANCK-INSTITUT FÜR METALLFORSCHUNG)
2015

Contents

1	Introduction	11
1.1	Kinetics of phase transformations	11
1.2	Modelling of phase transformation kinetics	12
1.2.1	Nucleation and growth	12
1.2.2	The kinetics of nucleation and growth	12
1.2.3	Modelling of concurring nucleation and growth	14
1.2.4	Application of kinetic models to experimental data	15
1.3	General scope of the thesis	17
1.4	Kinetic models	18
1.4.1	The modular approach	18
1.4.2	KWN-type kinetic models	21
1.5	Experimental systems	21
1.5.1	Metallic glasses	21
1.5.2	Precipitation reactions	22
1.6	Overview of the thesis	23
2	The Kinetics of the Precipitation of Co from Supersaturated Cu-Co Alloy	25
2.1	Introduction	26
2.2	Theoretical background of transformation kinetics	27
2.3	Experimental	31
2.4	Results and evaluation	33
2.4.1	Differential scanning calorimetry	33
2.4.2	TEM and HRTEM	34
2.4.3	Analysis of transformation kinetics	35
2.5	Discussion	41
2.6	Conclusions	44

3	Crystallisation Kinetics of Fe₄₀Ni₄₀B₂₀ Amorphous Alloy	47
3.1	Introduction	48
3.2	Experiments	49
3.3	Theoretical background	50
3.4	Results and data evaluation	53
3.4.1	DSC data evaluation	53
3.4.2	Phase analysis and microstructural evolution	54
3.4.3	Kinetic analysis	57
3.5	Discussion	62
3.6	Conclusions	67
4	Phase Transformation Kinetics; Advanced Modelling Strategies	69
4.1	Introduction	70
4.2	The modular model approach	72
4.3	Time dependency of kinetic parameters: modelling of the crystallisation of amorphous Fe ₄₀ Ni ₄₀ B ₂₀	74
4.4	Dedicated, specific descriptions for the nucleation and growth modes: modelling of the hcp → fcc transformation in Co	80
4.5	Incorporation of microstructural information: modelling of the precipitation kinetics of Co in CuCo	83
4.6	Conclusion	86
5	Modelling Precipitation Kinetics: Evaluation of the Thermodynamics of Nucleation and Growth	87
5.1	Introduction	87
5.2	Theoretical background	91
5.3	Usage of the common stability consideration upon numerical evaluation of nucleation and growth thermodynamics	99
5.4	Example	105
5.5	Conclusions	107

6	Analysis of Precipitation Kinetics on the Basis of Particle-Size Distributions	111
6.1	Introduction	112
6.2	Theoretical background	114
6.2.1	Kinetic model	114
6.2.2	Model application	118
6.3	Model implementation	119
6.4	Experimental procedure	122
6.5	Experimental results	125
6.6	Modelling results and discussion	128
6.6.1	General model behaviour	128
6.6.2	Influence of the thermodynamic description	131
6.6.3	Limitations of kinetic model fitting to averaged experimental data	133
6.6.4	Independent variation of nucleation and growth kinetics; utilising the full PSDs at different temperatures	135
6.6.5	Predictive capability; limitations	141
6.7	Conclusions	144
7	Summary	145
7.1	Summary in the English language	145
7.2	Zusammenfassung in deutscher Sprache	152
	Bibliography	161
	List of Publications	
	Danksagung	
	Curriculum Vitae	
	Erklärung über die Eigenständigkeit der Dissertation	

Chapter 1

Introduction

1.1 Kinetics of phase transformations

Phase transformations are ubiquitous in the world: They partake in natural phenomena such as cloud formation – involving the precipitation of water droplets from air supersaturated with H_2O -molecules, or the freezing of water – involving the transition of water from a liquid phase into a solid phase, as well as in techniques developed by humans such as age-hardening of alloys – involving the precipitation of solute-rich particles from a matrix supersaturated in solute, or selective laser melting – involving the rapid melting and re-solidification of an alloy. The primary technological relevance of phase transformations (and also the challenge therein) lies in the changes in the microstructure of the material upon phase transformation and the associated changes of its properties. Understanding and control of the kinetics of the phase transformation, i.e. the progress of the phase transformation as function of time, therefore play a crucial role for optimising the properties of a material [1].

The analysis of the kinetics of a phase transformation can be performed on different length scales, time scales and with different levels of refinement, ranging from atomistic simulations over simulations on the mesoscopic or macroscopic scale to mean-field kinetic models [2],¹ with the choice of a specific method for kinetic analysis strongly depending on the purpose of the analysis. In this thesis, the kinetics of solid-state phase transformations are described employing mean-field kinetic models. These models provide a (usually relatively simple and numerically efficient) description for the evolution of certain characteristic average parameters of the microstructure, e.g. the evolution of the transformed fraction or of the number and size of product-phase particles, as a function of the time t and of externally controlled parameters (most commonly of the temperature T), based on the assumption of certain *transformation mechanisms*. The focus of this thesis lies on the development of new strategies for kinetic modelling using mean-field kinetic models, combined with dedicated experimental investigations of phase transformation kinetics in

¹Also see [2] for the various different definitions of the terms *model* and *simulation*.

different model systems.

1.2 Modelling of phase transformation kinetics

1.2.1 Nucleation and growth

Phase transformation in the solid state are mostly of heterogeneous nature, i.e. a clear distinction between parent and product phase (or phases) can be made in all stages of the reaction [3]. The kinetics of these transformations are generally treated in terms of two separate transformation mechanisms: the *nucleation* of product-phase particles and their subsequent *growth*, each associated with a certain time-dependency, expressed in a kinetic rate equation.

This distinction between particle nucleation and particle growth upon kinetic modelling originates from a consideration of thermodynamic stability of a product phase particle as function of its size [4]: The phase transformation is promoted by a release of energy, as provided by a change in crystal structure and/or chemical composition of the phases. This energy release, often termed the driving force² for transformation, scales with the volume of the product particle. On the other hand, formation of a product particle is associated with an energy increase owing to the formation of an interface between nucleating particle and parent phase (and the potential generation of other defects), with an energy contribution which scales with a lower dimensionality of the particle and thus dominates the energy balance for small particle size. As a consequence, a critical size, corresponding to an energy³ barrier ΔG^* for nucleation, exists below which the nucleating particle is unstable. Hence, *particle nucleation* considers the formation of a product-phase particle of critical size and *particle growth* the subsequent growth⁴ of a particle once it has surpassed the critical size.

1.2.2 The kinetics of nucleation and growth

The formation of a nucleus is considered as resulting from short-range fluctuations (e.g. in structure or in composition) associated with an increase of total energy, which allow the system to overcome the energy barrier ΔG^* for nucleation [3]. To describe the kinetics of nucleation, i.e. the emergence of new product-phase particles as function of time, in the classical kinetic theory

²The term “driving force” is a relatively vague notion; its meaning e.g. depends on how the initial state and the final state of the transformation (step) is defined (see, e.g., the definition of the driving force for nucleation in Chapter 5).

³Within this thesis, the Gibbs energy/free enthalpy is used as the thermodynamic potential function due to the typical experimental control of temperature and pressure.

⁴in some cases also shrinkage, cf. Chapter 5 and 6 of this thesis.

of nucleation [5, 6] the energy barrier ΔG^* is translated into a certain probability for formation of a particle of critical size and into a rate \dot{N} of particle nucleation.

By considering the step-wise clustering of single atoms (or molecules) the well-known dependency

$$\dot{N} \propto \exp\left(-\frac{\Delta G^*}{kT}\right) \quad (1.1)$$

of the nucleation rate on the nucleation barrier is obtained, where T is the absolute temperature and $k = R/N_A$ is the Boltzmann constant (R : ideal gas constant, N_A : Avogadro's constant). Owing to the exponential dependency of \dot{N} on ΔG^* , the nucleation rate is very sensitive towards changes in the nucleation barrier (and thus towards changes in the driving force [7]). The consideration of nucleus formation by individual addition steps leads to a second temperature-dependent term of the nucleation rate accounting for the thermal activation of the elemental addition step upon nucleation:

$$\dot{N} \propto \exp\left(-\frac{\Delta G^*}{kT}\right) \times \exp\left(-\frac{Q_N}{RT}\right), \quad (1.2)$$

where Q_N is the activation energy associated with the elemental addition step, often termed as activation energy for nucleation.⁵

Classical nucleation theory describes particle nucleation as the outcome of a statistical, random process of clustering of individual atoms or molecules. Especially in the solid state, the preconditions for such a process almost never hold [8], or the concept of clustering is simply not applicable: nucleation of a product-phase particle can be facilitated by the presence of defects in the parent phase, or may occur via different transient stages, or may start from sub-critical nuclei already present in the parent phase, etc. For kinetic modelling in practice, this leads to a plethora of different approaches used to describe the kinetics of nucleation, some originating from considerations similar to classical nucleation theory, some of more phenomenological nature.

In contrast to the probabilistic treatment of particle nucleation in the classical theory of nucleation, the growth of a particle after surpassing the critical size is usually described as a deterministic process.⁶ Descriptions for particle

⁵The term ‘‘activation energy’’ is sometimes also used for the nucleation barrier ΔG^* , or for a combination of ΔG^* and Q_N ; this type of activation energy is then evidently also a function of the driving force.

⁶In some cases, the abrupt transition from a probabilistic description of particle nucleation to a deterministic description of particle growth is a rather artificial concept (e.g. in the above presented case of particle formation by clustering of solute atoms; cf. e.g. cluster dynamics models [9]); however, this assumption strongly facilitates the modelling of the particle growth kinetics.

growth kinetics therefore generally show a different dependency on the driving force (and on the other energy contributions associated with the formation of the product-phase particle) than corresponding descriptions for particle nucleation kinetics and are generally less sensitive towards changes therein.

However, similar to the elemental addition step in classical nucleation theory, kinetic rate equations for particle growth generally also consider a thermally activated process with an Arrhenius-type temperature dependency:

$$v \propto \exp\left(-\frac{Q_G}{RT}\right), \quad (1.3)$$

where v is the growth rate and Q_G is the (constant) activation energy of growth.

In presence of high driving forces, e.g. in case of highly undercooled phases, the influence of the driving force on the temperature-dependency of the nucleation kinetics and growth kinetics is often considered as being negligible; in this case, both nucleation rate and growth rate reduce to simple, Arrhenius-type rate equations with constant activation energy Q [1].

1.2.3 Modelling of concurring nucleation and growth

Kinetic rate equations for particle nucleation and particle growth as introduced above may directly be employed to describe the nucleation kinetics and the growth kinetics of particles in absence of interference of other particles. This condition can only be maintained in the (very) early stages of the transformation. In order to arrive at kinetic models covering the entire range of the transformation reaction, the kinetic descriptions of particle nucleation and particle growth must be implemented into a common framework which accounts for the particle interference, i.e. for the finiteness of the parent phase.

This can for instance be done by implementing the kinetic rate equations in a spatially resolved, three-dimensional model/simulation, or by use of mean-field approaches which replace the direct, spatial interaction of particles with the interaction of an individual particle (or of a class of particles) with a parent phase of average properties. Obviously, mean-field kinetic models are much simpler and much faster to apply than three-dimensional simulations, often even providing closed, analytic expressions for the transformation kinetics. However, this comes at the price of losing all spatially resolved information on the parent and product microstructure (see e.g. [10]).

In this thesis, kinetic models featuring two different types of mean-field approaches are employed, with product particles either interacting with a parent phase of average degree of transformation (mean-field transformed fraction ap-

proach) or interacting with a parent phase providing an average driving force for transformation (mean-field driving force approach). The first approach is followed in the so-called modular model for transformation kinetics ([11], see Section 1.4.1), a generalisation of the classical JMAK-(Johnson-Mehl-Avrami-Kolomogorov)-equation [12–14]: Nucleation and growth of product phase particles is first assumed to proceed in an infinitely large parent phase, i.e. without particle interference (and thus without a dependency of the rate equations on the progress of the transformation), yielding the so-called extended volume fraction x_e . The change df in the actually transformed volume fraction f is then obtained by application of an impingement correction

$$df = (1 - f) \times dx_e, \quad (1.4)$$

accounting for the fact that particle nucleation and particle growth cannot proceed in already transformed volume (see Figure 1.1).

In the second type of model, a Kampmann-Wagner numerical (KWN)-type [15] multi-class model (see Section 1.4.2), employed to describe the precipitation kinetics of solute-rich particles from a supersaturated parent phase, the rate equations for nucleation and growth are directly and individually dependent on the average chemical driving force, which itself depends on the average solute content of the parent phase. The main difference of the two mean-field kinetic models thus lies in the way the nucleation kinetics and the growth kinetics are implemented into the mean-field approach (a more detailed discussion of the two models is given in Sections 1.4.1 and 1.4.2).

1.2.4 Application of kinetic models to experimental data

The actual usage of a kinetic model strongly depends on the way the model has been formulated [16]: If the kinetics of nucleation and of growth can entirely be expressed in terms of established theories, of basic physical principles and processes (e.g. thermodynamic models, elastic theory, volume diffusion of solute atoms, movement of dislocations, etc.), the model may directly provide a description of the transformation kinetics. The comparison of kinetic model prediction and experiment then indicates whether the mechanisms presumed for nucleation and growth do indeed hold (naturally, the goodness of the model description then also depends on the quality of the external input data).

However, kinetic models often include a number of parameters which are either not available from external sources (i.e. from (model-)independent experimental data or theoretical calculations) – also in case that the parameters lack direct correspondence to a basic physical process or quantity – or have no (clearly definable) physical meaning.

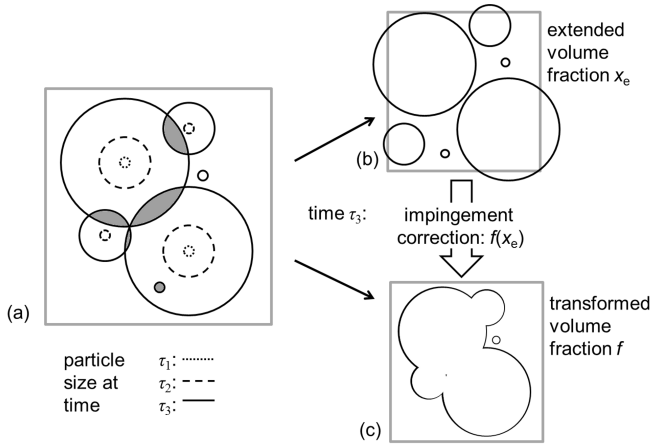


Figure 1.1: A schematic representation of the impingement approach: Particles are first assumed to nucleate and grow without the interference of other particles, i.e. in an infinitely large parent phase (a). This yields the extended transformed volume fraction x_e (b). The impingement relation then corrects for the interference of article (the grey areas at $t = \tau_3$ in (a)), yielding the transformed volume fraction $f(x_e)$ in finite space (c).

In such situations, the kinetic model is fitted to the experimental data using the unknown model parameters as adaptable fit parameters (see example in Figure 1.2). The model fit then yields a set of parameters which characterises the kinetics of the phase transformation within the framework of the chosen model. The values of the kinetic model parameters obtained upon model fitting can provide more or less insight into the mechanisms of the transformation, depending on the nature of the model: an activation energy for growth may for instance be associated with the activation energy for diffusion in case of particle growth controlled by volume diffusion of one component, or may only constitute some average quantity characterising the thermal activation for the advancement of an interface in case of growth of a multi-phase product particle.⁷ In the extreme case, the kinetic model parameters have no physical meaning at all and the kinetic model solely provides an empirical description of the experimental data allowing to some extent a prediction for the phase

⁷In some situations, atomistic kinetic simulations can be employed to bridge the gap between a basic physical process, e.g. the jumps of single atoms through the the interface region, and the macroscopic transformation mechanism, e.g. the net movement of the interface [17]; the atomistic simulation can then be seen as a “computer experiment”, or as the atomistic part of a multi-scale kinetic model [2].

transformation kinetics under modified external conditions, e.g. for a somewhat different temperature treatment (which can yet be sufficient, e.g. for control of a technical process involving a phase transformation).

A potential problem of kinetic model fitting is that the kinetic model fit may actually be an under-constrained fit, i.e. that the kinetic model can provide descriptions of the experimental data of same quality, but with entirely different sets of kinetic model parameters. Such under-determination of the model fit can for instance occur when the model is applied to experimental data which does not convey sufficient information to uniquely determine all kinetic model parameters. However, under-determination of the kinetic model can also be already inherently present in the kinetic model description, e.g. when the originally separate expressions for the kinetics of particle nucleation and for particle growth as function of t and T , each with separate kinetic model parameters, can be simplified to a single expression as function of t and T , with combined, effective model parameters (cf. Figure 1.2). A typical example is the classical JMAK-equation for isothermal transformation kinetics ([12–14], also see Section 1.4.1): although the kinetic model is derived under the assumption of nucleation-and-growth-processes, the model characterises the transformation kinetics only by a set of effective model parameters – an effective activation energy Q_{eff} (and a corresponding pre-exponential factor) and an effective growth exponent n (Figure 1.2). The kinetic model description does then no longer convey separate information on nucleation kinetics and growth kinetics and is consequently not capable to describe and predict the evolution of size and number density of the product particles.

1.3 General scope of the thesis

In the framework of this thesis, the kinetics of heterogeneous phase transformations in different prototype experimental systems are analysed employing mean-field kinetic models. The underlying theme is the development of new strategies for kinetic modelling, focusing on the interrelation between the kinetic model description and the amount of available experimental information, on the interpretation of kinetic model parameters determined upon kinetic model fitting, and on the coupling of kinetic models to external input data, e.g. thermodynamic data.

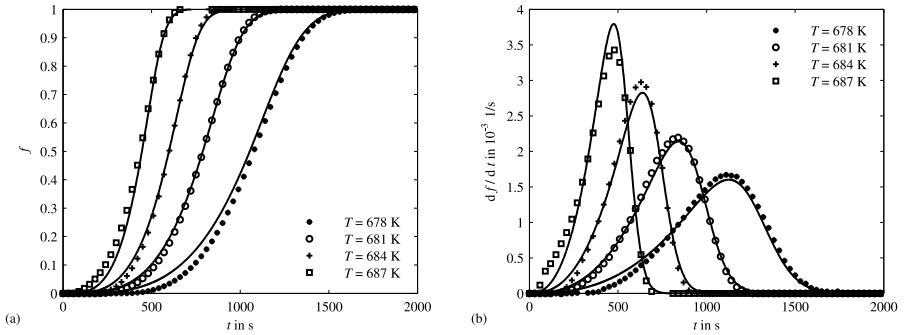


Figure 1.2: Example of a model fit to experimental data for the evolution of the transformed fraction $f(t)$ (a) and transformation rate df/dt (b) upon isothermal annealing of a metallic glass at different temperatures (markers: experimental data; lines: model fit). The here applied JMAK-like model description is based on the modular approach (see Section 1.4.1) with constant, effective kinetic model parameters: an effective activation energy Q_{eff} , a pre-exponential factor K_0 and a growth exponent n (also see Chapter 3).

1.4 Kinetic models

1.4.1 The modular approach

The modular approach for transformation kinetics [11] is a mean-field transformed fraction model which originates from, and generalises, the classical JMAK-model developed by Kolmogorov [12], and independently by Johnson and Mehl [14], and Avrami [13, 18, 19]. In this type of model, nucleation and growth of particles is in a first step considered as occurring in an infinitely large parent phase (Figure 1.1; cf. Section 1.2.3). The transformed fraction accounting for the finiteness of the parent phase is then obtained by application of an impingement correction, e.g. Equation (1.4), which relates the transformed volume fraction x_e of particles in the extended space to their transformed fraction f in finite space. By integration of Equation (1.4), pertaining to the case of a random spatial distribution of nucleation sites and isotropic particle growth, the relation

$$f = 1 - \exp(-x_e) \quad (1.5)$$

can be derived (for cases of non-random nucleation and non-isotropic growth, modified expressions of the impingement correction exist [11]). The classical

JMAK-equation for isothermal transformations is obtained for

$$x_e = (Kt)^n = \left(K_0 \exp \left(-\frac{Q_{\text{eff}}}{RT} \right) \right)^n \times t^n, \quad (1.6)$$

with the growth exponent n and the rate constant $K = K_0 \exp \left(-\frac{Q_{\text{eff}}}{RT} \right)$, where K_0 is a temperature-independent constant and Q_{eff} the effective activation energy. Similar expressions can be derived for the case of isochronal heating ([20], also see [11]).

Equation (1.6) is strictly valid only for a constant, Arrhenius-type nucleation rate, or a constant number of nuclei already present at the beginning of the reaction, and in presence of high driving forces [1]. To relieve these limitations, the extended volume fraction can be expressed in a general way (see [13] and [21]) as

$$x_e(t) = \int_0^t \dot{N}(\tau) Y(t, \tau) d\tau, \quad (1.7)$$

with the nucleation rate $\dot{N}(\tau)$ at time τ and the volume $Y(t, \tau)$ of a growing particle at time t nucleated at time τ , thus allowing to introduce various different expressions for particle nucleation and particle growth. The volume of a particle is obtained from

$$Y(t, \tau) = g \left(\int_{\tau}^t v dt' \right)^{d/m} \quad (1.8)$$

with v as the velocity (coefficient) of the advancing interface, d as the dimensionality of growth, m as the growth mode parameter and g as a shape factor. The expression $\int_{\tau}^t v dt'$ describes the one-dimensional size of the product particle (e.g. the radius r of a spherical particle) as function of time. The parameter m can be adapted to different types of growth kinetics: For $m = 1$, a linear growth law is obtained, i.e. the size of the particle increases proportional to time t in one dimension, and for $m = 2$, a parabolic growth law is obtained, i.e. the size of the particle increases proportional to $t^{1/2}$ in one dimension (at constant temperature).

Equations (1.7) and (1.8), together with an appropriate impingement correction, constitute the *modular kinetic model* [11], which provides a flexible

framework for modelling transformation kinetics: The modular approach allows to easily combine various different expressions of particle nucleation rates (also combining different modes of nucleation) and particle growth rates to describe the presumed mechanisms of nucleation and growth. In case of mathematically simple expressions for the nucleation rate and growth rate, such as Arrhenius-type rate equations, the transformed fraction $f(t)$ can often be expressed in a closed form similar to the classical JMAK-equation (Equation (1.5) + (1.6)) with effective (but now not necessarily constant) kinetic model parameters Q_{eff} , n and K_0 [11]. However, the flexible framework of the modular approach also allows to incorporate kinetic rate equations derived from dedicated theories for the mechanisms of nucleation and growth.

Owing to the application of a particle impingement correction for calculating the transformed fraction (Equation 1.5), model descriptions within the modular approach (and other models deriving from the classical JMAK-approach) are most suitable if direct impingement of particles does indeed occur.⁸ This condition is, for instance, clearly not fulfilled in case of precipitation of solute-rich particles from a matrix phase initially supersaturated in solute. Upon formation of the solute-rich particle, the surrounding matrix is gradually depleted of solute (thus sooner or later leading to growth of the particle controlled by long-range volume diffusion of the solute components through the matrix). Particles then do not interact directly (so-called “hard impingement”), but via their surrounding, eventually overlapping diffusion fields (so-called “soft impingement”). In the framework of the impingement correction approach, this case can be approximated by considering “hard impingement” of particles including their solute-depleted shells, as done in Chapter 2 of this thesis; and more sophisticated soft-impingement models are being developed ([22, 23], also see already [24]). However, a general drawback of mean-field kinetic models based on the impingement approach remains: the impingement correction, transferring the extended volume fraction x_e into the transformed volume fraction f , is applied *equally* to nucleation and growth. This makes current models based on the impingement approach less adequate to describe the kinetics of phase transformations which include a separate, prolonged stage of particle growth (and coarsening) after the cease of particle nucleation, as is indeed often observed for precipitation reactions (cf. the discussion on the influence of the driving force on nucleation kinetics and growth kinetics in Section 1.2.2).

⁸This also implies a clear distinction between transformed volume (“zero driving force” and thus zero nucleation rate and zero growth rate) and untransformed volume (“constant driving force”, and thus constant nucleation rate and constant growth rate).

1.4.2 KWN-type kinetic models

A frequently used type of kinetic model to describe the kinetics of precipitation reactions originates from the Kampmann-Wagner numerical (KWN)-approach [15] which uses a mean-field approximation for the matrix composition (cf. Section 1.2.3): In this type of model, the evolution of the particle size distribution (PSD) of precipitate particles is computed for discrete time steps and discrete particle-size classes (so-called multi-class approach) using kinetic rate equations for particle nucleation and particle growth based on the classical theory of nucleation [5,6] and growth of spherical particles controlled by long-range volume diffusion of the solute component(s) [25,26], respectively. KWN-type models are thus models specialised on the description of precipitation kinetics (in contrast to the flexible modelling approach followed in the modular model, Section 1.4.1).

Both kinetic rate equations are functions of the mean matrix composition, i.e. of the average chemical driving force, and thus explicitly depend on the thermodynamics of the alloy system. In case of particle nucleation, this dependency is (mainly) expressed in the nucleation barrier ΔG^* (see Section 1.2). In case of particle growth the dependency is introduced by incorporation of the Gibbs-Thomson (or capillarity) effect, i.e. the (equilibrium) compositions of the particle phase and the matrix phase at the particle-matrix interface are functions of the size of the particle.

1.5 Experimental systems

1.5.1 Metallic glasses

Metallic glasses, i.e. metallic alloys featuring only short-range atomic ordering but no long-range ordering, can show outstanding physical and mechanical properties owing to the absence of crystallinity and of defects such as grain boundaries and dislocations associated with the crystalline state [27,28].

In some cases, a partial crystallisation of the amorphous alloy can considerably improve the performance of a metallic glass [27]. However, the crystallisation reaction can also serve as an excellent experimental model system for testing of kinetic models: the amorphous alloy represents a homogeneous, isotropic parent phase, and nucleation of crystalline particles (in the bulk of the metallic glass) can be assumed to occur randomly, while particle growth is not influenced by anisotropy of the parent phase or by presence of large-scale defects such as grain boundaries or dislocations in the parent phase. This is, of course, a highly idealised image: metallic glasses can indeed show defects such as voids and nano-sized crystallites, show different degrees of short-range

or medium-range ordering, or show localised variations in composition etc., which all can strongly affect the kinetics of the crystallisation reaction.⁹ The extent of such deviations from an ideal amorphous state strongly depends on the preparation process of the metallic glass and the further treatment of the material. Kinetic analysis of the crystallisation reaction therefore often yields more or less arbitrary kinetic model parameters which only pertain the experimentally determined transformation kinetics of the material at hand.

In this thesis, the crystallisation kinetics of amorphous $\text{Fe}_{40}\text{Ni}_{40}\text{B}_{20}$ upon isothermal annealing is investigated. Power-compensating differential scanning calorimetry (DSC) is employed to measure the time-dependent heat release upon crystallisation, providing access to the evolution of the transformed fraction as function of time and annealing temperature. The kinetic analysis is supported by an investigation of the microstructure evolving upon crystallisation by use transmission electron microscopy and by X-ray diffraction analysis for phase analysis.

1.5.2 Precipitation reactions

Precipitation reactions are among the technologically most important phase transformations utilised to improve materials properties [1]. In this thesis, the precipitation kinetics of Co-rich particles from dilute Cu-Co alloys are investigated. The peritectic system Cu-Co represents an ideal case for studying precipitation reactions in the solid state: the composition-temperature phase diagram shows a large miscibility gap with sufficient solubility of Co in fcc Cu at high temperatures [29]. Upon quenching dilute Cu-Co-alloys into the two-phase region, spherical Co-rich particles of fcc structure are formed within the fcc Cu-rich matrix. Owing to the small lattice mismatch between fcc Cu and fcc Co, the precipitate particles are initially fully coherent with the surrounding matrix [30] (see Figure 1.3). Such properties lead to frequent use of the system Cu-Co for testing of kinetic models and application of newly developed experimental analysis methods (e.g. [8, 31–43]).

In the framework of this thesis, the kinetics of precipitation in Cu-Co are investigated in two fundamentally different types of experiments: In one case, the precipitation reaction in a quenched Cu-1 at.% Co alloy upon isochronal heating is investigated by means of DSC, complemented by a TEM analysis of the final microstructure (Chapter 2). This type of experiment allows to investigate the precipitation kinetics in presence of (initially) very high driving forces and at low temperatures, i.e. under conditions where the kinetics

⁹Moreover, crystallisation reactions of metallic glasses are generally prone to follow complicated kinetic pathways owing to the large number of chemical components involved and the (usually) quite high driving forces for crystallisation.

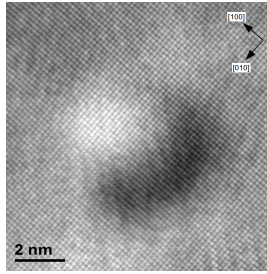


Figure 1.3: High-resolution transmission electron microscopy image of a Co-rich precipitate particle formed in a Cu-rich matrix. The particle shows full coherency with the surrounding matrix (cf. Chapter 2).

are supposed to be dominated by the thermal activation of the diffusional movement of solute atoms. In the second case, the precipitation reaction in a quenched Cu-0.6 at.% Co alloy upon isothermal annealing at high temperatures, i.e. at low degrees of supersaturation and thus for low driving forces, is followed using TEM (Chapter 6).

1.6 Overview of the thesis

In Chapters 2 to 4, application of the modular model to experimental data for different types of phase transformations is presented, focusing on different aspects of model application:

In **Chapter 2**, the modular model approach is employed to describe the precipitation kinetics in Cu-1 at.% Co upon isochronal heating. In order to obtain separate kinetic descriptions for the nucleation kinetics and growth kinetics upon employing the modular model in a JMAK-type mode, quantitative information on the microstructure – the number density of precipitate particles as determined with TEM – is directly implemented into the kinetic model. This allows to separately determine the activation energies for nucleation and growth within the framework of the modular model.

Chapter 3 deals with the crystallisation of amorphous $\text{Fe}_{40}\text{Ni}_{40}\text{B}_{20}$ upon isothermal annealing: The experimental data in form of the evolution of the transformed volume fraction at different temperatures, derived from DSC measurements, only allows determination of effective kinetic model parameters. By artificially altering the crystallisation kinetics, applying a pre-annealing treatment to the amorphous alloy at low temperatures (cf. [21]), a second experimental dataset containing additional kinetic information is generated. Simultaneous fitting of the kinetic model to both datasets again allows to

determine separate kinetic model parameters for nucleation and growth.

Chapter 4 presents a review of the experimental studies in Chapter 2 and Chapter 3 with focus on practical application of the modular modelling approach for kinetic analysis. Additionally, an example for employing the modular model as a flexible framework for case-specific, dedicated expressions of the kinetic rate equations is given [44].

Chapters 5 and 6 focus on the kinetic modelling of precipitation reactions:

In **Chapter 5**, the problem of inconsistent usage of thermodynamic models for nucleation and growth upon modelling of precipitation kinetics, as frequently occurring in KWN-type kinetic models, is addressed. It is shown how typical approaches for separate treatment of nucleation barrier and Gibbs-Thomson effect can be retraced to a common underlying consideration of thermodynamic equilibrium, as already discussed by Gibbs in [4], but most frequently ignored. For typical assumptions introduced upon kinetic modelling of precipitation reactions, a numerically highly efficient method to consistently implement thermodynamic data for the chemical driving force, as e.g. derived from a thermodynamic assessment of the alloy system, into the kinetic model is developed.

In the last part, **Chapter 6**, an analysis of the precipitation kinetics of Co-rich particles in a Cu-0.6 at.% Co alloy upon isothermal annealing is presented, applying the numerically efficient method for thermodynamic evaluation introduced in Chapter 5: The evolution of the particle-size distribution of Co-rich particles at different annealing temperatures, determined by TEM, is modelled using a KWN-type kinetic model. It is investigated how thermodynamic models of different accuracy affect the behaviour of the kinetic model and to which extent the amount of experimental kinetic data present in the time-evolution of the PSDs at different temperatures allows to determine unique, physically plausible values for the kinetic model parameters.

Chapter 2

The Kinetics of the Precipitation of Co from Supersaturated Cu-Co Alloy

Rico Bauer, Bastian Rheingans and Eric J. Mittemeijer

Abstract

The kinetics of the precipitation of Co from a supersaturated solid solution of Cu-0.95 at.% Co was investigated by isochronal annealing applying differential scanning calorimetry (DSC) with heating rates in the range 5 Kmin^{-1} to 20 Kmin^{-1} . The corresponding microstructural evolution was investigated by (high-resolution) transmission electron microscopy [(HR)TEM] in combination with electron energy loss spectroscopy (EELS). Upon isochronal annealing spherical Co precipitates of fcc crystal structure form. Kinetic analysis by fitting of a modular phase transformation model to, simultaneously, all DSC curves of variable heating rate measured for Cu-0.95 at.% Co showed that the precipitation-process mechanism can be described within the framework of this general phase transformation model by continuous nucleation and diffusion-controlled growth. By introducing additional microstructural information (here the precipitate-particle density), for the first time values for the *separate* activation energies of nucleation and growth could be deduced from the transformation kinetics.

2.1 Introduction

Knowledge on the nucleation and growth processes involved in a solid-solid phase transformation resulting in a microstructure with specific properties, e.g. mechanical, electric or magnetic properties, is of great interest both from a fundamental scientific point of view and with regard to practical applications. In order to follow the progress of the transformation reaction, a global, macroscopic parameter as the degree of transformation f ($0 \leq f \leq 1$) can be determined experimentally as function of time and temperature. However, it is no easy task to extract from such experimental data quantitative information on the operating modes of nucleation, growth and impingement. To this end a modular phase transformation model [45] has been developed recently that allows separate determination of kinetic data for nucleation, growth and impingement. This model has until now been successfully applied to a variety of phase transformations: crystallisation of amorphous metal alloys [21,46–50], the austenite-ferrite transformation in Fe-based alloys [51–53] and the polytypic transformations of Laves phases [54].

To explore the applicability of this general description of transformation kinetics to the precipitation of a second, product phase in a supersaturated parent, matrix phase, the precipitation of Co from an initially supersaturated dilute solid solution of Cu-0.95 at.% Co was investigated as a model system.

At lower temperatures, Cu and Co show only very small mutual solubility [55]. Upon annealing of supersaturated Cu-rich Cu-Co alloys Co-rich precipitates of fcc structure form within the fcc Cu matrix. During the early stages of the precipitation reaction, these particles show full coherency with the Cu matrix and are of spheroidal shape [56]. Pure Co exhibits an allotropic reaction at the equilibrium temperature $T_a = (690 \pm 7)$ K (at 1 atm) [57] with the hcp modification as low temperature phase and the fcc modification as high temperature phase. Yet, the coherent Co precipitates developing upon precipitation in Cu-rich Cu-Co alloys are generally of fcc structure both above and below T_a .

With conventional transmission electron microscopy (TEM), the small Co-rich precipitates are only indirectly visible due to the strain contrast resulting from the lattice misfit, δ , between the lattices of fcc Co and fcc Cu [56,30] ($\delta = (a_{\text{Co}} - a_{\text{Cu}})/a_{\text{Cu}} \times 100\% \approx -1.9\%$; with the lattice-parameter of Co, $a_{\text{Co}} = 0.35447$ nm, and of Cu, $a_{\text{Cu}} = 0.36146$ nm, [58]). In bright field zone axis (BFZA) TEM mode, the local distortion of the matrix around a Co particle leads to a well-defined circular strain contrast ring, which centre-line corresponds within ± 0.2 nm with the real particle diameter [59,38].

The kinetics of Co precipitation from dilute Cu-Co alloys has been the subject of a large number of investigations over the last decades aimed at

testing the validity of diverse kinetic descriptions, as those based on classical or non-classical nucleation theories (e.g. [32]), sometimes in combination with presumed diffusion-controlled growth (e.g. [60]), based on cluster-dynamics models [61] and on Monte-Carlo simulations (e.g. [62]). Most of these studies showed fair to good agreement or compatibility of the adopted theoretical approach with presented experimental data. However, all experiments were restricted to isothermal annealing and cases of medium or low supersaturation in order to assure modest reaction rates, which are experimentally accessible by microscopic and/or scattering techniques.

In the present project non-isothermal, but isochronal (i.e. with constant heating rate) annealing experiments, applying differential scanning calorimetry (DSC), have been performed, i.e. the experiments start at a low temperature, where the degree of supersaturation is very high, but the rate of the thermally activated reaction is virtually nil. Upon heating thermal activation eventually becomes substantial enough to induce precipitation from the highly supersaturated solid solution. Thus isochronal heating DSC experiments allow experimental access to data for the formation and growth of Co precipitate particles in the presence of very large driving forces. Large, as compared to small, driving forces can substantially affect the modes of nucleation and growth. Against this background the present work is focused on kinetic analysis, applying a modular phase-transformation model [11], to the precipitation of Co from a highly supersaturated Cu-0.95 at.% Co solid solution in order to identify the separate nucleation and growth mechanisms and to determine the associated kinetic parameters. It will be shown that the kinetic analysis can be powerfully performed on the basis of isochronal (DSC) annealing experiments, provided the kinetic model is fitted to simultaneously all transformation curves measured at various heating rates. In combination with microstructural information (the product-particle density obtained by TEM investigation), separate values for the activation energies of nucleation and growth could be determined.

2.2 Theoretical background of transformation kinetics

The modular phase transformation model comprises three modes – nucleation, growth and impingement – which can be dealt with separately [63, 11]. In the following those aspects of nucleation, growth and impingement which are relevant for the present work are indicated briefly.

According to classical nucleation theory, the steady state rate of nucleation

of product phase particles per unit volume can be given as

$$\dot{N}(T(t)) = C\omega \exp\left(-\frac{\Delta G^* + Q_N}{RT(t)}\right), \quad (2.1a)$$

with the gas constant R , the temperature T depending on time t , the number density of suitable nucleation sites C , a characteristic frequency factor ω , the critical Gibbs energy ΔG^* for the formation of a product-phase particle of critical size and the activation energy Q_N for the jump of an atom through the interface of a particle of critical size.

In case of large undercooling, i.e. high supersaturation of the parent phase, $\Delta G^* \ll Q_N$ and the nucleation can be described by the so-called continuous nucleation rate with an Arrhenius temperature dependency

$$\dot{N}(T(t)) = N_0 \exp\left(-\frac{Q_N}{RT(t)}\right), \quad (2.1b)$$

with a temperature- and time-independent pre-exponential factor N_0 .

The two possible extreme growth mechanisms, diffusion-controlled and interface-controlled growth, can be given in a compact expression as follows:

$$Y = g \left[\int_{\tau}^t v dt' \right]^{d/m}, \quad (2.2)$$

with Y as the volume of a particle at time t nucleated at time τ , g as the geometry factor describing the particle shape, d as the growth dimension, m as the growth mode ($m = 1$: “linear growth” at constant temperature, compatible with interface-controlled growth; $m = 2$: “parabolic growth” at constant temperature, diffusion-controlled growth), and v as the growth rate. For large undercooling or overheating, an Arrhenius dependency holds for v [11]:

$$v(T(t)) = v_0 \exp\left(-\frac{Q_G}{RT(t)}\right), \quad (2.3)$$

with Q_G as the temperature- and time-independent activation energy for growth. For interface-controlled growth, v_0 is a temperature-independent interface-velocity constant and Q_G represents the energy barrier at the product/parent interface. For diffusion-controlled growth Q_G represents the activation energy for diffusion, Q_D . In this case, v_0 is a factor depending on the pre-exponential factor for diffusion, D_0 , and on the degree of supersaturation of the matrix phase [3].

Supposing that every product particle grows into an infinitely large parent phase, the precipitate volume of all product particles at time t is given by the so-called extended precipitate volume:

$$V_{p,e} = \int_0^t V \dot{N}(\tau) Y(t, \tau) d\tau, \quad (2.4)$$

where $V_{p,e}$ is the extended precipitate volume and V is the specimen volume. Note that Equations (2.1b) and (2.2) indeed pertain to nucleation and growth, respectively, in the absence of other precipitate particles.

For precipitation reactions the degree of transformation can be defined as the volume V_p occupied by precipitate particles normalised with respect to the volume $V_{p,end}$ of the precipitate particles at the end of the reaction:

$$f \equiv \frac{V_p}{V_{p,end}}, \quad (2.5)$$

with $0 \leq f \leq 1$. Thus the extended precipitate-volume fraction, $x_{p,e}$, can be given as (cf. Equation (2.4))

$$x_{p,e} = \frac{V_{p,e}}{V_{p,end}} = \frac{V}{V_{p,end}} \int_0^t \dot{N}(\tau) Y(t, \tau) d\tau. \quad (2.6)$$

Evidently, product-phase particles cannot nucleate and grow in specimen volume that has already been occupied by other product-phase particles. This is called "hard impingement". Further, if diffusion of solute towards precipitate/product-particles is necessary to establish growth, then a solute-depletion zone can develop around a growing product particle in which zone less likely further nucleation can take place (because of a lesser supersaturation) or even no further nucleation can occur at all (if the supersaturation has become negligible). This is called "soft impingement". Various explicit modes for hard impingement have been given in the literature (see [11]). A rigorous treatment for "soft impingement" does not exist. It can be inferred (see [64]), for the case of randomly dispersed nuclei and isotropic growth, that a correction for impingement in case of growth controlled by solute diffusion in the matrix can be realised by equating the infinitesimal change df with the infinitesimal change of $x_{p,e}$ multiplied with the untransformed fraction $(1 - f)$:

$df = (1 - f) \times dx_{p,e}$. This leads to

$$f \equiv \frac{V_p}{V_{p,\text{end}}} = 1 - \exp(-x_{p,e}) = 1 - \exp\left(-\frac{V_{p,e}}{V_{p,\text{end}}}\right). \quad (2.7)$$

This result implies a formalism of "soft impingement" that parallels that for "hard impingement" (also in case of random nucleation and isotropic growth). This may be understood as that for the case of "soft impingement" each precipitate/product particle is supposed to be surrounded, effectively, by an outer solute depleted shell of size such that upon completed precipitation all precipitate particles with their surrounding solute depleted shells occupy the whole volume of the specimen.

For a wide range of nucleation and growth modes the following analytical expression for $x_{p,e}$ for isochronal heating can be given [11]:

$$x_{p,e} = \frac{V}{V_{p,\text{end}}} \left(\frac{RT^2}{\Phi}\right)^n \left(\frac{K_0}{Q}\right)^n \exp\left(-\frac{nQ}{RT}\right) \quad (2.8)$$

with the time and temperature independent rate K_0 , the overall activation energy Q , the growth exponent $n = d/m + 1$ and $(V/V_{p,\text{end}})^{-1}$ as the volume fraction of particles at the end of the reaction.¹ For extreme cases of nucleation, as site saturation and continuous nucleation (see Equation (2.1b)), in combination with interface-controlled and diffusion-controlled growth, the growth exponent n adopts values as listed in Table 2.1. The overall activation energy Q can be expressed as a weighted sum of Q_N and Q_G using n and the ratio d/m as weighting factors [65]:

$$Q = \frac{\frac{d}{m}Q_G + \left(n - \frac{d}{m}\right)Q_N}{n} \quad (2.9)$$

Fitting the kinetic model by applying Equation (2.8) in combination with an appropriate impingement correction, e.g. as given by Equation (2.7), to phase-transformation data obtained from experiment allows for determination of the kinetic parameters K_0 , Q and n , which can suffice for an identification of the probably governing nucleation and growth modes (see Table 2.1). In

¹Note that Equation (2.8) differs in two aspects from Equation (31) in [11]: (i) because of the different normalisation of f (and $x_{p,e}$), i.e. with respect to $V_{p,\text{end}}$ (not V) in the current paper, the fraction $V/V_{p,\text{end}}$ appears in Equation (2.8); (ii) the factor K_0 in Equation (31) in [11] is equal to K_0/Q in the present Equation (2.8), because in [11] the factor $1/Q$ has been incorporated in the expressions for K_0 given for isochronal annealing in Tables 1 to 3 in [11].

Table 2.1: Values for the growth exponent n in case of site saturation or continuous nucleation in combination with 3-dimensional ($d = 3$) interface-controlled ($m = 1$) or diffusion-controlled growth ($m = 2$).

	interface-controlled	diffusion-controlled
	growth	growth
site saturation ($n = d/m$)	3	3/2
continuous nucleation ($n = d/m + 1$)	4	5/2

the following this type of kinetic analysis will be referred to as the "general" case.

The kinetic parameters K_0 , Q and n can be substituted by analytical expressions, valid upon isothermal or isochronal annealing, as listed in Tables 1 to 3 in [11] for a range of specific nucleation and growth modes, which describe the transformation kinetics in terms of parameters as N_0 , v_0 , Q_N and Q_G . However, v_0 and N_0 cannot be determined separately in a subsequent fitting procedure to transformation-rate data, as they always appear in combined fashion, e.g. $(N_0 \times v_0^{d/m})$ (see Equation (2.12a) below), in the expression for $(K_0/Q)^n$. Further, if Q_N and Q_G only appear in Q (see Equation (2.9)), the fitting also cannot lead to determination of separate values for Q_N and Q_G . Upon isochronal annealing a further combination of Q_N and Q_G (in a way different from Equation (2.9)) appears in the expression for $(K_0/Q)^n$ (see C_c in Equation (2.12b) below). Then fitting to the transformation-rate data (here the DSC scans) could in principle lead to separate values of $(N_0 v_0^{d/m})$, Q_N and Q_G . However, the value of C_c (and thus the value of $(K_0/Q)^n$) is rather insensitive to changes of Q_N and Q_G . Therefore, extra experimental information depending in different ways on $(N_0 v_0^{d/m})$, Q_N and Q_G has to be incorporated in the model fitting. As demonstrated in this paper such experimental data is provided by e.g. the number density of product particles at the end of the transformation reaction.

2.3 Experimental

A cylindrical ingot with a diameter of 8 mm was produced by melting Cu (99.9995 at.%) and Co (99.995 at.%) under a protective argon atmosphere. The overall composition was determined to Cu-(0.95 \pm 0.01) at.% Co applying

inductively coupled plasma-optical emission spectrometry (ICP-OES) for the metal components. The degree of oxygen contamination of the alloy was determined by carrier gas hot extraction yielding a negligible value of less than 10 $\mu\text{g/g}$. The ingot was homogenised at 1333 K for 138 h within a silica capsule filled with a protective argon atmosphere, followed by a quench by breaking the capsules in ice water. Thereafter the ingot was hammered down to a diameter of 5 mm and subsequently cut into discs of about 500 μm thickness. The specimen discs were recrystallised at 1333 K for 48 h and quenched thereafter as described above. Next, the discs were ground and polished using 0.25 μm diamond paste as last step.

Isochronal annealing experiments (leading to Co precipitation) were performed with a differential scanning calorimeter (DSC) Pyris 1 from Perkin Elmer. The DSC was calibrated using the temperature and enthalpy of melting of In, Zn and Al. Sample and (empty) reference pan were made of Y_2O_3 . For each measurement a new specimen disc was used.

Starting from room temperature, isochronal annealing was performed at heating rates in the range from 5 Kmin^{-1} to 20 Kmin^{-1} . Two consecutive heating runs were performed in order to determine the baseline from the second run. In the second run no further reaction was observed.

The microstructure of the specimens prior to and after the DSC runs was investigated by transmission electron microscopy (TEM).

Electron transparent foils for TEM were prepared in three steps: first, the diameter of the discs was reduced from 5 mm to 3 mm by grinding. After this, in a second step, the disc thickness was reduced by grinding from initially 500 μm to about 120 μm . In a third step the discs were electrolytically etched with a D2 electrolyte by Struers using a Tenupol 5 device. TEM was performed using a Zeiss 912 Omega instrument at an accelerating voltage of 120 kV, which is equipped with an energy filter for electron energy loss spectroscopy (EELS). Bright field images in zone axis orientation were recorded with a Gatan digital camera. The particle density and the precipitate-volume fraction after isochronal annealing were calculated by counting the number and measuring the size of all particles visible in the bright field image. The thickness of the foil at the location where the measurements were made was determined by EELS applying the log-ratio method [66] with a value for the scattering mean-free path of 100 nm calculated for the given alloy composition and the experimental conditions applied in TEM. The accuracy of the thickness measurement with EELS is about $\pm 20\%$.

Supplementary isothermal annealing experiments were performed for a Cu-(2.13 \pm 0.03) at.% Co alloy at 843 K. For this alloy, additional high resolution TEM (HRTEM) investigations were made using a Jeol FX 4000 at an acceleration voltage of 400 kV.

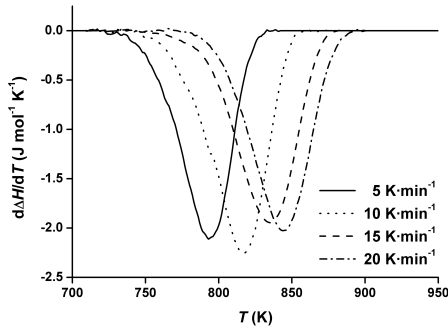


Figure 2.1: Isochronal baseline corrected DSC-scans of the precipitation of Co at various heating rates for Cu-0.95 at.% Co.

2.4 Results and evaluation

2.4.1 Differential scanning calorimetry

The baseline-corrected isochronal DSC curves describing the precipitation of Co from supersaturated Cu-0.95 at.% Co (for microstructural evidence, see Section 2.4.2) measured at heating rates in the range from 5 Kmin⁻¹ to 20 Kmin⁻¹ are shown in Figure 2.1.

The peak maximum of the resulting differential enthalpy signal $d\Delta H/dt$ shifts towards higher temperature with increasing heating rate. The measured total transformation enthalpy ΔH_{tot} of the precipitation reaction was found to be independent of the heating rate and temperature range: $\Delta H_{\text{tot}} = (-95 \pm 7) \text{ Jmol}^{-1}$.

The degree of transformation, f , was determined as follows

$$f(t) = \left(\frac{V_p(t)}{V_{p,\text{end}}} \right) \frac{\Delta H(t)}{\Delta H_{\text{tot}}} \quad (2.10)$$

with ΔH as the cumulative transformation enthalpy obtained by integration of the heat signal $d\Delta H/dt$ ($\Delta H < 0$ in case of an exothermic precipitation reaction which is the case here). In case of a precipitation reaction, the definition for f expressed by Equation (2.10) is appropriate if a fixed reference state for the reaction can be assumed, i.e. if $V_{p,\text{end}}$, or ΔH_{tot} , is independent of heating rate and temperature.² Since ΔH_{tot} was indeed found to be independent of

²This is equivalent to the assumption that the change of the mutual solubilities of Co and Cu is negligible in the temperature range of interest, which is also a prerequisite for adopting Arrhenius temperature dependencies for nucleation and growth (c.f. [67]).

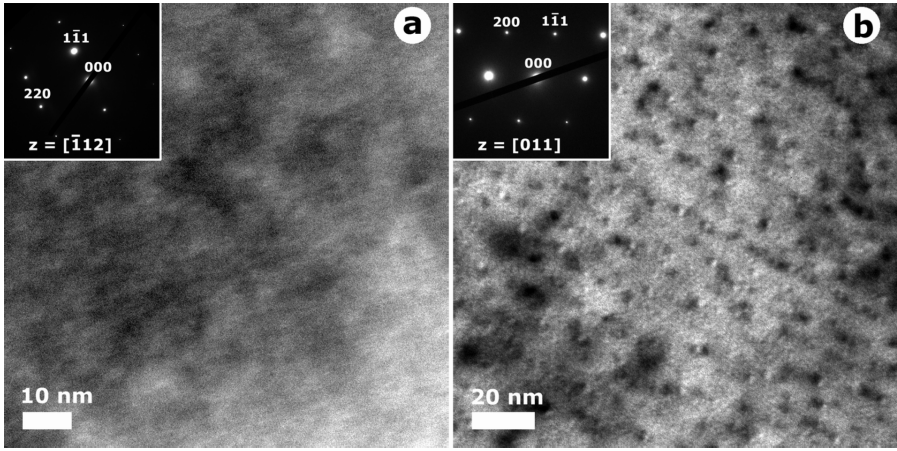


Figure 2.2: TEM bright field images and the corresponding SADPs (a) prior to and (b) after isochronal annealing with 20 Kmin^{-1} up to about 900 K, i.e. immediately after the DSC peak (see Figure 2.1), of Cu-0.95 at.% Co. (a) No precipitates are visible in the as-quenched state ($[-112]_{\text{Cu}}$ zone axis). (b) Small coherent spherical fcc Co particles are observed in the annealed state with a particle density of $N_V = 7.19 \times 10^{23} \text{ m}^{-3}$ and a mean particle diameter of $d_m = 1.6 \text{ nm}$ leading to a volume fraction of precipitate equal to 0.147 vol.% ($[011]_{\text{Cu}}$ zone axis).

the heating rate (see above), this condition is satisfied.

2.4.2 TEM and HRTEM

TEM bright-field images and the corresponding selected area diffraction patterns (SADPs) taken prior to and after isochronal annealing with 20 Kmin^{-1} up to about 900 K, i.e. immediately after the DSC peak (see Figure 2.1), of Cu-0.95 at.% Co are shown in Figure 2.2 (a) and Figure 2.2 (b).

After quenching from about 1333 K to room temperature no precipitation was observed in Cu-0.95 at.% Co (see Figure 2.2 a). Then, upon isochronal annealing spherical coherent fcc Co particles developed in the matrix (see Figure 2.2 (b) and Figure 2.3). The particle density was determined as $N_V = 7.19 \times 10^{23} \text{ m}^{-3}$ and the mean particle diameter as $d_m = 1.6 \text{ nm}$ with a particle-diameter range from about 1 nm to 3 nm. This corresponds to a volume fraction of precipitate particles equal to 0.147 vol.% (see Section 2.3).

An HRTEM image of a Co nanoparticle, formed in the Cu-2 at.% Co alloy after isothermal annealing at 843 K for 60 min, is shown in Figure 2.3. Evidently the nanoparticle has full coherency with the surrounding Cu-rich matrix

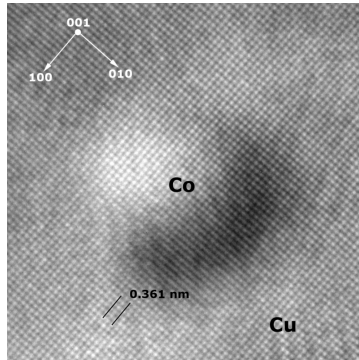


Figure 2.3: HRTEM image of Cu-2 at.% Co annealed at 843 K for 60 min ([001] zone axis). The image shows a spherical Co-rich particle fully coherent with the surrounding Cu-rich matrix. The precipitate particle has a fcc crystal structure, as well as the matrix.

and exhibits a fcc crystal lattice.

2.4.3 Analysis of transformation kinetics

Values for Q and n can be determined without recourse to any specific model using procedures given in [11, 63]: For isochronal anneals of variable heating rate the effective activation energy Q can be deduced from the temperatures where a specific, chosen degree of transformation is attained, according to a Kissinger-like analysis [63] (Figure 2.4), and a value for the growth exponent n can be deduced from the degree of transformation where a specific, chosen temperature is attained, according to a procedure presented in [11] (Figure 2.5). The values for the effective activation energy, Q , and the growth exponent, n , as determined by these separate methods have been summarised in Table 2.2.

The impingement mode can be deduced from a plot of the transformation rate df/dT versus the corresponding transformed fraction f [68]. Such a plot is shown for the present data in Figure 2.6. All curves show a peak maximum at a value of about 0.6 for the transformed fraction. This value agrees very well with the theoretical value $f = 1 - 1/e$ for the case of an impingement correction as given by Equation (2.7) (see also [68]) and thereby validates this choice of impingement mode.

The kinetic parameters K_0 , Q and n were determined by fitting the "general" model (combination of Equations (2.7) and (2.8)) to *simultaneously* all iso-

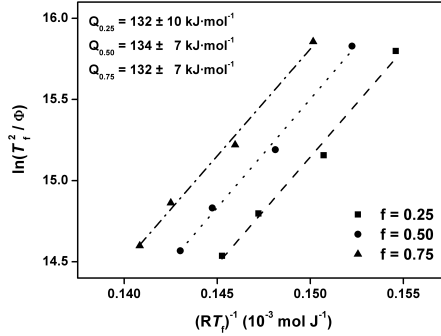


Figure 2.4: Determination of the effective activation energy according to Kissinger-like analysis for isochronal annealing [63]: plot of $\ln(T_f^2 / \Phi)$ vs. $(RT_f)^{-1}$ with Φ as the heating rate and T_f as the temperature at which the degree of transformation attains a specific, chosen value. Results for $f = 0.25, 0.50$ and 0.75 are shown. The slope of the straight line fitted to the data points for constant f yields a value for the effective activation energy, Q . The corresponding values of Q have been indicated in the figure.

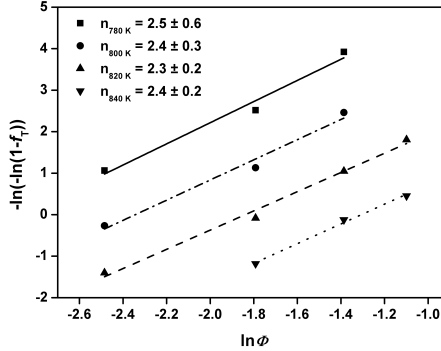


Figure 2.5: Determination of the growth exponent according to a procedure for isochronal annealing given in [11]: plot of $-\ln(-\ln(1-f_T))$ vs. $\ln \Phi$ with Φ as the heating rate and f_T as the transformed fraction at which the temperature attains a specific, chosen value. Results for $T = 780 \text{ K}, 800 \text{ K}, 820 \text{ K}$ and 840 K are shown. The slope of the straight line fitted to the data points for constant temperature yields a value for the growth exponent n . The corresponding values of n have been indicated in the figure.

Table 2.2: Values obtained for the kinetic parameters K_0 , Q and n as determined by fitting the modular phase-transformation model for the "general" case as well as for fixed values of the growth exponent n (i.e. fixed modes for nucleation and growth, see Table 2.1) to the experimental data (MSE is the mean square error of the fit) and values for the overall activation energy Q and the growth exponent n as determined by model independent analysis (Figures 2.4 and 2.5). (CN: continuous nucleation, SS: site saturation, DCG: diffusion-controlled growth, ICG: interface-controlled growth)

model	$\frac{K_0}{s^{-1}}$	$\frac{Q}{\text{kJmol}^{-1}}$	n	$MSE/\%$
"general"	7.6×10^4	134	2.2	2
CN + DCG	2.9×10^4	126	5/2 (fixed)	4
SS + DCG	809.0×10^4	174	3/2 (fixed)	18
CN + ICG	0.2×10^4	101	4 (fixed)	68
SS + ICG	0.8×10^4	115	3 (fixed)	17
procedure for Q ; Kissinger-like analysis [63]	-	133 ± 8	-	-
procedure for n [11]	-	-	2.4 ± 0.3	-

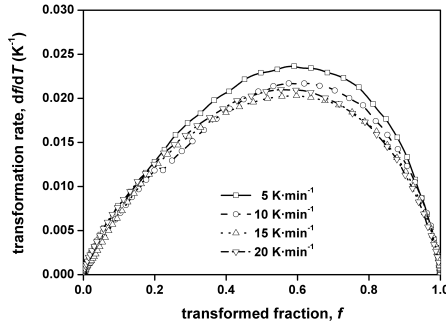


Figure 2.6: The transformation rate as function of the transformed fraction f (obtained from the data shown in Figure 2.1). The peak maximum occurs at a value for f equal to about $1 - 1/e \approx 0.6$ which is compatible with Equation (2.7).

chronal heating runs of variable heating rate as recorded from the as-quenched supersaturated Cu-0.95 at.% Co. Start values for the fit parameters K_0 , Q and n were estimated within a physical meaningful range. Then a calculated transformed fraction vs. temperature curve was obtained according to Equations (2.7) and (2.8). The mean square error (MSE) was defined as the squared difference between the calculated (f_{calc}) and experimental (f_{exp}) transformed fraction curves normalised with respect to f_{exp} for each, i -th, of the heating rates applied:

$$MSE = \sum_{i=1}^{n_{\Phi}} \left[\sum_{\text{data points}} \left(\frac{f_{\text{exp}} - f_{\text{calc}}}{f_{\text{exp}}} \right)^2 \right], \quad (2.11)$$

with n_{Φ} as the number of heating rates applied. The MSE was minimised by varying the fit parameters using a multidimensional unconstrained non-linear minimisation fitting routine as implemented in MATLAB. The results of the fitting as described above are shown in Figure 2.7. The corresponding values for the fitting parameters of the "general" model have been gathered in Table 2.2.

Adopting specific nucleation and growth modes, as site saturation (pre-existing nuclei) or continuous nucleation and diffusion-controlled or interface-controlled growth, the growth exponent n was set to a fixed value (see Table 2.1) and solely K_0 and Q were used as fit parameters. Values obtained for the fit parameters for the above cases of specific nucleation and growth modes have also been listed in Table 2.2.

Evidently the values for Q and n , as obtained from (i) the general case of

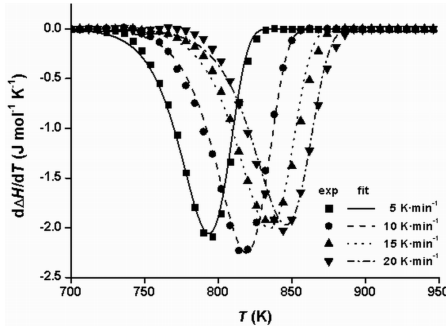


Figure 2.7: Isochronal DSC curves and model fit (simultaneously to all runs) using the modular phase transformation model (K_0 , Q and n as fit parameters) for the precipitation of Co from supersaturated Cu-0.95 at.% Co (experimental data: symbols; fit: lines).

the modular phase transformation model, (ii) the modular phase transformation model based on a combination of continuous nucleation and diffusion-controlled growth and (iii) the model-independent, separate methods, agree well. It is also noted that the smallest values for the mean square error of the model fits occur for the cases described under (i) and (ii). Continuous nucleation and diffusion-controlled growth can thus be adopted as nucleation and growth mechanisms controlling the Co precipitation reaction.

For the above identified nucleation and growth modes analytical expressions for Q and K_0 are available: the overall activation energy Q is given by Equation (2.9) and the rate constant K_0 can be expressed as follows [11]:

$$\left(\frac{K_0}{Q}\right)^n = \frac{gN_0v_0^{d/m}C_c}{n}, \quad (2.12a)$$

with C_c as a correction factor depending on the activation energy values for nucleation, Q_N , and growth, Q_G [69]:

$$C_c = \frac{5}{2} \frac{Q_G^{1/2} (3Q_G + 4Q_N)}{4Q_N (Q_N + 1/2 Q_G) (Q_N + Q_G) (Q_N + 3/2 Q_G)} \quad (2.12b)$$

The shape factor g for spherical product particles (see Figure 2.3 and Section 2.4.2) is given by $g = 4\pi/3$. As discussed in Section 2.2, fitting of the modular phase-transformation model expressed in terms of fitting parameters as N_0 , v_0 , Q_N and Q_G to data of the degree of transformation as function of

time and/or temperature, in order to find values for these fitting parameters, is partly impossible (in this case for N_0 and v_0 , separately) or partly impracticable (in this case for Q_N and Q_G). Involvement of extra experimental information depending on the kinetic parameters in a way different from the transformation-rate data is required. One possible approach is to measure the number of precipitated particles per unit volume, i.e. the product-particle density $N_{\text{exp}}^{\text{tot}}$, after completed transformation, i.e. after completion of the peak in the DSC scans (see Section 2.4.2 and Figure 2.2). The product-particle density is related to the (continuous) nucleation rate \dot{N} (see Equation (2.1b)) and is calculated by

$$N_{\text{calc}}^{\text{tot}} = \int_0^t \dot{N}(\tau) (1 - f(\tau)) d\tau. \quad (2.13)$$

Applying Equation (2.13) with the requirement $N_{\text{exp}}^{\text{tot}} = N_{\text{calc}}^{\text{tot}}$ as additional constraint in the fitting now leads to determination of separate values for the parameters N_0 , v_0 , Q_N and Q_G by numerical fitting of Equations (2.7) and (2.8) to the experimentally determined degree of transformation, f . For that purpose, the total mean square error (MSE_{tot}) is defined as the sum of (a) the mean square error (MSE) for the fitted transformed fraction curves (see Equation (2.11)) and (b) the squared difference between the calculated ($N_{\text{calc}}^{\text{tot}}$) and experimental ($N_{\text{exp}}^{\text{tot}}$) particle density normalised with respect to $N_{\text{exp}}^{\text{tot}}$ for the isochronal anneal with the largest heating rate (20 Kmin⁻¹) for which the final particle density was determined by TEM measurement (see Section 2.4.2):

$$MSE_{\text{tot}} = \frac{z-1}{z} MSE + \frac{1}{z} \left(\frac{N_{\text{exp}}^{\text{tot}} - N_{\text{calc}}^{\text{tot}}}{N_{\text{exp}}^{\text{tot}}} \right)^2 \Bigg|_{\phi=20 \text{ Kmin}^{-1}}, \quad (2.14)$$

with z as the total number of experimental data points composed of all heating-rate data points plus one for the particle density.

Fitting of the kinetic model to the degree of transformation rate data (the DSC scans) subjected to the constraint $N_{\text{exp}}^{\text{tot}} = N_{\text{calc}}^{\text{tot}}$ (TEM product-particle density) yielded the following values for the fit parameters: $N_0 = 3.9 \times 10^{24} \text{ s}^{-1}$, $v_0 = 4.6 \times 10^{-10} \text{ m}^2 \text{ s}^{-1}$, $Q_N = 50 \text{ kJmol}^{-1}$ and $Q_G = 177 \text{ kJmol}^{-1}$. The fitted transformation curves are shown in Figure 2.8.

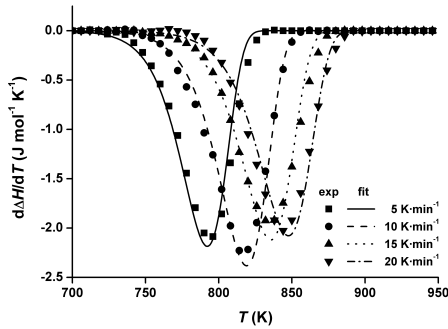


Figure 2.8: Isochronal DSC curves and model fit (simultaneously to all runs) using the modular phase transformation model (continuous nucleation and diffusion-controlled growth with N_0 , v_0 , Q_N and Q_G as fit parameters and the experimentally determined particle density $N_{v,\text{exp}}$ as additional boundary condition) for the precipitation of Co from supersaturated Cu-0.95 at.% Co (experimental data: symbols; fit: lines).

2.5 Discussion

The as-quenched Cu-0.95 at.% Co alloy exhibits a homogeneous precipitate-free microstructure (Figure 2.2 (a)). Upon precipitation spherical, coherent, fcc Co particles develop, as revealed by HRTEM (Figure 2.3). The low-temperature hcp Co phase was not observed, indicating the very small difference in bulk energy of the fcc and hcp modifications [70]. The spherical shape, and possibly the preservation of the fcc structure at room temperature, of the small coherent particles may be ascribed to a delicate interplay of elastic strain energy and interface energy [71].

The TEM analysis in combination with EELS yielded a precipitate-volume fraction of Co of 0.147 vol.% (Section 2.4.2) immediately after completion of the exothermic peak in DSC, whereas for a total separation into phases with equilibrium concentrations as given by the phase diagram [55], a volume fraction of precipitates of about 0.89 vol.% is expected for a Cu-0.95 at.% Co alloy. Before interpretation of this observed discrepancy can occur two possible error sources must be taken into consideration: (a) The determination of the specimen volume with EELS and (b) the measurement of the particle size: (a) The accuracy of the thickness measurement is $\pm 20\%$ [66]. The measurement of lateral distances in the digitalised TEM image can occur with an accuracy of about $\pm 2\%$. This leads to an accuracy of the volume determination of about $\pm 25\%$. (b) The measurement of the particle diameter is based on an estimate of the position of the centre line in the ring of strain contrast. The

inaccuracy of the value thus determined for the particle size is estimated at ± 0.2 nm [38]. This [(a) + (b)] leads to a range for the measured precipitate-volume fraction from 0.078 vol.% to 0.280 vol.%, still clearly remote from the expected equilibrium value.

DSC measurements revealed that the total enthalpy change associated with the precipitation reaction is about (-95 ± 7) Jmol⁻¹ (see Section 2.4.1). The enthalpy of decomposition according to the reaction $(\text{Cu,Co})_{\text{fcc}} \rightarrow (\text{Cu})_{\text{fcc}} + (\text{Co})_{\text{fcc}}$ can be assessed adopting the regular solution model for the solid solution with a, for dilute solid solutions, concentration independent interaction parameter $\Omega = 37048$ Jmol⁻¹ [72]. At a temperature of about 1000 K, the here recorded transformation enthalpy corresponds to a precipitate-volume fraction of about (0.181 ± 0.014) vol.%. This result agrees well with the above discussed range of values for the precipitate-volume fraction as determined by TEM (plus EELS).

Hence, the discrepancy between the expected precipitate-volume fraction of about 0.89 vol.% for total decomposition and the experimentally observed precipitate-volume fraction of about 0.147 vol.% indicates that, at the apparent end of the reaction represented by the exothermic peak in the DSC scans (Figure 2.1), a significant fraction of Co (here 0.8 at.%) still is dissolved.

Understanding of this observation is provided by the additional isothermal annealing experiments, performed in the present project, for the Cu - 2.13 at.% Co alloy at 843 K (c.f. Section 2.3): as demonstrated by particle density measurements with TEM, no further Co particles nucleated after 15 min annealing. The solute concentration in the matrix measured with EDX at this stage still was (1.7 ± 0.3) at.%, being compatible with the Co particle density and size distribution as determined by TEM. Continued annealing showed that the Co particle size increased with a simultaneous decrease of the particle density and a decline of the solute concentration in the matrix down to (0.4 ± 0.2) at.% after 6000 min of annealing. Hence, after an initial rapid nucleation-and-growth stage continued precipitation of Co is realised by a considerably slower process of growth only, accompanied by simultaneous coarsening.

The exothermic DSC peak (Figure 2.1) can therefore be ascribed to an initial stage of Co precipitation by nucleation and growth with a rapid increase of the precipitate-volume fraction and thus with pronounced heat release. Then nucleation effectively comes to a halt. The later stages of growth and coarsening are not well detectable with DSC due to the very small amount of released heat per unit of time.

Because of the abrupt diminution of the reaction rate after the initial stage of the precipitation reaction manifested by the exothermal DSC peak, it appears reasonable to treat this nucleation and growth dominated part of the

overall precipitation reaction as a separate reaction and to define a degree of transformation f with $0 \leq f \leq 1$ by choosing the state of transformation immediately at the end of this first stage as reference state (cf. Equation (2.10)).

The evaluation of the Co precipitation kinetics based on such considerations (Section 2.4.3) revealed that the precipitation of Co, as corresponding to the peaks in the isochronal DSC runs, can be described by continuous nucleation in combination with diffusion-controlled growth. This result is in agreement with the values obtained for Q and n by the methods independent of a specific model (see Figure 2.4 and Figure 2.5) and also with the microstructure: The formation of spherical precipitates (Figure 2.2b and Figure 2.3) suggests 3-dimensional growth ($d = 3$). The growth exponent n as determined by the model independent analysis (Figure 2.5) equals 2.4 ± 0.3 . Within experimental accuracy this value is (only) compatible with diffusion-controlled growth and continuous nucleation satisfying the equation $n = d/m + 1 = 5/2$ [11].

Using additional information, i.e. the particle density immediately after the exothermic peak in DSC, values for the kinetic parameters N_0 , v_0 , Q_N and Q_G could be obtained. For the activation energy of nucleation, a value of $Q_N = 50 \text{ kJmol}^{-1}$ and for the activation energy of growth, a value of $Q_G = 177 \text{ kJmol}^{-1}$ were obtained.

The value of the activation energy for tracer-volume diffusion of Co in Cu [73] is about 214 kJmol^{-1} , thus being significantly larger than the value determined for Q_G . It can be assumed that (a significant amount of) quenched-in vacancies have been retained at the onset of Co precipitation upon isochronal annealing. Preservation of quenched-in vacancies was also found for the isochronal precipitation of Co_2Si from Cu-1 at.% Co_2Si [74] and of CoTi from Cu-1 at.% CoTi [75]. In particular a bonding of quenched-in vacancies to solute Co atoms could occur [76]. In the extreme case this can imply that the vacancy-formation energy is no longer part of the activation energy for Co diffusion. Consequently, the expected value for the activation energy of Co diffusion in the Cu-rich matrix can be considerably reduced as compared to the activation energy for bulk (tracer) diffusion of Co in Cu. This consideration leads to the conclusion that quenched-in vacancies likely contribute to the kinetics of precipitation of the nano-sized fcc Co precipitate particles in the Cu-rich matrix.

The occurrence of a defined initial stage of continuous nucleation and diffusion-controlled growth, with a significant fraction of Co remaining in solution at the end of this initial stage may be interpreted in terms of classical nucleation theory, as follows. For precipitation reactions, the Gibbs energy for formation of a particle of critical size, ΔG^* , strongly depends on the degree of supersaturation [3]. For large degrees of supersaturation, as is the case for the here applied experimental conditions at the beginning of the heat treatment,

ΔG^* is distinctly smaller than the activation energy for nucleation Q_N , and nucleation can be well described by continuous nucleation (Equation (2.2)). With a decreasing degree of supersaturation of the matrix, i.e. with increasing solute depletion by precipitation, ΔG^* increases which can lead to a sharp decline of the nucleation (c.f. Equation (2.1a), note that in the modelling approach applied here the solute depletion of the matrix is accounted for by the impingement correction). The precipitation process then can only be completed by growth, in combination with simultaneous coarsening, which is a comparatively slow process as indicated by the large difference in activation energies obtained in this work for nucleation, Q_N (50 kJmol^{-1}), and growth, Q_G (177 kJmol^{-1}).

2.6 Conclusions

- The precipitation of fcc Co from supersaturated Cu-0.95 at.% Co solid solution is governed by continuous, random nucleation and diffusion-controlled, isotropic growth, as described by the modular phase-transformation model.
- Fitting of the kinetic model to isochronal transformation-rate data, as exhibited by DSC scans, subject to additional constraints as for example provided by microscopic (TEM) product particle-density analysis, allows determination of the kinetic parameters characterizing the separate nucleation and growth modes.
- The effective, overall activation energy of about $(133 \pm 8) \text{ kJmol}^{-1}$ can (thus) be separated into separate activation energies of nucleation and growth of 50 kJmol^{-1} and 177 kJmol^{-1} , respectively.
- Nucleation is found to come to a halt long before all Co dissolved in the Cu-rich matrix has precipitated. Continued precipitation can only be realised by growth, accompanied by simultaneous coarsening, which, as indicated by the activation energies of nucleation and growth, is a relatively slow process.
- The activation energy of growth is distinctly smaller than the activation energy for volume diffusion of Co in equilibrated Cu due to the presence of quenched-in excess vacancies.

Acknowledgement

The authors are grateful to Mr P. Kopold for assistance with HRTEM and to Dr W. Sigle for the STEM analysis both at the Max Planck Institute for Metals Research.

Chapter 3

Crystallisation Kinetics of $\text{Fe}_{40}\text{Ni}_{40}\text{B}_{20}$ Amorphous Alloy

Bastian Rheingans, Yazhu Ma, Feng Liu and Eric J. Mittemeijer

Abstract

The crystallisation of amorphous $\text{Fe}_{40}\text{Ni}_{40}\text{B}_{20}$ alloy upon isothermal annealing was investigated using power-compensating differential scanning calorimetry supported by X-ray diffraction and transmission electron microscopy for microstructure analysis. It was found that the crystallisation occurs in one step mainly by coupled growth of lamellar fcc (Fe,Ni) and orthorhombic $(\text{Fe,Ni})_3\text{B}$ phase. Kinetic analysis of the crystallisation reaction was performed by fitting a modular model of phase transformation simultaneously to several isothermal transformation curves. It was thus found by fitting to transformation-rate data obtained without a pre-annealing treatment that above the glass transition temperature, the crystallisation reaction proceeds by continuous nucleation of new crystalline particles and by growth with a growth law slower than linear growth in 3D, attributed to the lamellar microstructure. By introducing additional experimental data, for variable nucleation mode realised by pre-annealing, separate activation energies for nucleation and for growth could be determined involving fitting to, simultaneously, the set of all transformation rate data comprising both data obtained without pre-annealing and data obtained after pre-annealing.

3.1 Introduction

Since their development more than fifty years ago, metallic glasses have found various fields of application, noticeably in electronics due to their remarkable electric or magnetic properties [28]. The amorphous alloy $Fe_{40}Ni_{40}B_{20}$ is a typical soft magnetic alloy. Its thermal stability and crystallisation behaviour has been the subject of numerous studies in the past. As crystallisation products upon isothermal annealing, orthorhombic (o-) $(Fe,Ni)_3B$ and fcc (Fe,Ni) were identified by X-ray diffraction (XRD) (e.g. [77,78]). In studies using transmission electron microscopy (TEM), the additional occurrence of an fcc $(Fe,Ni)_{23}B_6$ -phase [79,80] or, in one case, a tetragonal $(Fe,Ni)_3B$ -phase [81] was reported. The discrepancy between TEM and XRD results was attributed to the small volume fractions of the last mentioned phases hindering their detection by X-ray diffractometry. As dominating microstructural feature, large rod-shaped crystallites with a lamellar morphology of o- $(Fe,Ni)_3B$ and fcc (Fe,Ni) (“type A”) were observed. Additionally, medium-sized crystallites consisting of fcc (Fe,Ni) and fcc $(Fe,Ni)_{23}B_6$ in lamellar fashion (“type B”) and small nano-scaled crystals consisting of fcc (Fe,Ni) only (“type C”) were found. Demixing of the components in the amorphous state was suggested as possible reason for the simultaneous occurrence of the three different types of crystallites [80].

The kinetic analysis of the crystallisation reaction was performed with several different methods. Kinetic analysis was based on the evolution of the microstructure followed by TEM and light microscopy (LM) [79]: In case of crystallites of type A (LM) and B (TEM), the number density was found to be independent of annealing time and temperature. Thus athermal nucleation due to nuclei formation during quenching from the melt (pre-existing nuclei) was proposed. For the small crystallites of type C (TEM), a temperature-dependent nucleation rate with an activation energy $Q_N = (440 \pm 30) \text{ kJmol}^{-1}$ was determined. Linear growth in three dimensions was observed for all three types of crystallites with a common activation energy of $Q_G = (280 \pm 30) \text{ kJmol}^{-1}$. LM-based kinetic analysis of the evolution of large type A crystallites was performed adopting Johnson-Mehl-Avrami-Kolmogorov (JMAK) kinetics [12–14] presuming pre-existing nuclei [80]. The activation energy of growth and the growth exponent n were there determined to be $Q_G = 237 \text{ kJmol}^{-1}$ and $n = 2.1$, respectively. The deviation from $n = 3$, pertaining to three-dimensional linear growth of pre-existing nuclei [11], was explained as a consequence of anisotropic growth of the rod-shaped crystallites. Differential scanning calorimetry (DSC) was applied to follow the kinetics of crystallisation on the basis of the associated heat effects [82]: Also assuming JMAK kinetics and pre-existing nuclei, Q_G was determined to be

237 kJmol⁻¹. In this case, and in contrast with the above result from Ref. [80], a growth exponent of $n \approx 3$ indeed compatible with linear growth in three dimensions was found. Other studies, also based on adopting JMAK kinetics, yielded growth exponents of about 1.6, interpreted as diffusion-controlled growth, and an activation energy of 364 kJmol⁻¹ ([83], ferromagnetic resonance measurements), or non-constant growth exponents decreasing from 3 to 1 during crystallisation and an activation energy of 250 kJmol⁻¹ ([78], integrated XRD intensity changes). Hence, it can be concluded from the above overview of previous results, that conclusive information on the kinetics of crystallisation is not available: The presence of pre-existing nuclei appears generally accepted, but the nature of the operating growth mechanism is unclear, as reflected by the various different values reported for the growth exponent and the activation energy.

The JMAK approach applied in several of the reported kinetic studies is frequently used to describe the kinetics of isothermal solid state phase transformations proceeding by nucleation and growth of product phase particles. However, the applicability of the classical JMAK equation [12–14] is restricted to special cases of particle nucleation, growth and impingement [1]. To overcome such limitations, several generalisations of the JMAK approach can be made resulting in a modular kinetic model which comprises various possible combinations of different nucleation, growth and impingement modes [11].

In the present work, the isothermal crystallisation of amorphous Fe₄₀Ni₄₀B₂₀ has been revisited with emphasis on the kinetics of crystallisation now using the modular model. The progress of the transformation has been traced by power-compensating differential scanning calorimetry with supplementary X-ray diffraction and transmission electron microscopy investigations. The kinetic parameters of the crystallisation reaction, such as the separate activation energies for nucleation and growth, the growth exponent and the type of impingement, have been determined by application of the modular model of phase transformation kinetics.

3.2 Experiments

Amorphous Fe₄₀Ni₄₀B₂₀ ribbons of about 2 mm in width and 20 μm in thickness were prepared by melt spinning in argon atmosphere from an Fe₄₀Ni₄₀B₂₀ master alloy made of Fe 4N8, Ni 4N8 and B 3N8. The concentration of Fe, Ni and B in the produced ribbons was determined by inductively coupled plasma-optical emission spectroscopy (ICP-OES) to be (46.1 ± 0.5) wt. % Fe, (49.9 ± 0.5) wt. % Ni and (4.52 ± 0.04) wt. % B (ideal wt. composition of Fe₄₀Ni₄₀B₂₀: 46.6 wt. % Fe, 48.9 wt. % Ni and 4.5 wt. % B). The presence of

an initial amorphous state was verified by XRD and TEM (see below).

Differential scanning calorimetry measurements were carried out applying a power-compensating Perkin Elmer DSC 8500 under high-purity argon flow with Al sample pans. In view of the small specimen masses (about 2 mg), an empty aluminium pan was utilised as reference. For temperature calibration, the melting points of In, Pb and Zn, and, for heat flow calibration, the heats of fusion of In and Pb were used.

Isothermal annealing of the ribbons was carried out at $T_a = (672, 675, 678, 681, 684, 687)$ K. In order to reach the isothermal annealing temperature quickly, a heating rate of 500 Kmin^{-1} was applied. For experiments with a pre-annealing treatment prior to the main annealing step (see below for further information), an additional preceding step at $T_{\text{pre}} = 658$ K with a duration of $t_{\text{pre}} = 1200$ s was introduced.

For phase analysis, XRD was performed (Philips X'pert diffractometer with $\text{Co-K}\alpha$ radiation). The microstructure developing upon annealing was investigated with TEM (Zeiss Omega 912 TEM, 120 kV accelerating voltage). Electron-transparent foils were prepared by ion thinning (Fischione Model 1010 Ion Mill).

3.3 Theoretical background

In the classical JMAK approach, the dependency of the transformed fraction f on time t and temperature T is given by

$$f(t, T) = 1 - \exp(-K^n t^n) = 1 - \exp\left(-K_0^n \exp\left(-\frac{nQ_{\text{eff}}}{RT}\right) t^n\right), \quad (3.1)$$

where K is a time-independent factor usually of Arrhenius-type temperature dependency with an effective activation energy Q_{eff} and a constant pre-factor K_0 . R is the ideal gas constant. The constant growth exponent n yields information on the operating mechanisms of nucleation and growth. Equation (3.1) is only strictly valid for randomly distributed nuclei and isotropic growth of particles, i.e. random impingement of particles, and, moreover, the rate of nucleation has to be either constant (continuous nucleation) or zero (pre-existing nuclei, i.e. a constant number of product phase particles from the beginning of the reaction) [1]. In the modular model approach, several generalisations of the JMAK approach are introduced to include various different combinations of different nucleation, growth and impingement modes to increase its possible range of application. In the following, the elements of the modular model relevant for the present study will be indicated.

Two basic descriptions for nucleation are pre-existing nuclei, i.e. nuclei

present at $t = 0$, and continuous nucleation. In case of pre-existing nuclei, the nucleation rate $\dot{N}(t)$ as function of reaction time t can be described by

$$\dot{N}_s(t) = N_{s,0} \times \delta(t - t_0), \quad (3.2)$$

where $N_{s,0}$ is the number of nuclei present at time t_0 and $\delta(t - t_0)$ is the Dirac function. The case of a constant, continuous nucleation rate is expressed as

$$\dot{N}_c(t, T) = N_{c,0} \exp\left(-\frac{Q_N}{RT}\right), \quad (3.3)$$

where $N_{c,0}$ is a pre-exponential factor and Q_N denotes the (constant) activation energy for nucleation. By combining both modes of nucleation, the occurrence of a mixed form of nucleation can be described, as well. The growth of product phase particles can be expressed in a compact form: the volume Y of a particle nucleated at time τ at a given time t is

$$Y(\tau, t) = g \left[\int_{\tau}^t v dt' \right]^{d/m}, \quad (3.4)$$

with the particle shape factor g , the growth rate v and the dimensionality d of growth ($d = 1, 2, 3$). The temperature dependency of the growth rate in case of high driving forces is given as

$$v(T) = v_0 \exp\left(-\frac{Q_G}{RT}\right), \quad (3.5)$$

where v_0 is a constant and Q_G the constant activation energy for growth. The value m indicates the growth mode with $m = 1$ in case of a linear growth law and $m = 2$ for a parabolic growth law.

The volume fraction of particles nucleating and growing without inference of other particles, the extended volume fraction $x_e(t)$, can now be calculated by

$$x_e(t) = \int_0^t \dot{N}(\tau) Y(t, \tau) d\tau. \quad (3.6)$$

For isothermal transformations and various (combinations of) different modes of nucleation, the expended volume fraction can be expressed as [11]

$$x_e(t) = K_0(t) n^{(t)} t^{n(t)} \exp\left(-\frac{n(t) \times Q_{\text{eff}}(t)}{RT}\right), \quad (3.7)$$

with a time-dependent growth exponent $n(t)$, rate coefficient $K_0(t)^{n(t)}$ and effective activation energy $Q_{\text{eff}}(t)$. It can be shown that the relation

$$n(t) = \frac{d \ln x_e}{d \ln t} \quad (3.8)$$

between the extended volume fraction and the growth exponent is generally valid [11]. Constant kinetic parameters as in the classical JMAK approach (cf. Equation (3.1)) are obtained if only one type of nucleation mode and one type of growth mode occur in the time-temperature window investigated. In the general case, the effective activation energy can be expressed as a function of the separate, constant activation energies for nucleation and growth and of the time-depending growth exponent:

$$Q_{\text{eff}}(t) = \left(\frac{d}{m} Q_G + \left(n(t) - \frac{d}{m} \right) Q_N \right) / n(t) \quad (3.9)$$

The time dependency of the growth exponent in case of mixed nucleation with contributions of continuous nucleation and site saturation (combining equations (3.2) and (3.3)) is given by

$$n(t) = \frac{d}{m} + \frac{1}{1 + \lambda(t)^{-1}}, \quad (3.10)$$

where $\lambda(t)$ represents the increasing ratio of continuous nucleation to site saturation contribution starting from $\lambda = 0$ at $t = 0$ (see [11]). Thus $n(t)$ increases with time from $n(t = 0) = d/m$ towards the limit of $n(t) = d/m + 1$ for pure continuous nucleation. In this limiting case, Equation (3.9) is underdetermined, i.e. a constant value of Q_{eff} can be realised by different combinations of constant activation energies for nucleation and growth. Hence it is not possible to determine these activation energies separately if only continuous nucleation occurs. One possible approach is to vary the prevailing mode of nucleation artificially, e.g. by applying a pre-annealing treatment to generate pre-existing nuclei. Thus the accessible experimental kinetic data can be sufficiently diversified to separate the contributions of nucleation and growth.

Nucleation and growth of product particles in finite space is obviously limited due to already transformed volume. To obtain the (real) transformed volume fraction f from the extended volume fraction, an impingement correction is introduced depending on the evolution of the microstructure. In the JMAK model, assuming nuclei randomly dispersed in the entire matrix and

isotropic growth, the change of f with x_e is given by

$$\frac{df}{dx_e} = 1 - f. \quad (3.11)$$

Integration and insertion of $x_e(t)$ (Equation (3.6)) yields

$$f = 1 - \exp\left(-K_0(t)^{n(t)} t^{n(t)} \exp\left(-\frac{n(t) \times Q_{\text{eff}}(t)}{RT}\right)\right). \quad (3.12)$$

For K_0 , n and Q_{eff} independent of t , Equation (3.12) reduces to the classical JMAK equation. With reference to Equation (3.11), enhanced impingement can be described by

$$\frac{df}{dx_e} = (1 - f)^\zeta, \quad (3.13)$$

where $\zeta \geq 1$ (relevant for anisotropic growth). A delayed impingement can be expressed by

$$\frac{df}{dx_e} = (1 - f^\varepsilon), \quad (3.14)$$

where $\varepsilon \geq 1$ (relevant for non-random nucleus distribution).

By combination of Equation (3.7) with an appropriate impingement correction, the entire evolution of the transformed volume fraction with time can be modelled. Direct fitting of the modular model to experimental data requires adoption of the governing modes of nucleation and growth, as represented by the growth exponent, and of the mode of impingement correction. Approximates for these characteristics can be inferred from the experimental transformed fraction curve at its point of inversion (maximum transformation rate method, [68, 84]). The results of this single-point analysis can then be used as starting parameters for fitting the model to the entire experimental transformed fraction curves. It is essential that not a single transformation curve is fitted, as often done in the literature where moreover classical JMAK kinetics is usually adopted, but that the modular model is fitted, simultaneously, to a set of isothermal transformation curves (recorded at different temperatures) in order to ascertain uniqueness of the values of the kinetic parameters.

3.4 Results and data evaluation

3.4.1 DSC data evaluation

The amorphous alloy was annealed isothermally within the DSC apparatus at temperatures between 669 K and 684 K. The resulting heat-flux curves

are shown in Figure 3.1. After the initial heating step to reach the desired isothermal annealing temperature, a transient behaviour of the power-compensating DSC as well as a linear baseline drift were observed during the subsequent isothermal step. Therefore, an exponential decay function with a linear term

$$y(t) = a_0 \exp(-a_1 t) + a_2 t + a_3 \quad (3.15)$$

with the parameters $a_i \in \mathbb{R}$, $i = 0, 1, 2, 3$ was used as description of the baseline. This equation was fitted to each curve individually outside the range where the crystallisation proceeds (see Figure 3.1(a)). From the baseline-corrected heat flux curves $\Delta\dot{H} = dH/dt$, the total enthalpy of crystallisation ΔH_{total} can be obtained by integration. For the different annealing temperatures, the same crystallisation enthalpy of $\Delta H_{\text{total}} = (-99 \pm 4) \text{ J/g}$ was obtained. The transformed fraction $f(t)$ as function of annealing time can be calculated by

$$f(t) = \frac{\int_{t_0=0}^t \Delta\dot{H} dt}{\Delta H_{\text{total}}}. \quad (3.16)$$

The transformation rate follows from

$$\dot{f}(t) = \frac{df(t)}{dt} = \frac{\Delta\dot{H}}{\Delta H_{\text{total}}} \quad (3.17)$$

(see Figure 3.4). An analogous analysis was performed for the series with pre-annealing (see Figure 3.1 (b)). Again, the same crystallisation enthalpy was found for the different annealing temperatures with $\Delta H_{\text{total}} = (-104 \pm 4) \text{ J/g}$, i.e. within experimental accuracy not significantly different from the result obtained for the series without pre-annealing. The corresponding transformed fraction curves and the transformation-rate curves are shown in Figure 3.5.

3.4.2 Phase analysis and microstructural evolution

X-ray diffractograms recorded before annealing, after pre-annealing and after completion of the crystallisation at 684 K are shown in Figure 3.2. Both the as-prepared sample and the pre-annealed sample show only the typical, broad peak representing the short-range ordering in the amorphous solid (Figures 3.2 (a), (b)). This implies that crystallisation during pre-annealing is negligible (as also indicated by the practically equal values for the enthalpies of crystallisation as obtained for the series with and without pre-annealing, cf. Section 3.4.1). In the diffractogram of the crystallised sample after the completed isothermal anneal (Figure 3.2 (c)), distinct peaks of diffracting

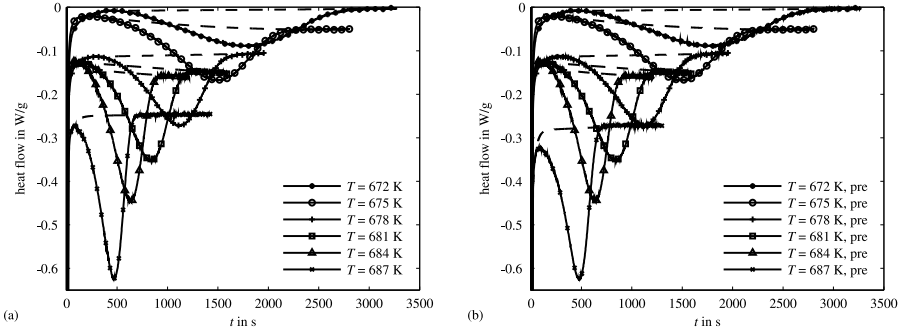


Figure 3.1: Measured heat flow curves for the isothermal crystallisation of $\text{Fe}_{40}\text{Ni}_{40}\text{B}_{20}$ with DSC at various temperatures (a) specimens without pre-annealing, (b) specimens having experienced a pre-annealing step at $T_{\text{pre}} = 658$ K for 1200 s. Solid lines with markers: measured curves; dashed lines: fitted baselines (cf. Equation (3.15)).

crystalline phases are visible. For the fully crystallised samples, a Rietveld refinement with two crystal structures was applied to the diffraction patterns using the TOPAS software [85] (Figures 3.2 (c) and (d)). It followed that the diffraction patterns could be modelled adopting the presence of (i) a solid solution (Fe,Ni) phase of fcc structure ($\text{Fm}\bar{3}\text{m}$, lattice parameter $a = 0.358$ nm, $a_{\text{Fe,fcc}} < a < a_{\text{Ni,fcc}}$) and (ii) a compound $(\text{Fe,Ni})_3\text{B}$ of orthorhombic structure (Pnma , lattice parameters $a = 0.535$ nm, $b = 0.664$ nm, $c = 0.443$ nm). These findings agree well with previous results (see [78] for an overview).

In TEM bright-field (BF) mode, predominantly relatively large grains with an internal microstructure of lamellar morphology were observed (see Figure 3.3 (a) and for larger magnification Figure 3.3 (b)), showing one set of dark lamellae with contrast variations along the lamellae length axes. At very few locations, much smaller crystallites of more homogeneous contrast were found (such an example is deliberately shown in Figure 3.3: see centre of Figures 3.3 (a) & (b)). The selected area diffraction pattern (SADP) at lower magnification (inset in Figure 3.3 (a)) shows concentric circles with numerous diffraction spots due to the nano-scaled nature of the lamellar microstructure. The inhomogeneous distribution of the diffraction spots along the circles suggests that a certain orientation relation between the lamellae exists. The SAD pattern at higher magnification (Figure 3.3 (c)) shows defined patterns of $\text{o}-(\text{Fe,Ni})_3\text{B}$ in $(-1,0,1)$ -zone axis (with additional spots due to double diffraction), and of fcc (Fe,Ni) in $(-1,1,4)$ -zone axis (cf. Figure 3.3 (g)), as well as several extra spots of fcc (Fe,Ni) . By selecting different (groups of) spots

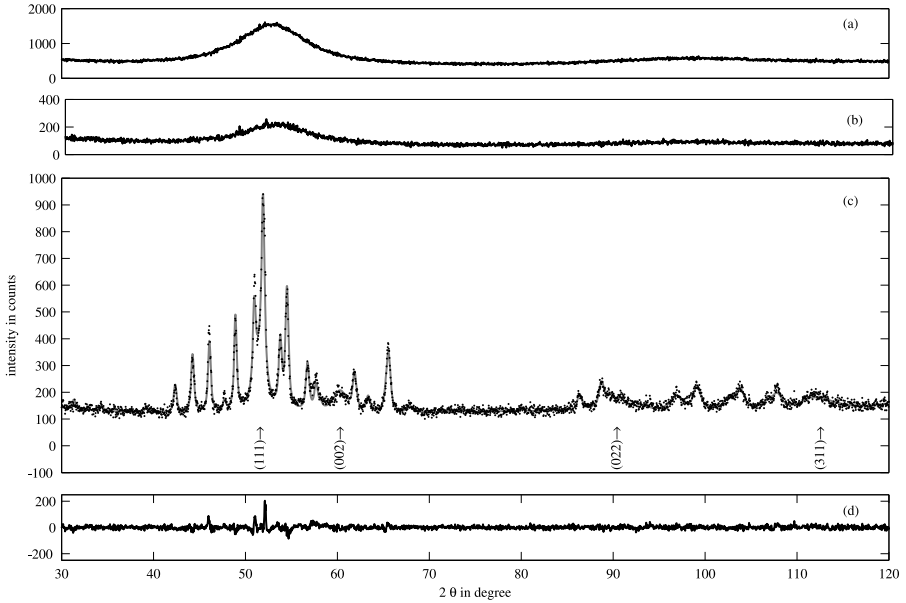


Figure 3.2: X-ray diffractograms of a $Fe_{40}Ni_{40}B_{20}$ ribbon (a) in the as-prepared state and (b) after pre-annealing. Both diffractograms show a broad amorphous peak representing short-range ordering in the amorphous metallic glass. (c) After crystallisation at 684 K, distinct peaks of crystalline phases (black circles) appear which can be modelled adopting two crystalline phases: (i) an orthorhombic compound phase of $(Fe,Ni)_3B$ and (ii) a face-centred cubic solid solution phase (Fe,Ni) . The peak positions of the fcc (Fe,Ni) phase have been identified by arrows. All other peaks can be attributed to the α - $(Fe,Ni)_3B$ phase. Black line: Rietveld refinement. (d) Difference between Rietveld refinement, calculated according to [85], and the measured intensity data.

for dark-field imaging, it could be shown that the set of dark lamellae with the contrast variations in Figure 3.3 (b) consists of fcc (Fe,Ni) (the contrast variations could be caused by stacking faults, which can be generated easily in fcc materials) and that the other set of bright lamellae in Figure 3.3 (b) consists of o-(Fe,Ni)₃B (Figure 3.3 (d)). The orientation relationship between the two sets of lamellae derived from the SAD pattern is close to o-(-1,0,1) || fcc-(-1,1,4), o-[2,5,2] || fcc-[1,-3,1] (Figure 3.3 (g)), which is consistent with the orientation relationship reported in [82] for this system. The small crystallite appears to consist of fcc-(Fe,Ni) only (Figure 3.3 (f)). However, it cannot be excluded that this particle also contains o-(Fe,Ni)₃B phase in very fine distribution.

The above results on phases formed and the associated microstructure lead to the conclusion that the crystallisation reaction is predominated by the simultaneous growth of fcc (Fe,Ni) and o-(Fe,Ni)₃B -lamellae, while a possible separate formation of (Fe,Ni) crystallites contributes only to an insignificant part to the transformed volume and to the heat of crystallisation measured by DSC. Thus a kinetic model for a single reaction can be used to describe the kinetics of the crystallisation process.

3.4.3 Kinetic analysis

3.4.3.1 Isothermal annealing without pre-annealing

In order to determine the governing modes of nucleation, growth and impingement for the present experimental data, a preliminary analysis was performed: using the maximum transformation-rate method (described in Ref. [68]), the impingement mode was found to comply with “non-random nuclei distribution” (cf. Equation (3.14), i.e. delayed impingement), with an impingement parameter $\varepsilon \approx 2.9$ and a growth exponent around 3.8 at the transformation-rate maximum positions for the different annealing temperatures, except for the two lowest temperatures $T_a = (672, 675)$ K. For the latter temperatures, *random impingement* but with similar growth exponents as above was found to prevail. Additional isochronal measurements showed that the glass transition temperature for the alloy lies at approximately 671 K. It is plausible that the governing modes of transformation at temperatures close to the glass transition differ from those well above this temperature. Thus the transformation-rate data of the two lowest temperatures were excluded from further kinetic analysis.

To investigate the influence of the choice of impingement mode, the growth exponent was calculated from Equation (3.8) either using the correct impingement mode as determined above or using the classical “random” (JMAK)

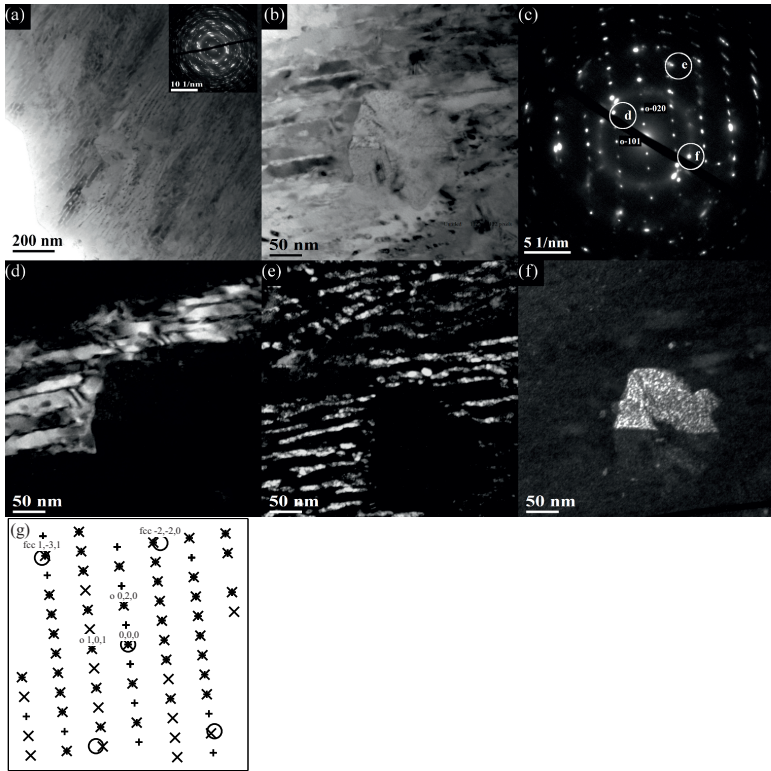


Figure 3.3: (a) Bright-field image of $Fe_{40}Ni_{40}B_{20}$ crystallised at $T = 669$ K showing a lamellar microstructure (inset: corresponding selected area diffraction pattern). In the centre, a separate particle is visible. (b) Bright-field image at the same place as in (a) but at higher magnification showing the lamellar microstructure and the isolated particle. (c) Corresponding SADP. The extended rectangular pattern belongs to the orthorhombic $(Fe,Ni)_3B$ -phase in $(-1,0,1)$ -zone axis with additional spots due to double-diffraction (see (g)). The spots at “e” and “f” correspond to fcc- (Fe,Ni) , the former spots belonging to fcc in $(-1,1,4)$ -zone axis (see (g)). (d) Dark field image using spot “d” in (c) of $o-(Fe,Ni)_3B$ and (e) dark field image using the cluster of spots “e” of the lamellar fcc- (Fe,Ni) phase for imaging. (f) Dark field of the isolated fcc- (Fe,Ni) spot “f” yielding intensity in the upper part of the single particle visible in (b). (g) Schematic representation of the diffraction spots in (c) pertaining to the lamellar orthorhombic $(Fe,Ni)_3B$ -phase in (-101) -zone axis and to the lamellar fcc (Fe,Ni) -phase in $(-1,1,4)$ -zone axis. “x”-markers: genuine diffraction spots of $o-(Fe,Ni)_3B$, “+”-markers: spots caused by double diffraction, “o”-markers: diffraction spots of fcc (Fe,Ni) . The orientation relationship between the two phases is close to $o-(-1,0,1) \parallel fcc-(-1,1,4)$, $o-[2,5,2] \parallel fcc-[1,-3,1]$.

impingement mode. In the former case for ($0.1 < f < 0.9$) almost constant n -values around the transformation-rate maximum values were obtained, whereas in the latter case, the n -values increased from about 3.5 to 5.5 with time, a behaviour which is incompatible with the JMAK model involving “random” impingement.

Next, the modular model, with the correct impingement mode and adopting *constant* kinetic parameters (Equations (3.7) & (3.14)), was fitted to all experimental transformation-rate curves simultaneously with K_0 , Q_{eff} , n and ε as fitting parameters and the values determined above for n and ε as starting values. Albeit the presumption of constant kinetic parameters constrains the adaptability of the modular model, this approach allows easy assessment of the operating kinetics. Fitting was performed using a multidimensional unconstrained nonlinear fitting routine as implemented in MATLAB. The cost function was defined as the sum of the squared differences of the measured and fitted transformation-rate data:

$$error = \sum_{i=1}^k \frac{1}{n} \left(\sum_{j=1}^n \left(\dot{f}_{\text{exp}}(i, j) - \dot{f}_{\text{calc}}(i, j) \right)^2 \right), \quad (3.18)$$

where k is the number of different annealing temperatures and n the number of data points for one annealing temperature. \dot{f}_{exp} and \dot{f}_{calc} are the experimentally determined and the calculated transformation rate, respectively. The results are shown in Figure 3.4 and Table 3.1. For comparison, the same fit was performed using the classical JMAK equation, as well, leading to values of the kinetic parameters also included in Table 3.1. The experimental curves can be described reasonably well with the modular model adopting constant kinetic parameters (see Figure 3.4). Less good results are obtained adopting the JMAK model (cf. Table 3.1). The good agreement between experimental data and the modular model with constant parameters suggests that during the reaction, only one distinct mode of nucleation and one distinct mode of growth prevails (cf. Section 3.3).

From the growth exponent n , potential combinations of nucleation and growth modes can be surmised. In case of pre-existing nuclei as the operating mode of nucleation, n equals d/m , in case of pure continuous nucleation, n equals $d/m + 1$ (cf. Table 3 in Ref. [11]). For isothermal transformations involving these two modes of nucleation, the dimensionality d of growth and the growth mode parameter m solely occur as a ratio d/m in the expressions for n , Q_{eff} and K_0 (cf. Table 1 & 3 in Ref. [11]). Hence, in fitting of isothermal transformation curves, it is not necessary (or possible without further experimental information) to define separate values for d or m . It suffices to adopt

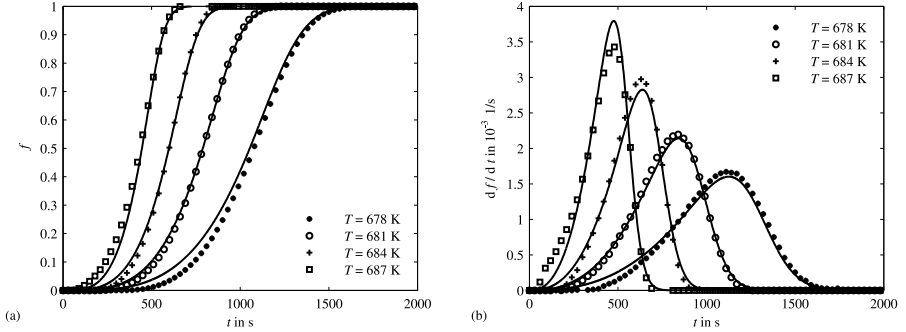


Figure 3.4: Transformed fractions (a) and transformation rates (b) upon isothermal annealing of the specimens without pre-annealing at various temperatures. Markers: experimental data. The full lines represent the results obtained by fitting the general modular model, with *time-independent* fitting parameters Q_{eff} , n , K_0 and ε (Equation (3.7) + Equation (3.14)), to, simultaneously, the set of four transformation-rate curves. The values for the kinetic parameters have been listed in Table 3.1.

Table 3.1: Kinetic parameters for the isothermal crystallisation of $Fe_{40}Ni_{40}B_{20}$ as determined by fitting the modular model with constant parameters, K_0 , n and Q_{eff} , simultaneously to all isothermal transformation rate curves above the glass transition temperature recorded for the samples without pre-annealing using (a) the delayed impingement mode as determined in the preliminary analysis (Equations (3.7) & (3.14)) and (b) the classical JMAK expression (see below Equation (3.12)). The last column represents the error by fitting as defined by Equation (3.18).

	K_0/s^{-1}	$Q_{\text{eff}}/(\text{kJmol}^{-1})$	n	ε	error
delayed impingement	9.7×10^{89}	371	3.5	3.1	1.3×10^{-8}
classical JMAK	2.3×10^{123}	372	4.8	-	2.2×10^{-8}

d/m as a single fit parameter. In order to identify the operating mechanism for nucleation, the modular model, now with explicit expressions for n , Q_{eff} and K_0 for mixed nucleation (as given in Table 1 & 3 of Ref. [11]) and using the general ratio d/m , was fitted to the experimental transformation-rate curves. Fitting clearly converged to pure continuous nucleation. However, as discussed in Section 3.3, in case of pure continuous nucleation it is not possible to separate the effective activation energy into activation energies for nucleation and growth. To this end, additional experimental data are required, e.g. for varying nucleation mode. Thus, in order to change in particular the nucleation kinetics of the transformation, the experiments with an additional pre-annealing step were performed in order to generate pre-existing nuclei in a controlled way (cf. discussion in Section 3.3).

3.4.3.2 Isothermal annealing with pre-annealing; combined fitting

For the specimens subjected to pre-annealing, the maximum transformation-rate method yielded the same impingement mode as for the specimens without pre-annealing, but considerably smaller values for the growth exponent around 2.6 were obtained. Thus it can be concluded that pre-annealing caused the mode of nucleation to shift from the pure continuous nucleation mode in the direction of the pre-existing nuclei nucleation mode.

Since the amorphous state is maintained upon this pre-annealing treatment (see measured enthalpies of crystallisation and XRD results discussed in Sections 3.4.1 & 3.4.2), it is plausible that the pre-annealing treatment has only limited influence on the rate of nucleation of new particles (by continuous nucleation) and on the growth rate. It was therefore tried to fit the modular model *simultaneously* to both data sets, i.e. to the transformation curves with and without pre-annealing, assuming mixed nucleation with varying contributions of pre-existing nuclei and continuous nucleation for both datasets, but assuming a growth mode and an impingement correction mode equal for both datasets. Hence, as fitting parameters common for both datasets, the activation energy for nucleation Q_N , the activation energy for growth Q_G , the ratio d/m and the impingement parameter ε were used; fitting parameters separate for both datasets were the pre-factors for continuous nucleation $N_{c,0}$ and $N_{c,0}^{\text{pre}}$, and the pre-factors for site saturation $N_{s,0}$ and $N_{s,0}^{\text{pre}}$. The resulting values for the kinetic parameters have been summarised in Table 3.2. The corresponding transformed fraction curves are shown in Figure 3.5. The corresponding changes of the growth exponent (Equation (3.10)) and of the effective activation energy (Equation (3.9)) as function of time are shown in Figure 3.6 (a) and (b), respectively. In order to assess the reliability of the fitting results, the starting values for the fit parameters (Q_N , Q_G , d/m , ε ,

Table 3.2: Kinetic parameters for the isothermal crystallisation of $Fe_{40}Ni_{40}B_{20}$ as determined by fitting the modular model with mixed nucleation mode and generalised growth ratio d/m to simultaneously the isothermal transformation rate curves recorded for both the only isothermally annealed specimens and the specimens additionally pre-annealed. For the specimens without pre-annealing, $N_{s,0}$, i.e. the number of pre-existing nuclei at the beginning of the transformation, was found to be too small to be determined accurately.

	$\frac{N_{s,0}}{m^{-3}s^{-1}}$	$\frac{N_{c,0}}{m^{-3}s^{-1}}$				
as-prepared	(1.9×10^{-3})	2.4×10^{65}				
pre-annealed	3.5×10^{22}	8.8×10^{64}				
	$\frac{Q_N}{\text{kJmol}^{-1}}$	$\frac{Q_G}{\text{kJmol}^{-1}}$	$\frac{v_0}{\text{ms}^{-1}}$ (fixed)	d/m	ε	error
shared param.	588	296	1.0×10^{10}	2.4	3.7	1.8×10^{-8}

$\ln(N_{c,0})$, $\ln(N_{s,0})$) were varied individually within ± 50 % around the final values for the fitting parameters as given in Table 3.2. These variations either yielded a larger error or led to the same results or did not converge. The assumption of a systematic error in temperature measurement by ± 2 K led to negligible deviations (within less than 1 %) of the activation energies Q_N and Q_G ; the values of d/m and ε are also not influenced since upon arbitrary temperature changes, the shapes of the curves (and thus the operating modes of nucleation, growth and impingement) remain unchanged.

3.5 Discussion

The crystallisation reaction of amorphous $Fe_{40}Ni_{40}B_{20}$ is associated with a pronounced exothermal heat effect in the form of a single distinct peak in the isothermal DSC scans (Figure 3.1). The XRD and TEM analyses indicated the development of two different crystalline product phases, fcc (Fe,Ni) and o-(Fe,Ni)₃B, predominantly within a lamellar morphology. It is concluded that the crystallisation of fcc (Fe,Ni) and o-(Fe,Ni)₃B predominantly occurs in one step by coupled growth of the lamellar colonies and that the measured heat effect can be ascribed to this dominating crystallisation reaction.

The evaluation of the isothermal transformation-rate curves based on the modular model with constant parameters shows that the kinetics can be described reasonably well with the simplified JMAK-*like* model, if the appropriate impingement correction of delayed impingement is chosen (Equation (3.7) + Equation (3.14); Table 3.1). The thus obtained effective activation energy Q_{eff} of 371 kJmol^{-1} as well as the growth coefficient $n = 3.5$ are considerably

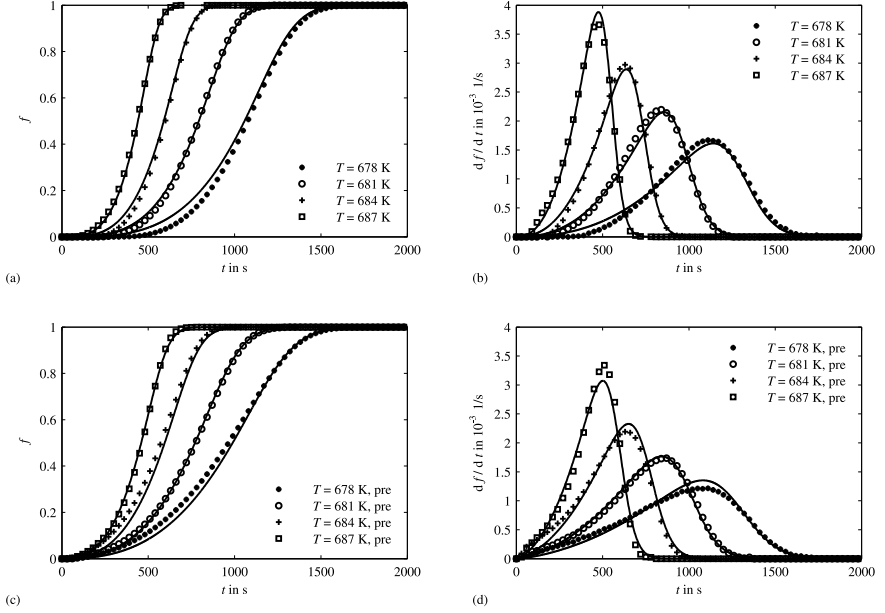


Figure 3.5: Transformed fractions and transformation rates upon isothermal annealing of the specimens without pre-annealing treatment ((a) and (b)) and of the specimens having experienced a pre-annealing step at $T_{\text{pre}} = 658 \text{ K}$ for 1200 s ((c) and (d)). Markers: experimental data. The full lines represent the results obtained by fitting the modular model with explicit expressions for the *time-dependent* fitting parameters $Q_{\text{eff}}(t)$, $n(t)$, $K_0(t)$ (Equation (3.7)) for the case of mixed nucleation and ε (Equation (3.14)) simultaneously to both sets of experimental data, i.e. with and without pre-annealing. The values obtained for the kinetic parameters have been listed in Table 3.2.

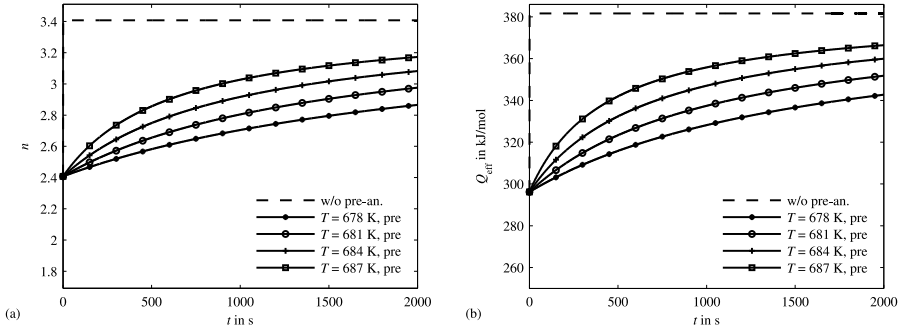


Figure 3.6: Time dependencies of (a) the growth exponent n and (b) the effective activation energy Q_{eff} for crystallisation after pre-annealing (curved solid lines) as compared to crystallisation without pre-annealing (horizontal dashed lines). For the specimens with pre-annealing, both n and Q_{eff} start from the value of pure site saturation (i.e. $n = d/m$ and $Q_{\text{eff}} = Q_G$) and approach asymptotically the limiting value of pure continuous nucleation (see Equations (3.10) and (3.9)).

higher than most of the values given in literature [78, 80, 82, 83]. Assuming the classical JMAK impingement correction (random nucleation + isotropic growth) to be valid, the resulting growth exponent would assume $n = 4.8$, a value which could only be explained by an accelerating nucleation during crystallisation. The effective activation energy Q_{eff} is not influenced since it is independent of the choice of the impingement mode. The occurrence of delayed impingement in this alloy, as could occur by a non-random nucleus distribution, is somehow surprising since for an ideally homogeneous amorphous alloy, random distribution of crystalline product-phase particles may intuitively be expected. Possibly, structural relaxation in the amorphous state above the glass transition temperature could lead to the observed phenomenon, e.g. by promoting a certain degree of ordering of preferential sites for nucleation.

Application of the modular model with explicit expressions for n , Q_{eff} and K_0 revealed that the curves can be modelled best with a continuous nucleation rate (in combination with a specific value for the ratio d/m). This result is incompatible with the occurrence of athermal nucleation due to pre-existing nuclei which was observed for the “type A” crystallites of lamellar $(Fe,Ni)/(Fe,Ni)_3B$ in [79]. A probable explanation could be that the amorphous ribbons prepared by melt-spinning in the present work contain only a negligible amount of pre-existing nuclei due to a much more efficacious quenching (see also [79]).

The observation of pure continuous nucleation is corroborated by the second

experimental series with an additional pre-annealing treatment: both datasets can be described consistently with a single kinetic model, only for the series with pre-annealing mixed nucleation with a considerable contribution of the site saturation mode results (Section 3.4.3.2). Interestingly, the pre-factors for continuous nucleation fitted separately for the two datasets are almost identical. This indicates that the pre-annealing treatment has no influence on the innate mode of nucleation, which thereby is validated to be continuous nucleation (apart from the decrease of its overall contribution upon pre-annealing), as well as on the nature of growth, since both datasets can be described by the same value of d/m .

The difference of kinetic models fitted to the data sets in Figure 3.4 and Figure 3.5 should be recognised. The comparable quality of the fit for the specimens without pre-annealing resulting from both model fits (Figure 3.4 vs. Figure 3.5 (a) and (b)) illustrates the power of the modular model with explicit expressions for n , Q_{eff} and K_0 (Figure 3.5) to identify, *in the same fit*, both the nucleation mode for the specimens without pre-annealing as practically pure continuous nucleation, and that of the specimens with pre-annealing as mixed nucleation. The model with constant kinetic parameters (Figure 3.4), by contrast, is limited in its applicability to experimental data with constant, single modes of nucleation (as indeed present for the series without pre-annealing) and only allows indirect inference of the operating modes of nucleation and growth (cf. discussion in Section 3.4).

The observed activation energy for nucleation $Q_N = 588 \text{ kJmol}^{-1}$ is considerably larger than the activation energy for growth $Q_G = 296 \text{ kJmol}^{-1}$. This may be understood recognising that the formation of a crystalline nucleus of specific composition in an amorphous matrix requires coordinated redistribution and ordering of several types of atoms in the amorphous bulk, whereas growth is realised by jumps of single atoms (across and) along the amorphous-crystalline interface of the growing lamellar colony with the amorphous matrix. The activation energy for growth $Q_G = 296 \text{ kJmol}^{-1}$ is somewhat larger than the activation energies for self-diffusion of Fe, $Q_{\text{D,Fe}} = 239 \text{ kJmol}^{-1}$ [86], and of Ni, $Q_{\text{D,Ni}} = 220 \text{ kJmol}^{-1}$ [87], in amorphous, relaxed $\text{Fe}_{40}\text{Ni}_{40}\text{B}_{20}$ below the glass transition temperature. Note that the development of a lamellar geometry with a very small interlamellar spacing (cf. Figure 3.3 (a) and (b)) is one way to establish phase separation at relatively low temperatures in reasonable times, albeit at the cost of generating a large contribution of interface energy [1].

The evolution of the growth exponents $n(t)$ and of the effective activation energies $Q_{\text{eff}} = f(n(t), Q_N, Q_G)$ (Figure 3.6) clearly shows the influence of the pre-annealing treatment: the transformation reaction in the pre-annealed specimens starts with pure site saturation with $n = d/m$ and $Q_{\text{eff}} = Q_G$. Then,

in the course of the reaction, n and Q_{eff} increase asymptotically towards the values for pure continuous nucleation, as indeed established for the specimens without pre-annealing (see above).

Recognising this change in effective activation energy from $Q_{\text{eff}} = Q_{\text{N}}$ to $Q_{\text{eff}} = f(n(t), Q_{\text{N}}, Q_{\text{G}})$, the variation in the values reported in the literature can be understood: depending on the number density of pre-existing nuclei generated during amorphous ribbon preparation, as a consequence of a more (or less) efficient quenching, different effective activation energies between $Q_{\text{eff}} = Q_{\text{G}}$ and the maximum value given by Equation (3.9) for pure continuous nucleation can operate. However, several reported effective activation energy values [80,83] are clearly below the activation energy for growth determined in this work which may be an artefact of the (surface-specific) evaluation method based on light microscopy [80], and can be caused by an inconsistent application of the JMAK equation [82], or can be due to compositional differences (including contaminations).

The change of the kinetic parameters due to a more or less pronounced contribution of pre-existing nuclei can also explain the various values reported in the literature for the growth exponent, with the additional reservation that the growth exponents in literature were derived by application of the classical JMAK equation and thus are biased by use of the differing (inappropriate for the case considered) impingement correction (cf. Table 3.1).

The value for the ratio of d/m determined in this work is about 2.4. Coupled growth to establish a lamellar microstructure can be rate-controlled by interface diffusion (along the front of the lamellar colony) following a linear growth law [88]. Thus the value of $d/m = 2.4$ obtained in the present work could be interpreted as linear growth ($m = 1$) in two dimensions ($d = 2$) along the interface (growth front) of the lamellar colony with the amorphous matrix combined with a contribution of non-linear growth (e.g. parabolic with $m = 1/2$) perpendicular to the lamellae (sidewise growth of the colony).

3.6 Conclusions

- The modular kinetic model can successfully be applied to describe the kinetics of isothermal crystallisation of amorphous $\text{Fe}_{40}\text{Ni}_{40}\text{B}_{20}$.
- The innate mode of nucleation for amorphous $\text{Fe}_{40}\text{Ni}_{40}\text{B}_{20}$ upon isothermal annealing is continuous nucleation.
- Growth occurs with a general growth ratio d/m of about 2.4, indicating linear growth in reduced dimensions.
- A so-called delayed impingement mode, as due to a non-random nucleus distribution, operates, which makes application of the classical JMAK equation impossible.
- By use of additional pre-annealing experiments, the effective activation energy, varying with time for the pre-annealed specimens, can be decomposed into the (genuinely constant) activation energies for nucleation $Q_{\text{N}} = 588 \text{ kJmol}^{-1}$ and growth $Q_{\text{G}} = 296 \text{ kJmol}^{-1}$.
- Varying values for the effective activation energy and the growth exponent as reported in the literature can be ascribed to varying contributions of pre-existing nuclei (due to more or less efficacious quenching upon melt spinning to produce the initially amorphous specimens) and/or to inappropriate application of the classical JMAK equation.

Acknowledgements

Dr A. Leineweber (Max Planck Institute for Intelligent Systems) is gratefully acknowledged for his assistance with Rietveld refinement and TOPAS. Two of the authors, Y. Ma and F. Liu, are grateful to the China National Funds for Distinguished Young Scientists (No. 51125002), the Natural Science Foundation of China (No. 51071127), the Fundamental Research Fund (No. JC201201) and the 111 Project (No. B08040) of Northwestern Polytechnical University.

Chapter 4

Phase Transformation Kinetics; Advanced Modelling Strategies

Bastian Rheingans, Eric J. Mittemeijer

Abstract

Phase transformations in the solid state are often heterogeneous and can be described by concurring modes of nucleation, growth and impingement. The classical Johnson-Mehl-Avrami-Kolmogorov-(JMAK-)model, although offering an easy-to-use description of the transformation kinetics, is limited to very specific cases of the transformation modes. Instead, a generalised modular model of phase transformation kinetics can be proposed that provides a flexible formalism adaptable to various modes of nucleation, growth and impingement. Due to its large versatility, the modular model approach can be easily applied for characterisation of phase transformation kinetics beyond the scope of classical JMAK(-type) modelling. Three different strategies recently employed for such advanced modelling are presented: (i) deliberate variation of the nucleation mode upon crystallisation of an Fe-Ni-B metallic glass in order to determine separate activation energies for nucleation and growth, (ii) incorporation of specific, dedicated modes for nucleation and growth kinetics for the allotropic hcp-fcc transformation in cobalt introducing driving-force dependent rates of transformation, (iii) implementation of quantitative microstructural data for the description of the precipitation kinetics in a super-saturated CuCo alloy.

4.1 Introduction

Phase transformations are a powerful tool to modify the microstructure and thereby optimise the properties of materials. Understanding of the kinetics of a phase transformation and the associated change in microstructure is a prerequisite to utilise this tool to full extent. In the solid state, phase transformations are often heterogeneous and can be described as resulting from three concurring mechanisms: the nucleation of product-phase particles, their growth and their impingement in later stages of the phase transformation (Figure 4.1). Particle nucleation and particle growth proceed with certain rates, while impingement is of geometric nature and a consequence of continued nucleation and growth: product particles cannot nucleate and grow in volume already transformed by other particles.¹

The available experimental information usually is a set of transformation curves: transformed fraction versus time for various temperatures or transformed fraction versus temperature for various heating/cooling rates. The classical approach to describe the kinetics, as exhibited by the transformation curves and in terms of (only special) modes of nucleation, growth and impingement, is the model due to Johnson, Mehl and Avrami, and Kolmogorov (the JMAK-model, [14,13,12]) for isothermal reactions and its equivalents, so-called JMAK-*type* models [1], for also isochronal heating or cooling (i.e. heating or cooling with constant rate). In the JMAK-model, the transformed volume fraction f as function of reaction time t at temperature T is expressed as

$$f(t, T) = 1 - \exp(-K^n t^n) = 1 - \exp\left(-K_0^n \exp\left(-\frac{n \times Q_{\text{eff}}}{RT}\right) t^n\right). \quad (4.1)$$

The characteristic kinetic parameters are the effective activation energy Q_{eff} , some effective mean of the separate activation energies of the nucleation and growth modes, and the growth exponent n , comprising information on the time dependence of particle nucleation and particle growth, as well as on the dimensionality of growth. The constant K_0 combines several pre-factors and R is the ideal gas constant. Values for Q_{eff} and n abound in the literature and have usually been determined with short-cut methods using fixed values of transformation time, temperature or transformed fraction (e.g. Kissinger-like methods for the isochronal case [20]; see also [1]). However, application of the JMAK(-type) approach is subjected to severe constraints [1]: A principal condition is that the kinetics must be governed by a *constant* effective activation energy and a *constant* growth coefficient. This entails that the mechanisms of

¹This is called “hard impingement”; for “soft impingement”, see Section 4.5.

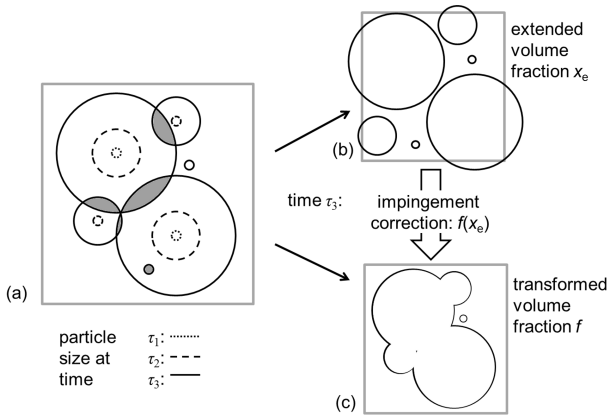


Figure 4.1: Schematic presentation of the impingement approach: Particles are first assumed to nucleate and grow without any “interference” of other particles (a), yielding the extended volume fraction x_e (b). The impingement relation corrects for the particle “interference” (the grey areas at $t = \tau_3$ in (a)), yielding the transformed volume fraction $f(x_e)$, i.e. the volume fraction the particles can actually assume (c).

nucleation and growth must not change during the transformation. In addition, the impingement is assumed to be random, i.e. product particles must be distributed randomly throughout the parent phase and must grow isotropically. A violation of these prerequisites is usually less obvious when one of the above indicated short-cut methods is employed to determine values for Q_{eff} and n , instead of fitting the entire set of transformed fraction curves available, but then the resulting kinetic parameters can be very erroneous. This has led to publication of many meaningless kinetic data in the literature (see, e.g., discussion in [89]).

To transcend the limited range of applicability of the JMAK-approach, a generalisation to a flexible formulation has been proposed which allows the combination of a range of modes of nucleation, growth and impingement in a modular way [11, 90]. This paper intends to give an overview of this approach by presenting a few cases where different strategies are followed in the application of the modular model. With the extended kinetic “toolbox” provided by the modular model (outlined in Section 4.2), a variety of problems in the analysis of phase transformation kinetics can be tackled:

A prime example is the time dependency of the kinetic parameters $Q_{\text{eff}}(t)$ and $n(t)$, as often observed in experiments, but mostly ignored or left unexplained. Such behaviour can be understood and described consistently within

the modular model, e.g. as the outcome of a combination of different nucleation modes. Moreover, the time dependency of the kinetic parameters and the underlying variation in kinetic modes can be utilised to determine the separate, genuinely *constant*, activation energies of nucleation and growth. This strategy is presented in Section 4.3 for the kinetic analysis of the crystallisation of a metallic glass where a variation of the nucleation mode was introduced deliberately into the experiments.

For some types of phase transformations, a (relatively) good theoretical understanding of the mechanisms of nucleation and growth exists. Here, the modular model can serve as a flexible framework to introduce and combine these specific descriptions for the transformation modes (this usually leads to a non-closed, non-analytical formulation of the transformed fraction). This type of approach provides an efficacious description of the kinetics of the allotropic hcp \rightarrow fcc transformation in cobalt, as outlined in Section 4.4.

Phase transformations are characterised not only by the kinetics of transformation, but also by the change in microstructure upon transformation. Frequently, for a transformation model good agreement can be achieved with only either the experimentally observed transformation kinetics or the experimentally observed change in microstructure. Simultaneous description of both kinetics and microstructural evolution is often difficult, requiring recognition of spatial variation of driving force and interface mobility [91]. An example of the direct implementation of the microstructural evolution into the kinetic model is presented in Section 4.5 for the precipitation of second-phase particles from a supersaturated alloy.

4.2 The modular model approach

The modular approach allows the combination of various modes of nucleation, growth and impingement in a flexible, adaptive way: The extended volume fraction, i.e. the volume fraction that second-phase particles would assume if they could nucleate and grow without interference with other particles (cf. Figure 4.1), is calculated according to

$$x_e(t) = \int_0^t \dot{N}(\tau) Y(t, \tau) d\tau, \quad (4.2)$$

where $\dot{N}(\tau)$ is the nucleation rate at time τ and $Y(t, \tau)$ the volume of a particle at time t that had nucleated at time τ .

The particle volume is expressed as

$$Y(t, \tau) = g \left(\int_{\tau}^t v dt' \right)^{d/m} \quad (4.3)$$

with the growth rate v , the growth mode parameter m , the dimensionality d of growth and a geometry factor g . The values of m and d can be chosen to describe different types of growth: $m = 1$ in case of “linear” growth (i.e. for isothermal transformations, the transformed volume grows proportional to t in one dimension; this usually corresponds with interface-controlled growth) and $m = 2$ in case of “parabolic” growth (i.e. for isothermal transformations, the transformed volume grows proportional to $t^{1/2}$ in one dimension; this usually corresponds with volume-diffusion controlled growth), and $d = 1, 2, 3$ for growth in one, two or three dimensions. The growth rate v can be identified as the growth velocity (velocity of the product/parent interface) in case of interface-controlled growth ($m = 1$) and as the diffusion coefficient in case of diffusion-controlled growth ($m = 2$).

Finally, to transfer the extended volume fraction into the actually transformed volume fraction f , with $0 \leq f \leq 1$, an impingement correction has to be introduced that describes the relation between x_e and f (Figure 4.1).² For random spatial distribution of particles and isotropic growth, the impingement correction can be derived analytically [12, 13] yielding

$$\frac{df}{dx_e} = (1 - f), \quad (4.4)$$

and, after integration

$$f = 1 - \exp(-x_e). \quad (4.5)$$

To describe an impingement enhanced or delayed as compared to random impingement, (partly empirical) relations with an additional model parameter can be used.

Only for the isothermal case, for random impingement in combination with either the pure “site saturation” (or “pre-existing nuclei”) nucleation mode ($\dot{N}(\tau)$ is non-zero only at $\tau = 0$) or the pure continuous nucleation mode ($\dot{N}(\tau)$ is a constant), and constant v , the classical JMAK-equation (Equa-

²The modular model and also the original JMAK-model can thus be classified as mean-field kinetic models with the transformed fraction, characterising the state of the transformation reaction, as function of the extended volume fraction x_e , the independent variable, or state variable, cf. [63]. The impingement correction constitutes the mathematical relation between f and x_e .

tion (4.1)) is obtained.

A flexible kinetic model inevitably introduces the danger of arbitrariness: a model description, including a number of adaptable fit parameters, may exhibit an excellent numerical agreement with an experimental dataset, but yield physically meaningless values for these fit parameters. Obviously, such non-physical solutions can be suppressed by imposing constraints for transformation modes which are compatible with general features of the investigated transformation, e.g. compatible with the parent and/or the product microstructure(s) (see, especially, Section 4.5). Further, to improve the significance of the kinetic parameters, simultaneous fitting to all experimental data sets is mandatory, i.e. fitting, simultaneously, to all transformation curves recorded at different temperatures or at different cooling/heating rates. This contrasts with the often followed practice in the literature where values for the kinetic parameters are obtained by fitting to only a single transformation curve.

In the following, the general framework of the modular model as outlined above is applied to very different cases of phase transformation, demonstrating the versatility of the proposed approach.

4.3 Time dependency of kinetic parameters: modelling of the crystallisation of amorphous $\text{Fe}_{40}\text{Ni}_{40}\text{B}_{20}$

Crystallisation of metallic glasses (or its prevention) upon annealing is a topic of wide interest covered by very many publications (see, e.g., [27]). Knowledge on the kinetics of crystallisation allows for instance to assess the operating conditions of an amorphous metal in practical use, or to tailor the degree of crystallisation for enhancement of material properties. Metal alloys in the amorphous state can be achieved by rapid quenching from the melt. This state is a metastable one: Upon temperature increase, nucleation and growth of the more stable crystalline phase(s) set in. This means that the crystallisation reaction is controlled by the thermal activation of nucleation and growth.

Upon isothermal annealing of amorphous $\text{Fe}_{40}\text{Ni}_{40}\text{B}_{20}$ at elevated temperatures, this alloy crystallises forming grains with a lamellar microstructure of two crystalline phases (Figure 4.2) [89].

Annealing experiments were performed in a power-compensating differential scanning calorimeter (DSC) at various annealing temperatures where the crystallisation reaction occurs within practicable time range. The transformed fraction can be derived from the measured annealing-time dependent heat release upon crystallisation [89]. The transformation-rate curves, df/dt vs. t , obtained for the different annealing temperatures, are shown in Figure 4.3.

In order to analyse the kinetics of the transformation, the modes of nucle-

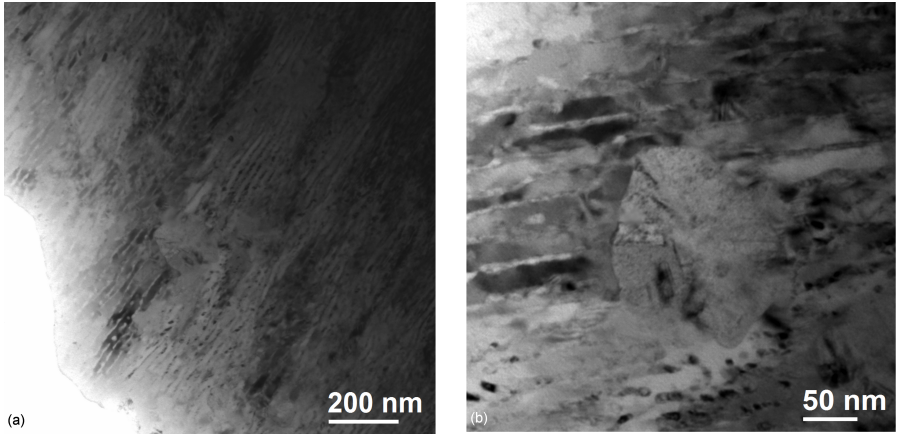


Figure 4.2: Crystallisation of $\text{Fe}_{40}\text{Ni}_{40}\text{B}_{20}$ upon isothermal annealing [89] - Bright field TEM images showing the microstructure of a specimen after completed crystallisation at $T = 669\text{ K}$. The microstructure consists of nano-scaled grains with a lamellar microstructure of two crystalline product phases, a face-centered cubic (Fe,Ni) solid solution and an orthorhombic $(\text{Fe,Ni})_3\text{ B}$ -phase.

ation and growth and the impingement correction have to be defined. According to classical nucleation theory, the rate of nuclei formation is dominated by two energies, the nucleation barrier ΔG^* , which depends on the driving force available for transformation, and the constant activation energy for nucleation Q_N :

$$\dot{N}(T) \propto \exp\left(-\frac{\Delta G^* + Q_N}{RT}\right) \quad (4.6)$$

For a metallic alloy in the amorphous state, the driving force for crystallisation is very high, hence $\Delta G^* \approx 0$. The nucleation rate can then be described by a continuous nucleation rate

$$\dot{N}(T) = N_0 \exp\left(-\frac{Q_N}{RT}\right), \quad (4.7)$$

where N_0 is a constant pre-factor. For large chemical driving forces, also the growth rate can be expressed with an Arrhenius term [1]

$$v(t, T) = v_0 \exp\left(-\frac{Q_G}{RT}\right), \quad (4.8)$$

where v_0 is again a constant pre-factor and Q_G is the constant activation energy for growth. Thus, both the nucleation mode and the growth mode can be formulated as rates (predominantly) controlled by thermal activation. The modular model then allows to express the extended volume fraction, Equation (4.2), in a concise way ([11], compare Equation (4.1)):

$$x_e(t, T) = \alpha^n K_0^n \exp\left(-\frac{nQ_{\text{eff}}}{RT}\right), \quad (4.9)$$

where α equals t for isothermal annealing (and $(RT^2)/(Q_{\text{eff}}\Phi)$ for isochronal annealing [1], with Φ as the constant heating rate). K_0 combines several pre-factors. The growth exponent n includes the ratio d/m , characteristic for the growth mode, as well as information on the nucleation mode. For continuous nucleation as in the present case, n equals $d/m + 1$; for the nucleation mode of site-saturation/pre-existing nuclei at $t = 0$, n equals d/m . The effective activation energy Q_{eff} is composed of the weighted sum of the separate activation energies of nucleation and growth,

$$Q_{\text{eff}} = \frac{(n - d/m)Q_N + d/mQ_G}{n}, \quad (4.10)$$

which simplifies to $Q_{\text{eff}} = Q_G$ in case of pre-existing nuclei.

Combination of Equation (4.9) with an appropriate impingement correction (here delayed impingement) then yields an expression for the transformed volume fraction and the rate of transformation as function of the annealing time.

In studies on the crystallisation of amorphous metals often *non-constant*, time-dependent kinetic parameters have been presented, frequently determined with short-cut methods such as Kissinger-like methods for Q_{eff} upon isochronal annealing (which presume constant kinetic parameters) [63]. The question of the origin of time dependency of the kinetic parameters is then either simply ignored, or the observation is explained only qualitatively as the result of a change in the operating modes of transformation. A variation of nucleation mode during the transformation can for instance be caused by the presence of pre-existing nuclei of crystalline phases at (effectively) the start of transformation, resulting from insufficiently powerful quenching, or by preferential nucleation at inhomogeneities (e.g. surfaces). As a consequence a change of nucleation mode can occur during the transformation: away from “site saturation” prevailing in the first stage of transformation towards the innate mode of nucleation. This can explain the large range of kinetic parameters sometimes reported for one and the same material in the literature

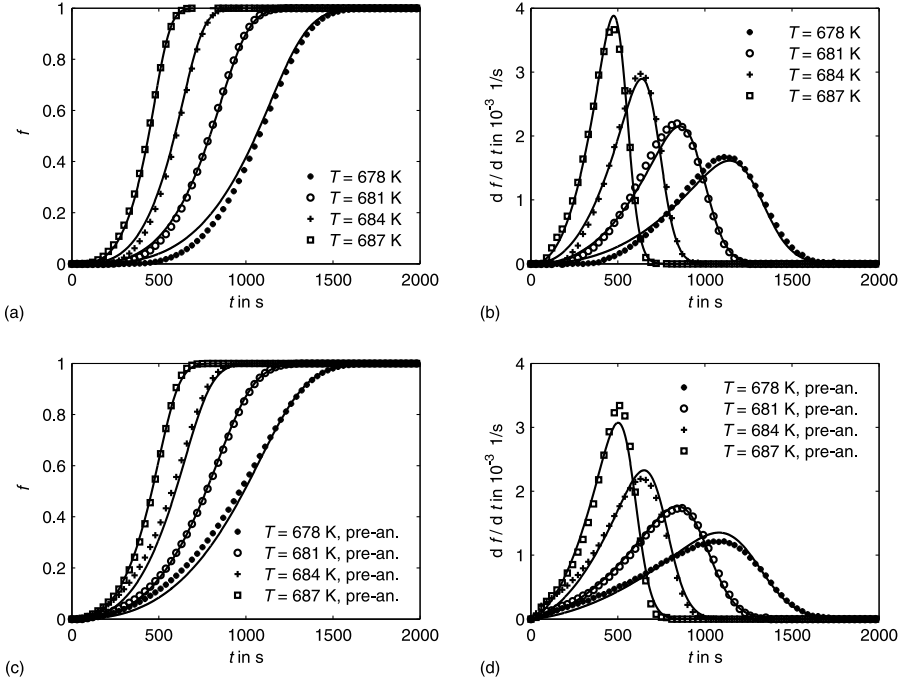


Figure 4.3: Crystallisation of amorphous $Fe_{40}Ni_{40}B_{20}$ upon isothermal annealing [89] - transformed fraction curves and transformation-rate curves for annealing without pre-annealing treatment ((a) and (b)) and after application of a pre-annealing treatment at $T_{pre} = 658 K$ for 1200 s ((c) and (d)). Markers: experimental data, solid lines: model fit. The modular model was fitted to all transformation rate curves of both data sets simultaneously, only allowing the relative contributions of continuous nucleation and pre-existing nuclei (site saturation at $t = 0$) to be different.

(cf. [89]). The results of an analysis of transformation kinetics inconsiderately presuming *constant* kinetic parameters should therefore be treated with caution.

Here, the modular model offers a consistent way to model transformation kinetics with time-dependent kinetic parameters: For a large number of combinations of nucleation modes and growth modes, the extended volume fraction can be described by Equation (4.9), now with explicit mathematical expressions for the time-dependent kinetic parameters $Q_{\text{eff}}(t)$ and $n(t)$. Fitting of the modular model with a (reasonably chosen) combination of modes of nucleation and growth to, simultaneously, a set of transformed fraction curves then allows to describe the time-dependent behaviour of $Q_{\text{eff}}(t)$ and $n(t)$. Moreover, it also allows to determine the relative contributions of the nucleation and growth modes, e.g. in the effective activation energy: As exhibited by Equation (4.10), a specific value for the effective activation energy is compatible with an infinite number of combinations of values for the activation energies of nucleation and growth. In the general case it is therefore not possible to determine the separate activation energies of these modes from a model fit. However, if a (pronounced) variation in the operating modes (and thus of Q_{eff} and n) occurs, these contributions can be separated upon model fitting.

In the present example [89], the isothermal crystallisation kinetics of $\text{Fe}_{40}\text{Ni}_{40}\text{B}_{20}$ could be described well by constant kinetic parameters. Thus a separate determination of the effectively constant activation energies of nucleation and growth was not possible based on this experimental dataset. Therefore, a variation of the operating modes of nucleation was generated deliberately: By pre-annealing of the amorphous alloy at a low temperature, before the main annealing step at higher temperatures leading to crystallisation, nuclei of the crystalline product phase(s) can be generated. Since these pre-existing nuclei are already present at the beginning of the crystallisation reaction at higher temperature, they can immediately grow once the main (elevated) annealing temperature has been imposed. As a consequence, in the initial stage of transformation $Q_{\text{eff}} \approx Q_{\text{G}}$ and $n \approx d/m$, as discussed above. Upon continued transformation, the contribution of the prevailing thermally activated nucleation mode (in this case “continuous nucleation”, cf. Equation (4.7)) becomes more and more dominant, leading to a strong time/temperature dependency of Q_{eff} and n (see Figure 4.4).

Extended kinetic modelling was then performed by fitting the modular model *simultaneously* to all transformation-rate curves, each at different isothermal annealing temperature, of *both* experimental series, with and without pre-annealing treatment (see Figure 4.3). For both datasets, the same kinetic model was employed but with separately adjustable contributions of pre-

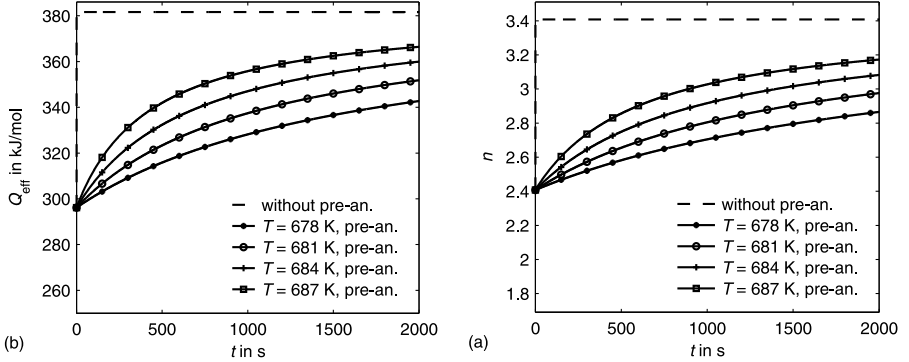


Figure 4.4: Crystallisation of $\text{Fe}_{40}\text{Ni}_{140}\text{B}_{20}$ upon isothermal annealing [89] - time dependencies of (a) the effective activation energy Q_{eff} and (b) the growth exponent n for the series with pre-annealing treatment (curved solid lines with markers) as compared to the constant values for the series without pre-annealing (dashed lines). For the series with pre-annealing, Q_{eff} and n *initially* assume the values corresponding to pre-existing nuclei $Q_{\text{eff}} = Q_G$ and $n = d/m$ (i.e. growth-only reaction). Later, the contribution of continuous particle nucleation becomes increasingly dominant. Such time/stage of transformation-dependent behaviour of Q_{eff} and n implies that erroneous results are obtained if the kinetic analysis is performed assuming *constant* Q_{eff} and n . This is a common source of error in the literature when experimental data is influenced by non-constant modes of transformation, e.g. as consequence of a less efficacious quench from the liquid to the solid amorphous state.

existing nuclei and continuous nucleation. Due to the strong variation in transformation kinetics as introduced by the pre-annealing treatment (note the pronounced time/temperature dependence of the parameters Q_{eff} and n , Figure 4.4), the genuinely *constant*, separate activation energies of nucleation and growth could successfully be determined.

4.4 Dedicated, specific descriptions for the nucleation and growth modes: modelling of the hcp \rightarrow fcc transformation in Co

Pure Co shows an allotropic transformation at around 670 K with a hexagonal close-packed (hcp) low temperature phase, denoted *martensite*, and a cubic close-packed (fcc) high temperature phase, denoted *austenite*. The transformation occurs diffusionless and shows an athermal nucleation behaviour, i.e. nucleation of the new phase is realised instantaneously upon heating above the austenite start temperature or cooling below the martensite start temperature. Obviously, in such a case it is not possible to achieve high degrees of undercooling (or overheating) resulting in large chemical driving forces for transformation, in contrast to the amorphous metal obtained upon quenching from the liquid state presented in Section 4.3. Therefore, for such cases of moderate or small driving force, the rates of nucleation and growth cannot be described solely by Arrhenius terms with constant activation energies.³ In these cases, the kinetic analysis requires the implementation of rates depending on the net driving force ΔG for transformation as function of the degree of undercooling or overheating ΔT [44].

The transformation from the hcp to the fcc crystal structure, and vice versa, can be described by a dislocation-mediated mechanism [92]: A “perfect” dislocation in the hcp structure can dissociate into two so-called Shockley partial dislocations, creating a stacking fault associated with a certain stacking fault energy. This stacking fault introduces a local fcc-type layer stacking within the parent hcp structure (Figure 4.5). In the hcp Co phase, arrays of ordered Shockley partial dislocations (“ordered” means one dislocation at every second close packed plane) occur with a certain distribution of array size. When, upon heating hcp Co, the austenite start temperature is surpassed, the stacking fault arrays serve as nuclei for the (fcc) austenite phase. The higher the overheating, the smaller the arrays can be to serve as a nucleus of the new phase, i.e. the critical array size decreases with increased overheating due to

³Indeed, application of a (JMAK(-type)) kinetic analysis, based on rates for nucleation and growth controlled only by thermal activation as characterised by an activation energy, leads to gravely erroneous results (cf. [54]).

the higher chemical driving force. The number of nuclei $N(T(t))$ thus activated at a certain temperature can be described by the empirical equation [93]

$$N(T(t)) = N_{\text{tot}} \exp(-n^*(\Delta T)), \quad (4.11)$$

where N_{tot} is the total number of Shockley partial dislocation arrays and $n^*(\Delta T)$ is the critical (minimal) number of Shockley partial dislocations within an array at a given degree of overheating ΔT .

The nucleus of the new phase (the ordered array of Shockley partial dislocations) can then grow by lateral dislocation glide, i.e. by one-dimensional growth. For small overheating as in the present case, the growth velocity is a function of the net driving force $\Delta G(\Delta T)$ available for growth of a particle and is given by [1]

$$v(T(t)) = M(-\Delta G(\Delta T(t))) = M_0 \exp\left(-\frac{Q_G}{RT}\right)(-\Delta G(\Delta T(t))), \quad (4.12)$$

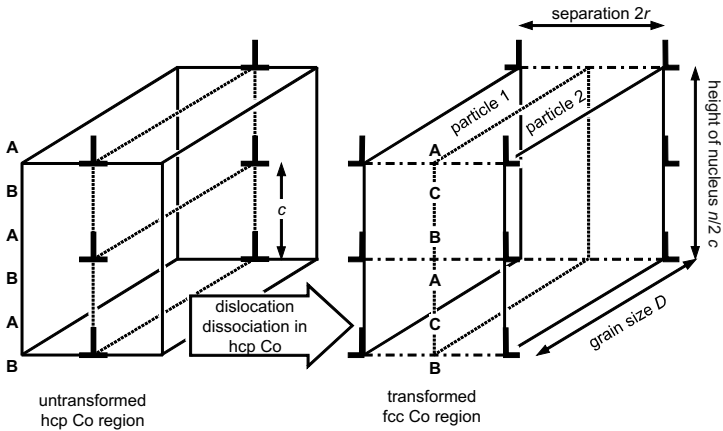
where M is the mobility, with an Arrhenius-type temperature dependency with constant pre-factor M_0 and constant activation energy Q_G . As compared to the example presented in Section 4.3, the growth rate now depends on the time- and temperature-dependent driving force determined by the degree of undercooling ΔT .

After having defined explicit descriptions of the kinetics of nucleation and growth, the extended volume fraction can be calculated (cf. Equation (4.2); note that Equation (4.9) is not valid here), and, introducing an adequate impingement correction (in this case anisotropic due to lateral growth, implying enhanced impingement as compared to isotropic growth; cf. Equation (4.4)), the transformed volume fraction f can be calculated.

Experimental investigation of the hcp→fcc and the reverse fcc→hcp transformation was performed by DSC upon heating and upon cooling, respectively. Model fitting was only applied to the hcp→fcc transformation curves obtained upon heating due to the problematic calibration of DSC curves upon cooling [44].

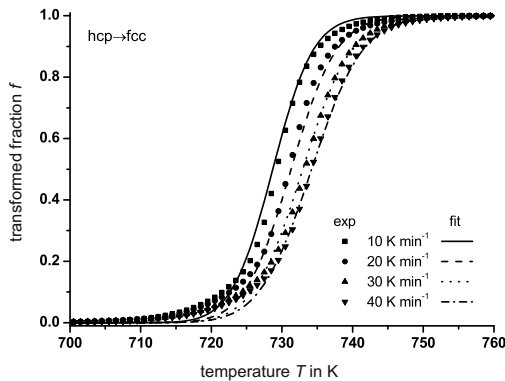
By fitting the modular model with the explicit expressions for nucleation and growth to the experimental transformation rate curves for all heating rates simultaneously (see Figure 4.5), the kinetic parameters characteristic for this phase transformation could be determined: the stacking fault energy, defining nucleation, and the activation energy for dislocation glide, defining growth.

This example demonstrates that the modular model is well suited to serve as a flexible framework for incorporation of specified kinetic formulations for nucleation and growth modes, e.g. in situations where the original JMAK(-



⊥: perfect dislocation, ⊥: Shockley partial dislocation

(a)



(b)

Figure 4.5: Allotropic hcp \rightarrow fcc transformation in Co [94] - (a) schematic representation of the transformation mechanism. A perfect dislocation in the hcp structure can dissociate into two Shockley partial dislocations generating a stacking fault of fcc-type stacking in between. An ordered array of Shockley partial dislocations (one at each second close-packed plane) can transform by dislocation glide the hcp structure into the fcc structure, and vice versa. Both the activation of dislocation arrays as nuclei of the new phase and the rate of growth by dislocation glide depend strongly on the driving force available and thus on the extent of undercooling/overheating. (b) Transformed fraction curves derived from the DSC measurements upon heating. Markers: experimental data, solid lines: model fit. The modular model, including undercooling-dependent modes of nucleation and growth, was fitted to all transformed fraction curves simultaneously.

type) approach cannot be applied at all.

4.5 Incorporation of microstructural information: modelling of the precipitation kinetics of Co in CuCo

Precipitation of second-phase particles in a supersaturated matrix is a frequently used process to enhance the mechanical, electric or magnetic properties of a material. The binary system Cu-Co has often been investigated in the past as a model system for studying solid-solid phase transformation kinetics (e.g. [32,61,40]). Upon annealing of supersaturated Cu-rich alloys within the two-phase region, spherical, coherent Co-rich particles are formed within the Cu-matrix (see Figure 4.6 (a)). Kinetic analyses in the past focused on the precipitation reaction upon isothermal annealing at small to medium degrees of undercooling. Under such conditions, nucleation and growth are controlled by both thermal activation (cf. Section 4.3) and the available chemical driving force for the transformation (cf. Section 4.4). Kinetic analysis on the basis of isochronal annealing of quenched, supersaturated alloys implies that at least initially a very high degree of supersaturation, corresponding to a very high chemical driving for precipitation, is imposed. In that case nucleation and growth are controlled by thermal activation only, with constant activation energies for nucleation and growth. This experimental approach therefore allows to focus on the role of the activation energies for nucleation and growth; the chemical driving force does not influence the nucleation and growth rates. Thus, the rate of nucleus formation can be expressed by Equation (4.7) and the growth rate by Equation (4.8), introducing the activation energies Q_N and Q_G for nucleation and growth, respectively.

Upon formation of a Co-rich particle, the Cu-rich matrix around the particle is gradually depleted of solute. This leads to particle growth controlled by (long-range) volume diffusion of solute atoms, for a spherical particle upon isothermal growth resulting in a parabolic growth law⁴ [25,26]. Such growth behaviour can be described by setting the dimensionality $d = 3$ and the growth parameter $m = 2$ in Equation (4.3).

The occurrence of solute depletion upon formation of solute-rich particles within the matrix phase requires some re-consideration of the impingement: impingement as introduced in Section 4.2 is originally derived from the “interference” of (massive) product particles [12,13]: “hard” impingement. In case of the above described formation of precipitates within a matrix supersaturated

⁴i.e. the particle radius increases with $r \propto \sqrt{v(T(t))t}$, note that for isochronal annealing the resulting growth law is no longer strictly parabolic since $v(T(t))$ is a function of temperature and thus also of time; cf. discussion below Equation (4.3)

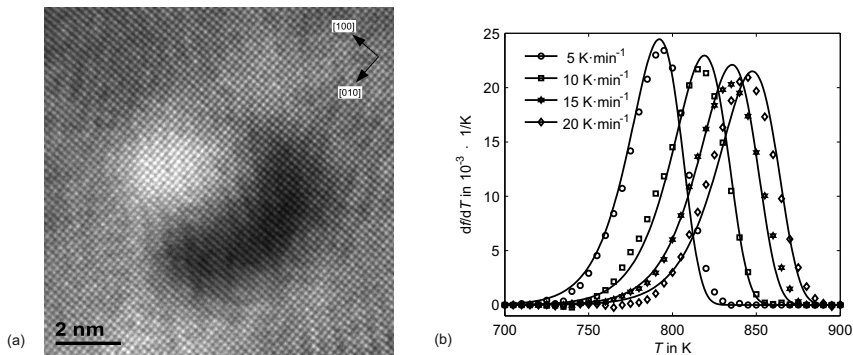


Figure 4.6: Precipitation of Co-rich particles in dilute CuCo alloys [94] - (a) high resolution TEM image of a spherical Co-rich particle embedded in a Cu-rich matrix (Cu-2.0 at.% Co alloy annealed for 60 min at 843 K). The particle is completely coherent with the matrix. (b) Transformation-rate curves derived from DSC measurements of quenched Cu-0.95 at.% Co alloy upon isochronal heating with various heating rates. Markers: experimental data, solid lines: model fit. The modular model was fitted to all transformation-rate curves simultaneously with the additional, microstructural constraint that the experimentally determined particle density is reproduced.

with solute(s) (in dilute systems the precipitates are usually well separated) impingement can be considered as the “interference” of diffusion fields, i.e. of solute-depleted regions, developing around the particles: “soft” impingement.

For precipitation reactions, the rates of nucleation and growth are a function of the degree of supersaturation. Typically, nucleation is much more sensitive towards a decrease of supersaturation: particle nucleation can effectively come to a halt long before the solute concentration in the matrix approaches its equilibrium value. The further progress of the precipitation reaction is then carried by continuing growth of the precipitate particles formed until that stage, evolving to solely coarsening in later stages. Due to the strong increase in transformed volume during the initial stage of *concurring* nucleation and growth, this first stage may be modelled as a separate reaction, ending when the matrix is depleted to such extent that nucleation effectively comes to a halt. Assuming random distribution of nuclei, soft impingement can then be treated analogously to hard impingement (Equation (4.4)): each precipitate particle is surrounded effectively by a solute-depleted shell such that all precipitate particles with their surrounding solute-depleted shells fill at the end of the nucleation-and-growth stage the entire volume of the specimen. The degree of depletion at the stage when nucleation effectively comes to a halt is introduced in form of a scaling factor for the extended volume fraction

(Equation (4.9); cf. e.g. [3]).

Having thus defined the modes of nucleation and growth and the nature of impingement upon precipitation, the transformed fraction and the transformation rate as function of $T(t)$ can be calculated using Equation (4.9) and Equation (4.4). Fitting this model to, simultaneously, all experimentally determined transformation-rate curves, each recorded at different heating rate, then allows to determine the effective activation energy Q_{eff} and the growth exponent n .

Isochronal annealing experiments were performed on Cu-0.95 at.% Co alloy quenched from the single-phase region, using a power-compensating DSC with a set of constant heating rates of $\Phi = (5, 10, 15, 20) \text{ K min}^{-1}$ [94]. The transformed fraction was derived from the measured annealing-time dependent heat release upon decomposition. The transformation-rate curves, df/dT vs. T , obtained for the different heating rates are shown in Figure 4.6 (b).

As discussed in Section 4.3, a specific value for Q_{eff} is compatible with an infinite number of combinations of values for the activation energies for nucleation, Q_{N} and growth, Q_{G} . The product microstructure, as characterised by number and size of the product particles, is defined by the rates of nucleation and growth, and thus by the values and the ratio of these activation energies [95]. Hence, a certain value for the effective activation energy is not specific for the resulting microstructure. This renders the presentation of solely a value for the effective activation energy, as is very often done, into an inadequate characterisation of a phase transformation that expresses itself by both its kinetics and by the resulting microstructural evolution.

Evidently, the quality of the kinetic description is increased considerably if microstructural data are taken into account, as well. This can, in the present example, be realised simply by recognising that the nucleation rate corrected for impingement yields the effective product-particle density:

$$N_{\text{eff}}(t, T) = \int_{t_0}^t \dot{N}(\tau) (1 - f(\tau)) d\tau. \quad (4.13)$$

The density $N_{\text{eff,exp}}(t, T)$ of the Co-rich particles attained at a certain (t, T) can be determined by e.g. transmission electron microscopy (TEM). Therefore, specimens upon reaching the end of the nucleation-and-growth stage (i.e. upon completion of the peak signal in the DSC curve) were quenched and analysed using TEM. The value of the product-particle density $N_{\text{eff}}(t = t_{\text{end}}, T = T_{\text{end}})$ is then introduced as an additional constraint to be fulfilled in the fitting procedure. Since this additional boundary condition only depends on the nucleation mechanism, whereas Q_{eff} depends on both the nucleation mechan-

ism and the growth mechanism, it is now possible to determine the separate activation energies for nucleation Q_N and growth Q_G by fitting the modular model to the experimental data for the transformation rate subject to the additional microstructural constraint given by Equation (4.13). In this way the results shown in Figure 4.6 (b) have been obtained.

With the separate activation energies, Q_N and Q_G , now at hand, it is not only possible to describe the overall kinetics of the transformation, but also to characterise and predict the microstructural evolution during the precipitation reaction, e.g. allowing the optimisation of the particle density and the particle size for a specific application.

4.6 Conclusion

Many solid state phase transformations are heterogeneous and can be constituted of the three concurring mechanisms nucleation, growth and impingement. The classical approach to model the corresponding transformation kinetics, the JMAK(-type) approach, is severely restricted in its applicability as very specific conditions for the nucleation, growth and impingement modes have to be satisfied. Here, the modular model constitutes a much more flexible framework: The modular approach can be easily adopted to a large variety of different phase transformations by introducing adequate model descriptions for nucleation, growth and impingement for the transformation under consideration. Beyond the determination of the classical JMAK kinetic parameters, i.e. the effective activation energy and the growth exponent, which is routinely (and often erroneously or unjustifiedly) performed in the literature, the modular model provides the means for a much more efficacious modelling of phase transformation kinetics.

Examples presented in this paper include (i) the modelling of time/temperature-dependent kinetic parameters, as the effective activation energy Q_{eff} and the growth coefficient n , and the determination of separate activation energies for nucleation and growth, (ii) the implementation of specific models for modes of nucleation and growth beyond the adoption of Arrhenius-type rate dependencies, and (iii) the inclusion of quantitative information on the microstructure into the kinetic modelling.

Application of such advanced strategies of modelling transformation kinetics allows dedicated choice of the process variables and thus optimisation of the resulting microstructure and material properties, i.e. tuned utilisation of phase transformations in practice.

Chapter 5

Modelling Precipitation Kinetics: Evaluation of the Thermodynamics of Nucleation and Growth

Bastian Rheingans and Eric J. Mittemeijer

Abstract

Modelling of (solid-state) precipitation kinetics in terms of particle nucleation and particle growth requires evaluation of the thermodynamic relations pertaining to these mechanisms, i.e. evaluation of the nucleation barrier and of the Gibbs-Thomson effect. In the present work, frequently occurring problems and misconceptions of the thermodynamic evaluation are identified and a generally valid, practical approach for a combined analysis of the thermodynamics of nucleation and growth, with regard to kinetic modelling, is proposed based on the fundamental thermodynamic equilibrium consideration in a particle-matrix system. A computationally efficient method for numerical determination of the thermodynamic relations is presented which allows an easy and flexible implementation into kinetic modelling.

5.1 Introduction

The dispersion of small second-phase particles within a parent-phase matrix, e.g. as resulting from a solid-state precipitation reaction, strongly influences the properties of the two-phase system. In materials science, precipitation reactions are therefore widely used as a method to enhance materials performance in numerous fields of application [1]. Precise control of the reaction kinetics allows to tailor the microstructure evolving upon precipitation and thus to tune the material properties.

Upon precipitation, particles of a solute(s)-rich β phase are formed within an α -phase matrix initially supersaturated in solute(s), leaving behind a solute(s)-depleted α -phase matrix. The kinetics of the precipitation reaction, typically described in terms of nucleation and growth of precipitate particles, strongly vary with the degree of solute supersaturation, i.e., at constant temperature,

with phase composition. In order to account for this effect in a model for precipitation kinetics the kinetics must be coupled to the thermodynamics of the alloy system. The numerical efficiency of the kinetic model and the quality of its results are therefore directly linked to the evaluation of the system's thermodynamics. Typical examples are models of Kampmann-Wagner-numerical (KWN)-type [15] (see e.g [96–99] and Section 5.4): In this frequently applied type of modelling approach, the evolution of the particle size distribution is computed on the basis of numerical integration of a composition-dependent nucleation rate and a size- and composition-dependent growth rate for discrete time steps and discrete particle-size classes. Such models thus involve numerous evaluations of thermodynamic relations, unfortunately until now usually using incompatible thermodynamic models for nucleation and growth (see below). The present work proposes a practical route for the thermodynamically correct and numerically efficient coupling of kinetic model and thermodynamic description.

In terms of thermodynamics, formation and stability of a precipitate-phase particle are (in the simplest case) defined by two counteracting factors: (i) The release of energy due to the decomposition of the supersaturated matrix phase into solute-depleted matrix phase and solute-rich precipitate phase. This release of energy can be described as a difference of chemical Gibbs energies $G_c^j(x^j)$ of the (homogeneous) phases $j = \alpha, \beta$, defined by their respective compositions x^j . (ii) The increase in energy due to the development of a particle-matrix interface¹.

In the rate equations for nucleation and growth as used in KWN-type kinetic models, this stability consideration is represented by two different concepts: the energy barrier for nucleation and the Gibbs-Thomson effect, affecting the growth (rate) of a particle. In the classical theory of nucleation [5, 6], the rate of nucleation \dot{N} is dominated by an energy barrier ΔG^* for formation of a particle of critical size r^* above which the particle is stable:

$$\dot{N} \propto \exp\left(-\frac{\Delta G^*}{kT}\right), \quad (5.1)$$

where k and T denote the Boltzmann constant and the absolute temperature, respectively. For the case of a precipitation reaction, ΔG^* and r^* are functions of the change in chemical Gibbs energy $\Delta g_c(x^{\alpha,m}, x^{\beta,p})$ upon nucleation (with $-\Delta g_c(x^{\alpha,m}, x^{\beta,p})$ being the chemical driving force for nucleation) for given compositions $x^{\alpha,m}$ and $x^{\beta,p}$ of the α -phase matrix and the β -phase precipitate, respectively, and of the interface energy γ per unit area,

¹Within the scope of this work, only the case of an, in the Gibbsian sense, “sharp” interface, i.e. an interface with a width small compared to the size of the particle will be considered.

i.e. $\Delta G^* = \Delta G^*(\Delta g_c(x^{\alpha,m}, x^{\beta,p}), \gamma)$ and $r^* = r^*(\Delta g_c(x^{\alpha,m}, x^{\beta,p}), \gamma)$, thus reflecting the two competing energy contributions. Growth of a solute-rich particle leads to solute depletion of the surrounding matrix; particle growth can then (in any case eventually) become rate-controlled by solute diffusion through the solute-depleted matrix towards the particle. The growth rate of a spherical particle of radius r in a binary² system A-B is then often described by [25, 26]

$$\frac{dr}{dt} = \frac{x^{\alpha,m} - x^{\alpha,int}}{k' x^{\beta,int} - x^{\alpha,int}} \frac{D}{r}, \quad (5.2)$$

with the diffusion coefficient D of the solute component in the matrix and the atom fractions³ of solute $x^{\alpha,m}$ in the α -phase matrix remote from the particle, and $x^{\alpha,int}$ and $x^{\beta,int}$ in the α -phase matrix and in the β -phase particle at the particle-matrix interface; the factor k' accounts for the difference in molar volume of the α phase and the β phase. For $x^{\alpha,m} > x^{\alpha,int}$, i.e. for a positive growth rate (considering precipitation of a solute-rich β phase, $kx^{\beta,int} - x^{\alpha,int}$ is generally positive), the particle is stable and grows; for $x^{\alpha,m} < x^{\alpha,int}$, the particle is unstable and shrinks. $x^{\alpha,int}$ and $x^{\beta,int}$ are often taken according to local establishment of thermodynamic equilibrium at the interface. For a small particle size, i.e. for a large ratio of interface area to particle volume, the state of equilibrium between the α -phase matrix and the β -phase precipitate can strongly deviate from the state of equilibrium between the α - and β -bulk phases, i.e. the α phase and the β phase in absence of the interface. This is the so-called Gibbs-Thomson effect, which, in compliance with the two counteracting contributions of composition-dependent chemical Gibbs energy and interface energy, can be expressed by functions $x^{\alpha,int}$ and $x^{\beta,int}$ depending on particle size (i.e. interface area) and interface energy γ per unit area, i.e. $x^{\alpha,int} = x^{\alpha,int}(r, \gamma)$ and $x^{\beta,int} = x^{\beta,int}(r, \gamma)$.

Kinetic modelling of nucleation and growth thus requires evaluation of the thermodynamics of the system defined by chemical energy and interface energy. Usually, the interface energy γ per area is taken as being constant within a certain range of composition, particle size and morphology. This assumption effectively allows to reduce the evaluation of the thermodynamics for the kinetic modelling to determination of (i) the nucleation barrier as function of the composition-dependent chemical driving force for nucleation $-\Delta g_c(x^{\alpha,m}, x^{\beta,p})$ and (ii) the compositions $x^{\alpha,int}(r)$ and $x^{\beta,int}(r)$ as function of particle size r (cf. Section 5.2). Analytical expressions for $\Delta g_c(x^{\alpha,m}, x^{\beta,p})$, $x^{\alpha,int}(r)$ and $x^{\beta,int}(r)$, based on simple thermodynamic solution models for the chemical Gibbs energies of the α and the β phase, are an often used, nu-

²for multinary systems, see e.g. [100]

³For binary systems, the convention $x^j = x_B^j$ will be used.

merically efficient way to implement thermodynamic data into the numerical kinetic modelling. For instance, the Gibbs-Thomson effect in a binary system is often accounted for by application of the equation [101]

$$x^{\alpha,\text{int}}(r) = x^\alpha(r \rightarrow \infty) \exp\left(\frac{2\gamma V_{\text{mol}}^\beta}{RT} \frac{1}{r}\right) \quad (5.3)$$

for the composition of the matrix at the particle-matrix interface, where $x^\alpha(r \rightarrow \infty)$ is the solute concentration of the α phase in the reference state of equilibrium between the α phase and the β phase with $r \rightarrow \infty$, i.e. between the bulk phases in absence of the interface. V_{mol}^β is the mean molar volume of the β -phase and R denotes the gas constant. Equation (5.3) is based on the assumption that the thermodynamic behaviour of the α -matrix phase can be described with the regular solution model and that the β -precipitate phase is a pure phase, i.e. $x^{\beta,\text{int}}(r) = x^\beta(r \rightarrow \infty) = 1$. The applicability of such analytical expressions can thus be severely limited by the limited capability of the underlying simple solution models to adequately describe the actual thermodynamic behaviour of the α phase and the β phase.

Hence, in recent years, direct numerical derivation of the relations $\Delta g_c(x^{\alpha,\text{m}}, x^{\beta,\text{p}})$, $x^{\alpha,\text{int}}(r)$ and $x^{\beta,\text{int}}(r)$ from a comprehensive thermodynamic assessment of the alloy system (which is typically based on more complex solid solution models for the chemical Gibbs energies) has been applied, especially for multi-component systems (see, e.g., [98,99]). This trend is facilitated by the increasing availability of such thermodynamic assessments, e.g. in form of CALPHAD data, and commercial software for thermodynamic analysis (e.g. [102]). On the one hand, the numerical determination of the chemical driving force for nucleation, $-\Delta g_c(x^{\alpha,\text{m}}, x^{\beta,\text{p}})$, for a given composition $x^{\alpha,\text{m}}$ of the matrix phase, can be performed straightforwardly, for instance by application of the parallel tangent/maximum chemical driving force approach [103] (see Section 5.2). On the other hand, the numerical evaluation of the Gibbs-Thomson effect, i.e. the determination of the compositions $x^{\alpha,\text{int}}(r)$ and $x^{\beta,\text{int}}(r)$, is much more elaborate [104–106], since it requires the evaluation of a thermodynamic equilibrium state including the energy contribution of the interface, e.g. by minimisation of the total Gibbs energy [102]. In view of the correspondingly larger complexity and computational effort, direct numerical evaluation of the Gibbs-Thomson effect has been avoided and simple analytical expressions such as Equation (5.3), based on generally invalid solid solution models, have been adopted instead. Obviously, problems of inconsistency arise when the relations $\Delta g_c(x^{\alpha,\text{m}}, x^{\beta,\text{p}})$ for nucleation and $x^{\alpha,\text{int}}(r)$ and $x^{\beta,\text{int}}(r)$ for growth are derived, analytically or numerically, by adoption

of differing, incompatible thermodynamic solution models for nucleation and for growth. This is a common shortcoming in kinetic models of precipitation kinetics based on the KWN-approach (e.g. [15, 96]).⁴ The problem becomes even more aggravated when an elastic strain energy contribution due to a precipitate/matrix misfit is taken into consideration only for nucleation but not for growth (or vice versa) without more ado (e.g. [108, 109]). As a consequence, the kinetic model predictions may be strongly biased or completely corrupted by the incongruent thermodynamic descriptions for nucleation and for growth.⁵

Against the above background, in the present work a generally valid approach of combined, inherently consistent, numerical evaluation of the thermodynamics of nucleation and growth is proposed which is founded on the Gibbsian treatment of nucleation and growth by fundamental consideration of thermodynamic equilibrium in a particle-matrix system [4, 110]: Starting from usually applied, typical approaches for separate thermodynamic evaluations of nucleation and growth, it is first shown how these approaches can be reconciled with a single evaluation of thermodynamic equilibrium. Introducing assumptions typically made upon coupling thermodynamics to kinetics (e.g. a constant interface energy per unit area), a powerful, computationally efficient method for numerical evaluations of nucleation barrier, critical radius and Gibbs-Thomson effect is presented, which can be easily adapted to practical cases of modelling transformation kinetics.

5.2 Theoretical background

Evaluation of nucleation thermodynamics, i.e. determination of the nucleation barrier ΔG^* and the critical radius r^* , classically departs from a consideration of the change of Gibbs energy $\Delta G(r)$ of the system with size of the precipitate particle formed, i.e. in case of formation of a spherical particle with radius r

$$\Delta G(r) = \frac{4}{3}\pi r^3 \times \Phi + 4\pi r^2 \times \gamma, \quad (5.4)$$

⁴Naturally, this problem does not appear in kinetic models without discrimination of nucleation kinetics and growth kinetics, as in cluster dynamics models, cf. e.g. [9]. Also, in kinetic models involving a consideration of the total (Gibbs) energy of the system [107], such problems are more readily avoided.

⁵Such type of inconsistencies can in an extreme case lead to the unphysical scenario that a particle of certain size generated by nucleation immediately experiences a negative growth rate due to $(x^{\alpha,m} - x^{\alpha,int}) < 0$ (cf. Equation (5.2)), i.e. it would be instantaneously, intrinsically unstable.

adopting the sharp interface model (see footnote in Section 5.1) with a constant (i.e. independent of r and composition), isotropic interface energy γ per unit area. Φ denotes the contributions to the Gibbs energy change which scale with the volume of the particle. For precipitation in the solid state, two contributions to Φ (per unit volume of particle) are typically taken into consideration: the (negative) change in chemical Gibbs energy Δg_c upon formation of a particle and an additional (positive) contribution of strain energy Δg_{el} , arising due to elastic accommodation of the particle/matrix misfit (with $\Phi = \Delta g_c + \Delta g_{el} < 0$). Δg_c and Δg_{el} are usually treated as constants for a given matrix composition. The Gibbs energy change then shows a maximum for $d\Delta G(r)/dr = 0$ for r equal to the critical radius

$$r^* = -\frac{2\gamma}{\Phi} = -\frac{2\gamma}{\Delta g_c + \Delta g_{el}}, \quad (5.5)$$

and with the nucleation barrier

$$\Delta G^* = \Delta G(r^*) = \frac{4}{3}\pi r^{*2}\gamma = \frac{16}{3} \frac{\gamma^3}{(\Delta g_c + \Delta g_{el})^2}. \quad (5.6)$$

For evaluating the change Δg_c in chemical Gibbs energy upon particle formation, it is assumed that particle formation occurs within an infinitely large matrix phase (or that the particle is negligibly small), implying a constant matrix composition $x^{\alpha,m}$ (and thus constant Δg_c for certain composition $x^{\beta,p}$ of the particle). The change in chemical Gibbs energy per unit volume of the particle is defined as the difference $\Delta g_c = g_c^\beta - g_c^\alpha$ of the chemical Gibbs energy g_c^β – the chemical Gibbs energy of the particle-forming components in the β phase of composition $x^{\beta,p}$ – and g_c^α – the chemical Gibbs energy of the same components in the supersaturated α -phase matrix of composition $x^{\alpha,m}$ evaluated at the composition $x^{\beta,p}$ of the nucleus (see Figure 5.1, note that all data presented for the binary case in Figures 5.1 (b) and 5.3 pertain to the example given in Section 5.4).

Introducing the chemical potentials $\mu_{c,i}^j(x^j)$ for the components i in the (bulk) phase $j = \alpha, \beta$, the chemical Gibbs energy change per mol, $\Delta g_{c,mol} = g_{c,mol}^\beta - g_{c,mol}^\alpha$, can be expressed as

$$\begin{aligned} g_{c,mol}^\beta - g_{c,mol}^\alpha &= \Delta g_{c,mol}(x^{\alpha,m}, x^{\beta,p}) \\ &= \sum_i x_i^{\beta,p} \mu_{c,i}^\beta(x^{\beta,p}) - \sum_i x_i^{\beta,p} \mu_{c,i}^\alpha(x^{\alpha,m}). \end{aligned} \quad (5.7a)$$

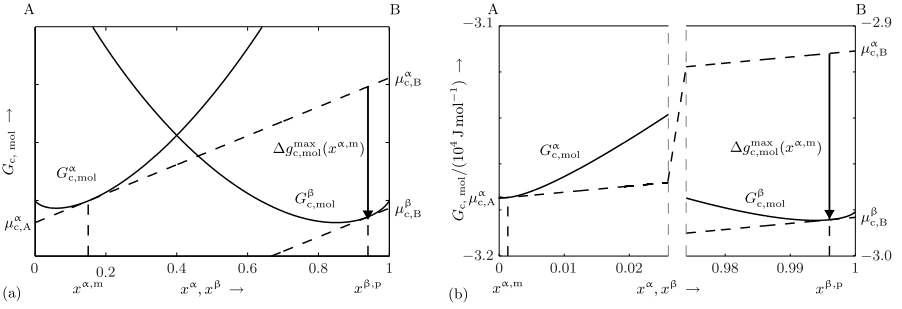


Figure 5.1: Chemical Gibbs energy curves $G_{c,\text{mol}}^\alpha(x^\alpha)$ and $G_{c,\text{mol}}^\beta(x^\beta)$ for the α phase (matrix) and the β phase (particle) in a binary system A-B as function of composition: (a) schematic representation; (b) chemical Gibbs energy curves for the system Cu-Co at $T = 763$ K and $p = 10^5$ Pa [29], employed for the case study in Section 5.4 (A: Cu, B: Co, α : fcc (Cu), β : fcc (Co)). The chemical driving force $-\Delta g_{c,\text{mol}}$ assumes a maximum value $-\Delta g_{c,\text{mol}}^{\text{max}}$ if the tangent on the $G_{c,\text{mol}}^\beta(x^\beta)$ -curve is parallel to the tangent of $G_{c,\text{mol}}^\alpha(x^\alpha)$ in $x^{\alpha,\text{m}}$, the given composition of the matrix (as shown here; parallel tangent/maximum driving force approach). This condition uniquely defines the composition $x^{\beta,\text{p}}$ of the β -phase particle.

For the case of nucleation, it thus follows with Equation (5.5):

$$\begin{aligned} \Delta g_{c,\text{mol}}(x^{\alpha,\text{m}}, x^{\beta,\text{p}}) &= \sum_i x_i^{\beta,\text{p}} \mu_{c,i}^\beta(x^{\beta,\text{p}}) - \sum_i x_i^{\beta,\text{p}} \mu_{c,i}^\alpha(x^{\alpha,\text{m}}) \\ &= - \left(\frac{2\gamma}{r^*} + \Delta g_{\text{el}} \right) V_{\text{mol}}^\beta \end{aligned} \quad (5.7b)$$

For a binary system, Equation (5.7b) can be visualised in a diagram of molar chemical Gibbs energy $G_{c,\text{mol}}^j(x^j)$ vs. composition x^j (see Figure 5.1). $\Delta g_{c,\text{mol}}(x^{\alpha,\text{m}}, x^{\beta,\text{p}})$ is represented by the difference of the ordinate value of the tangent of the $G_{c,\text{mol}}^\alpha(x^\alpha)$ -curve drawn at $x^{\alpha,\text{m}}$ (the given composition of the matrix phase) and evaluated at $x^{\beta,\text{p}}$ (the composition of the nucleus), and the $G_{c,\text{mol}}^\beta(x^\beta)$ -curve at $x^\beta = x^{\beta,\text{p}}$. For a given matrix composition $x^{\alpha,\text{m}}$, Equation (5.7b) does not uniquely define $\Delta g_{c,\text{mol}}(x^{\alpha,\text{m}}, x^{\beta,\text{p}})$ for nucleation, since the composition of the nucleus $x^{\beta,\text{p}}$ is not known a priori. In principle, for given $x^{\alpha,\text{m}}$, the composition $x^{\beta,\text{p}}$ of the precipitate nucleus may assume any value for which $\Delta g_{c,\text{mol}}(x^{\alpha,\text{m}}, x^{\beta,\text{p}})$ is negative. If $x^{\beta,\text{p}}$ is chosen such that the tangent of the $G_{c,\text{mol}}^\beta(x^\beta)$ -curve drawn at $x^{\beta,\text{p}}$ is parallel to the tangent of the $G_{c,\text{mol}}^\alpha(x^\alpha)$ -curve (fixed by the given matrix com-

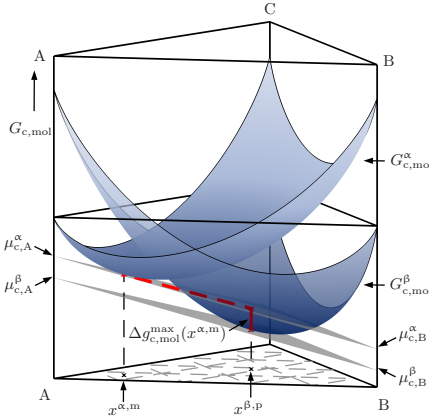


Figure 5.2: Chemical Gibbs energy surfaces $G_{c,\text{mol}}^\alpha(x)$ and $G_{c,\text{mol}}^\beta(x)$ for the α phase and the β phase in a ternary system A-B-C. Here, the parallel tangents of the binary system correspond to parallel tangent planes (depicted in grey). Applying the parallel tangent/maximum chemical driving force method yields $\Delta g_{c,\text{mol}}(x^{\beta,\text{p}}(x^{\alpha,\text{m}}))$ (vertical red line) and the composition $x^{\beta,\text{p}}(x^{\alpha,\text{m}})$ of the β -phase particle (for better visualisation, the $G_{c,\text{mol}}^\beta(x)$ -surface and the tangent planes were plotted semi-transparent).

position $x^{\alpha,\text{m}}$, the chemical driving force $-\Delta g_{c,\text{mol}}(x^{\alpha,\text{m}}, x^{\beta,\text{p}})$ assumes a maximum value and is solely defined by the composition of the matrix phase, i.e. $\max(-\Delta g_{c,\text{mol}}(x^{\alpha,\text{m}}, x^{\beta,\text{p}})) = -\Delta g_{c,\text{mol}}^{\text{max}}(x^{\alpha,\text{m}})$ and $x^{\beta,\text{p}} = x^{\beta,\text{p}}(x^{\alpha,\text{m}})$. This is the so-called maximum chemical driving force approach or parallel tangent approach [103, 111], an originally graphical method to determine the maximum chemical driving force for a binary system which can be straightforwardly generalised to the multinary case to numerically determine $-\Delta g_{c,\text{mol}}^{\text{max}}(x^{\alpha,\text{m}})$ and $x^{\beta,\text{p}} = x^{\beta,\text{p}}(x^{\alpha,\text{m}})$ (see Figure 5.2). Other methods for describing nucleation depart from setting $x^{\beta,\text{p}}$ equal to the composition of the β phase corresponding with equilibrium between the α - and β -bulk phases, thus inherently employing a lower chemical driving force; in the following, $x^{\beta,\text{p}}$ will always be identified with the composition of the β phase pertaining to the maximum chemical driving force). Use of the maximum chemical driving force is justified recognising the strong dependency of the nucleation rate \dot{N} on $\Delta g_{c,\text{mol}}(x^{\alpha,\text{m}}, x^{\beta,\text{p}})$ (Equations (5.1) and (5.6)), allowing to neglect nucleation of particles of composition different from that corresponding with the maximum chemical driving force [112].

Calculation of the growth rate requires evaluation of the Gibbs-Thomson effect, i.e. determination of the compositions $x^{\alpha,\text{int}}(r)$ and $x^{\beta,\text{int}}(r)$ as function

of particle size (cf. Equation (5.2)). This involves analysis of the equilibrium state for the β -phase particle embedded in the α -phase matrix, accounting for the contributions of the chemical energies, of the interface energy and of the elastic misfit-strain energy. Thermodynamic equilibrium, here at constant p and T , corresponds to equality of the (total⁶) chemical potentials μ_i^j for each component i in all phases of the system j , i.e.

$$\mu_i^{\alpha,m} = \mu_i^{\beta,p}. \quad (5.8)$$

Elaboration of these equilibrium conditions for the system particle-matrix in terms of size and shape of the second-phase particle, composition (field), elastic strain (field) etc. can become extremely cumbersome due to the interdependence of these parameters. Therefore, without restricting the generality of the following discussion, several simplifying assumptions and boundary conditions are introduced here:

- (i) the matrix phase is taken infinitely large,
- (ii) particle and matrix are separated by a sharp interface (see above), with a size- and composition-independent, isotropic interface energy per unit area γ ,
- (iii) the elastic misfit-strain energy Δg_{el} per unit volume can be reasonably well described by assumption of phases of constant compositions and of isotropic elasticity; the presence of the interface has no effect on the state of stress (i.e. the effect of interface *stress* is neglected, cf. [114,115,110]),
- (iv) the particle is of spherical shape (a consequence of the elastic isotropy and the isotropy of γ ; see (ii) and (iii) above),
- (vi) the molar volume of the precipitate phase is independent of composition (i.e. the partial molar volumes $V_{\text{mol},i}^{\beta}$ of the components of the β phase have the same value).

These assumptions, all more or less implicitly already introduced in the above discussion on the thermodynamics of nucleation, allow expression of the equilibrium condition in terms of phase composition and particle size on the basis of equality of the total chemical potential of the components,

$$\mu_i^{\alpha,m}(x^{\alpha,m}, x^{\beta,p}, r) = \mu_i^{\beta,p}(x^{\alpha,m}, x^{\beta,p}, r), \quad (5.9)$$

⁶derived from the total energy function, i.e. in the present case the total Gibbs energy incorporating the contributions of chemical Gibbs energy, interface energy and elastic energy, see e.g. [113],

and also allow a separation of the contributions of interface energy, elastic energy and chemical energy to the (total) chemical potential (cf. e.g. [111]), the latter then being the only contribution depending on (variable) phase composition:

$$\mu_{c,i}^{\alpha}(x^{\alpha,m}) = \mu_{c,i}^{\beta}(x^{\beta,p}) + \left(\frac{2\gamma}{r} + \Delta g_{el} \right) V_{mol,i}^{\beta}, \quad (5.10)$$

with $\mu_{c,i}^j(x^j)$ as the chemical potential of component i in the bulk phase j in the unstressed state, i.e. the chemical potential pertaining to the composition-dependent chemical Gibbs energy only (cf. Equation (5.7)).⁷

Equation (5.10) represents a system of equations (one equation for each component i) which defines thermodynamic equilibrium for the system particle-matrix. For given values of the interface energy γ , the elastic strain energy Δg_{el} and the partial molar volume $V_{mol,i}^{\beta}$, Equation (5.10) allows to derive expressions for the compositions $x^{\alpha,m}(r) = x^{\alpha,int}(r)$ and $x^{\beta,p}(r) = x^{\beta,int}(r)$ as function of particle radius r employing suitable functions for the chemical potentials $\mu_{c,i}^j(x^j)$ (i.e. employing suitable thermodynamic solution models $G_{c,mol}^{\alpha}(x^{\alpha})$ and $G_{c,mol}^{\beta}(x^{\beta})$ for the α and β phase).

In case of binary systems A-B, closed, analytical expressions for $x^{\alpha,int}(r)$ and $x^{\beta,int}(r)$ can be obtained if very simple mathematical expressions hold for the chemical potentials $\mu_{c,i}^j(x^j)$, i.e. if very simple solid solution models are applicable (cf. Equation (5.3)). For example, adopting the ideal solution model for the α phase and assuming a pure β phase of the solute component B, the chemical potential $\mu_{c,B}^j(x^j)$ is given by $\mu_{c,B}^{\alpha}(x^{\alpha}) = \mu_{c,B}^{\alpha,0} + RT \ln(x^{\alpha})$, and $\mu_{c,B}^{\beta}(x^{\beta}) = \mu_{c,B}^{\beta,0}$, since $x^{\beta} = x^{\beta,p} = 1$ (the corresponding chemical potential $\mu_{c,A}^{\beta}$ of component A in the β phase is not defined). Then, $\mu_{c,B}^{\alpha,0} + RT \ln(x^{\alpha}(r \rightarrow \infty)) = \mu_{c,B}^{\beta,0}$ holds for equilibrium between the bulk phases, i.e. in absence of interface and misfit strain. Applying Equation (5.10) for the equilibrium between the α -phase matrix and the β -phase precipitate in this case then leads to a Gibbs-Thomson-type equation

$$x^{\alpha,m}(r) = x^{\alpha,int}(r) = x^{\alpha}(r \rightarrow \infty) \exp \left(\left(\frac{2\gamma}{r} + \Delta g_{el} \right) \frac{V_{mol,B}^{\beta}}{RT} \right). \quad (5.11)$$

As compared to Equation (5.3), this expression includes an additional cor-

⁷For $r \rightarrow \infty$, the elastic energy contribution, in contrast with the interface energy contribution, does not vanish, since both the chemical Gibbs energy and the elastic energy contribution scale with the volume of the particle.

rection for the elastic energy contribution. Similar analytical expressions for $x^{\alpha,\text{int}}(r)$ and $x^{\beta,\text{int}}(r)$, based on other (simplifying) assumptions, can be found in numerous works (see e.g. [116,97] for the case of $\Delta g_{\text{el}} = 0$, and [115] including a consideration of elastic misfit-strain and interface stress for the special case of ideal solid solutions).

For describing the Gibbs-Thomson effect in the general case, i.e. without resorting to specific simple solution models for the α and β phase and without restriction to binary systems, Equation (5.10) has in principle to be evaluated numerically to obtain the (numerical) relationships $x^{\alpha,\text{int}}(r)$ and $x^{\beta,\text{int}}(r)$ (see e.g. [104, 105] or [106]).

Now considering the thermodynamics of both nucleation and growth, as in case of kinetic modelling, separate analysis of nucleation thermodynamics (Equation (5.7b)) and of growth thermodynamics (the Gibbs-Thomson effect, Equation (5.10)) is unnecessary: both nucleation and growth thermodynamics are based on the same thermodynamic stability consideration. In case of nucleation, the critical *size* $r^* = r(\Delta g_{\text{c,mol}}(x^{\alpha,\text{m}}, x^{\beta,\text{P}}(x^{\alpha,\text{m}})), \gamma, \Delta g_{\text{el}})$ for stability of a nucleus is determined, which, for given γ and Δg_{el} , is defined by a difference in chemical Gibbs energy (Equation (5.7b)) and thus by the *compositions* $x^{\alpha,\text{m}}$ and $x^{\beta,\text{P}} = x^{\beta,\text{P}}(x^{\alpha,\text{m}})$ of the α -matrix phase and the β -precipitate phase, respectively. In case of growth, the *compositions* $x^{\alpha,\text{int}}(r, \gamma) = x^{\alpha,\text{m}}(r, \gamma)$ of the α -phase matrix and $x^{\beta,\text{int}}(r, \gamma) = x^{\beta,\text{P}}(r, \gamma)$ of the β -phase precipitate particle, as defined by a difference in chemical Gibbs energy (c.f. Equation (5.10)), are evaluated for a particle of certain *size* r stable in an α -phase matrix. Thermodynamic analysis in both cases thus breaks down to an evaluation of the equilibrium state for an α -phase matrix of certain composition containing a β -phase particle of certain composition and certain size r , associated with a certain interface energy and elastic strain energy. As such, this is a consideration of thermodynamic equilibrium in a heterogeneous system with counteracting contributions to the total energy scaling differently with size of the second-phase domain (see [4], p. 252 ff., for a discussion of particle formation/nucleation and stability in a one-component system ensuing from a consideration of thermodynamic equilibrium, there in terms of the variables *size* and *pressure*).

The equivalence of the nucleation and growth thermodynamics as presented above may be elucidated in the following way: From Equations (5.9) and (5.10), the total molar Gibbs energy $g_{\text{mol}}^{\beta,\text{P}} = \sum_i \mu_i^{\beta,\text{P}}(x^{\beta,\text{P}}, r) x_i^{\beta,\text{P}}$ of a precipitate particle with radius r and composition $x^{\beta,\text{P}}$ is given by (cf. Equation (5.9))

$$\sum_i \mu_i^{\beta,\text{P}}(x^{\beta,\text{P}}, r) x_i^{\beta,\text{P}} = \sum_i \mu_i^{\alpha,\text{m}}(x^{\alpha,\text{m}}, r) x_i^{\beta,\text{P}} \quad (5.12)$$

and (cf. Equation (5.10))

$$\sum_i \left[\mu_{c,i}^\beta(x^{\beta,P}) + \left(\frac{2\gamma}{r} + \Delta g_{el} \right) V_{mol,i}^\beta \right] x_i^{\beta,P} = \sum_i \mu_{c,i}^\alpha(x^{\alpha,m}) x_i^{\beta,P} \quad (5.13a)$$

$$\left[\sum_i \mu_{c,i}^\beta(x^{\beta,P}) x_i^{\beta,P} \right] + \left(\frac{2\gamma}{r} + \Delta g_{el} \right) V_{mol}^\beta = \sum_i \mu_{c,i}^\alpha(x^{\alpha,m}) x_i^{\beta,P}, \quad (5.13b)$$

with $\sum_i V_{mol,i}^\beta x_i^{\beta,P} = V_{mol}^\beta$ and $\sum_i x_i^{\beta,P} = 1$. In a diagram of molar *chemical* Gibbs energies vs. composition of a binary system, Equation (5.13b), under the constraint of satisfying Equation (5.10)⁸ for each component i , represents a construction of two parallel tangents, one of the $G_{c,mol}^\alpha(x^\alpha)$ -curve and one of the $G_{c,mol}^\beta(x^\beta)$ -curve, with a vertical offset of $\left(\frac{2\gamma}{r} + \Delta g_{el} \right) V_{mol}^\beta$, since this additional term to each $\mu_{c,i}^\beta$ is independent of composition. Equation (5.13b), under the constraint of satisfying Equation (5.10) for each component, thus is identical with Equation (5.7) derived specifically for nucleation, provided the latter is evaluated according to the parallel tangent/maximum chemical driving force approach (see discussion below Equation (5.7)). Hence, evaluation of nucleation thermodynamics by combination of Equation (5.7) with the maximum chemical driving force approach represents an evaluation of the thermodynamic equilibrium of the system particle-matrix as function of the variables $x^{\alpha,m}$, $x^{\beta,P}$ and r and thus comprises both nucleation thermodynamics *and* growth thermodynamics.⁹ Irrespective of the simplifying assumptions introduced above, this equivalence generally holds as long as nucleation is treated as occurring via a critical state for which the particle is in an unstable equilibrium with the matrix and growth is treated as involving local establishment of thermodynamic equilibrium at the particle-matrix interface (cf. Section 5.1). Separate evaluation of nucleation thermodynamics and growth thermodynamics is then generally unnecessary, as will be illustrated in the next section.

Despite the fundamental nature of the equivalence of nucleation thermodynamics and growth thermodynamics [4], it has frequently been disregarded for analysis of the thermodynamics of nucleation and growth with respect to

⁸Equation (5.13b) is only a necessary condition, while Equation (5.10) is a sufficient condition.

⁹Equation (5.7) results from a *maximisation* of the system energy change as function of the radius r . Combined with a *maximisation* of the chemical driving force as function of the composition x^β at given $x^{\alpha,m}$, this corresponds, under the present assumptions, to the determination of equilibrium as function of r and x^β (the function $\Delta G(r, \Delta g_{c,mol}(x^\alpha = x^{\alpha,m}, x^\beta))$ shows a saddle-point at $r = r^*$, $x^\beta = x^{\beta,P}$). Indeed, the maximum chemical driving force/parallel tangent method is derived from a consideration of thermodynamic equilibrium [103].

kinetic modelling (but, cf. e.g., [114,115,103,111,97]) – a possible reason may lie in typical textbook treatments of nucleation thermodynamics in terms of an energy change (cf. Equation (5.4)), and of growth in terms of compositions only (instead of, e.g., activities; cf. Equation (5.2)) [101]. Moreover, its implications for thermodynamic evaluation upon kinetic modelling based on a modelling approach as outlined in Section 5.1 have, to the authors’ knowledge, up to now not been utilised at all.

5.3 Usage of the common stability consideration upon numerical evaluation of nucleation and growth thermodynamics

Modelling of nucleation and growth kinetics requires numerous evaluations of the corresponding thermodynamic relations, i.e. nucleation barrier and Gibbs-Thomson effect (cf. Section 5.1). In this situation, the equivalence of nucleation thermodynamics and growth thermodynamics as presented in the previous section allows, for the typically made assumption of a constant interface energy γ and a constant elastic energy contribution Δg_{el} , to devise a convenient method for computationally efficient analysis of thermodynamic data.

For nucleation, numerical evaluation of the chemical driving force can be performed straightforwardly by application of the maximum chemical driving force approach: For given matrix composition $x^{\alpha,\text{m}}$, $\Delta g_{\text{c,mol}}^{\text{max}}(x^{\alpha,\text{m}})$ can be directly evaluated from the chemical Gibbs energy functions $G_{\text{c,mol}}^{\alpha}(x)$ and $G_{\text{c,mol}}^{\beta}(x)$, for example by first calculating the tangent (plane) T^{α} of $G_{\text{c,mol}}^{\alpha}(x)$ in $x^{\alpha,\text{m}}$, i.e. $T^{\alpha}(x^{\alpha,\text{m}}, x) = \sum_i x_i \mu_{\text{c},i}^{\alpha}(x^{\alpha,\text{m}})$, and then finding the maximum of $\left| G_{\text{c,mol}}^{\beta}(x) - T^{\alpha}(x, x^{\alpha,\text{m}}) \right| = -\Delta g_{\text{c,mol}}^{\text{max}}(x^{\alpha,\text{m}})$ and the corresponding composition $x = x^{\beta,\text{p}}(x^{\alpha,\text{m}})$ of the β -phase particle (Figures 5.3 (a,b) and 5.4). Upon kinetic modelling, for given values of γ and Δg_{el} , the critical radius $r^* = r(\Delta g_{\text{c,mol}}^{\text{max}}(x^{\alpha,\text{m}}), \gamma, \Delta g_{\text{el}}) = r(x^{\alpha,\text{m}}, \gamma, \Delta g_{\text{el}})$ can be computed using Equation (5.5) (see Figures 5.3 (c) and 5.5). During the actual computation process, the numerical relation $r^* = r(x^{\alpha,\text{m}}, \gamma, \Delta g_{\text{el}})$ can then be accessed rapidly for certain $x^{\alpha,\text{m}}$, e.g. via a table look-up.

For growth, the equilibrium of the particle-matrix system (i.e. the Gibbs-Thomson effect) has to be evaluated [104–106] for given values of radius r , interface energy γ and elastic energy Δg_{el} based on Equation (5.10) (see Section 5.2; or on Equation (5.13), see e.g. [105], the additionally required constraint (see below Equation (5.13)) can then e.g. be obtained by introduction of the Gibbs-Duhem equation). Now, instead of either (numerically) evaluating Equation (5.10) (see, e.g., [104–106]) or adopting some approximate descrip-

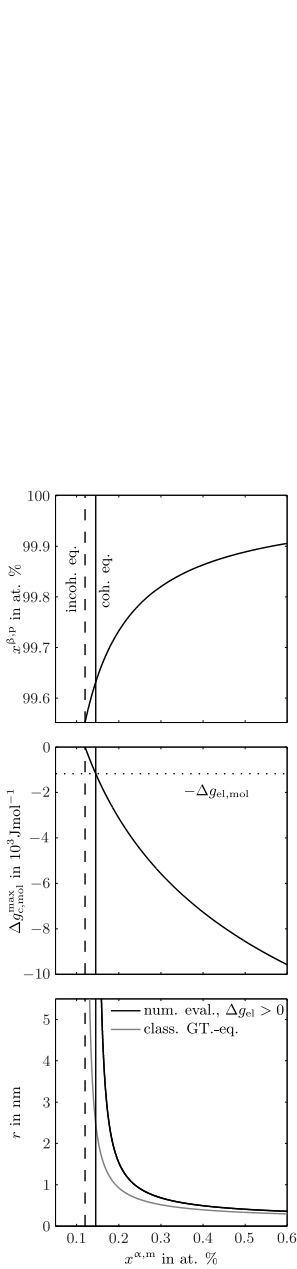


Figure 5.3: (a) Composition $x^{\beta,p}(x^{\alpha,m})$ of the β -phase particle and (b) maximum change in molar chemical Gibbs energy $\Delta g_{c,mol}^{\max}(x^{\alpha,m})$, both as function of the α -matrix composition $x^{\alpha,m}$, as derived from the chemical Gibbs energy curves of the α and β phases (see Figure 5.1 (b)) by application of the maximum chemical driving force method. The contribution of the elastic energy is represented by the dotted line in (b). For $\Delta g_{c,mol}^{\max}(x^{\alpha,m}) = 0$, i.e. zero chemical driving force, $x^{\alpha,m}$ and $x^{\beta,p}$ assume the composition values for equilibrium between bulk phases in absence of interface energy and elastic energy (indicated by the dashed vertical lines in (a), (b) and (c)). For $\Delta g_{c,mol}(x^{\alpha,m}) + \Delta g_{el} = 0$, $x^{\alpha,m}$ and $x^{\beta,p}$ assume the values for so-called coherent equilibrium of the bulk phases (indicated by the solid vertical lines in (a), (b) and (c)). (c) The relation $r(\Delta g_{c,mol}^{\max}(x^{\alpha,m}), \gamma, \Delta g_{el})$ as function of the matrix composition $x^{\alpha,m}$ (black curve), calculated by use of Equation (5.5) (for γ and Δg_{el} see Section 5.4). For nucleation, this relation can be evaluated for given matrix composition $x^{\alpha,m}$ in order to obtain the critical radius $r^* = r(\Delta g_{c,mol}^{\max}(x^{\alpha,m}), \gamma, \Delta g_{el})$. For growth, the same relation can be evaluated inversely for given radius r of the precipitate-phase particle in order to obtain the corresponding equilibrium composition of the matrix $x^{\alpha,int} = x^{\alpha,m}(r)$ as function of the particle radius. The composition $x^{\beta,int} = x^{\beta,p}(r)$ of the β phase can then be derived via the relation $x^{\beta,p}(x^{\alpha,m})$ shown in (a). The grey curve in (c) represents the relation $x^{\alpha,int}(r)$ as derived from the classical Gibbs-Thomson equation (5.3), i.e. neglecting the elastic energy contribution Δg_{el} and using a highly simplified thermodynamic solution model (note that when using the classical Gibbs-Thomson equation, $x^{\beta,p} = 1$ is assumed). For $r \rightarrow \infty$, the composition of the matrix in the first case (exact treatment) approaches the composition for coherent equilibrium (i.e. the solid vertical line), in the second case (the approximate Gibbs-Thomson equation) the composition for incoherent equilibrium (i.e. the dashed vertical line). All numerical results shown in this figure pertain to the example case considered in detail in Section 5.4.

tion of the Gibbs-Thomson effect (as Equation (5.11); see, e.g.[15, 96, 109]), the equivalence of evaluating the thermodynamics of nucleation and of the treatment of thermodynamic equilibrium of the particle-matrix system can be utilised: values for the matrix composition $x^{\alpha,\text{int}} = x^{\alpha,\text{m}}(r, \gamma, \Delta g_{\text{el}})$ as function of the radius can simply be obtained by inverse evaluation of the relation $r^* = r(x^{\alpha,\text{m}}, \gamma, \Delta g_{\text{el}})$, determined for nucleation, e.g. via an inverse table look-up. The corresponding composition $x^{\beta,\text{int}}$ of the precipitate phase can then be derived from the relation $x^{\beta,\text{P}}(x^{\alpha,\text{m}})$ (see Figures 5.3 (a), (c) and 5.5). With the thermodynamic relations for nucleation and for growth thus based on the same thermodynamic analysis, any inconsistencies of the thermodynamic descriptions are inherently excluded.¹⁰

In binary systems, for a given radius r , the inverse evaluation method provides a unique set of compositions $x^{\alpha,\text{int}} = x^{\alpha,\text{m}}(r, \gamma, \Delta g_{\text{el}})$ and $x^{\beta,\text{int}} = x^{\beta,\text{P}}(r, \gamma, \Delta g_{\text{el}}) = x^{\beta,\text{P}}(x^{\alpha,\text{m}})$ (this corresponds to the existence of a single tie-line at given p and T relating one pair of compositions $(x^{\alpha,\text{m}}, x^{\beta,\text{P}})$, analogous to equilibrium between bulk phases in a binary system, cf. Figure 5.3). Starting from a composition $x^{\beta,\text{P}}(x^{\alpha,\text{m}}) = x^{\beta,\text{int}}$ of the particle defined by the composition of the matrix $x^{\alpha,\text{m}} = x^{\alpha,\text{int}}$ at the moment of its nucleation, the compositions $x^{\alpha,\text{int}}$ and $x^{\beta,\text{int}}$ then evolve upon particle growth (see, e.g., Equation (5.2)) according to $x^{\alpha,\text{int}} = x^{\alpha,\text{m}}(r, \gamma, \Delta g_{\text{el}})$ and $x^{\beta,\text{int}} = x^{\beta,\text{P}}(r, \gamma, \Delta g_{\text{el}})$.

In a multinary system, however, equilibrium is not uniquely defined by the value of the particle radius r (the system of equations (5.10) would then be an underdetermined system), i.e. the composition of the phases cannot be determined directly via the inverse evaluation method (this corresponds to the existence of multiple tie-lines at given p and T relating multiple pairs of compositions $(x^{\alpha,\text{m}}, x^{\beta,\text{P}})$, analogous to phase equilibrium between bulk phases in a multinary system; cf. Figures 5.4 and 5.5). Starting from the, also for the multinary case, known compositions $x^{\alpha,\text{int}} = x^{\alpha,\text{m}}(r, \gamma, \Delta g_{\text{el}})$ and $x^{\beta,\text{int}} = x^{\beta,\text{P}}(r, \gamma, \Delta g_{\text{el}}) = x^{\beta,\text{P}}(x^{\alpha,\text{m}})$ of matrix and particle at the moment of nucleation, upon particle growth the generally differing diffusivities of the components in the matrix can then lead to a continuous change of the compositions in addition to the size effect. Modelling of the growth kinetics in a multi-component system considering the Gibbs-Thomson effect therefore requires knowledge of the coupled evolutions of particle radius and of phase

¹⁰The critical radius and the so-called no-growth radius r^c , the radius for which $x^{\alpha,\text{int}}(r)$ equals the current composition $x^{\alpha,\text{m}}$ of the matrix and the growth rate (Equation (5.2)) then equals zero, are then inherently identical (compare e.g. [108]). Arguably, the thermodynamics of nucleation and of growth may be different: For example, after nucleation of a particle, the misfit strain generated by the particle can be relaxed in the further course of its growth, e.g. via vacancy condensation or introduction of misfit dislocations. The kinetics of such additional mechanisms should then be explicitly introduced into the kinetic model.

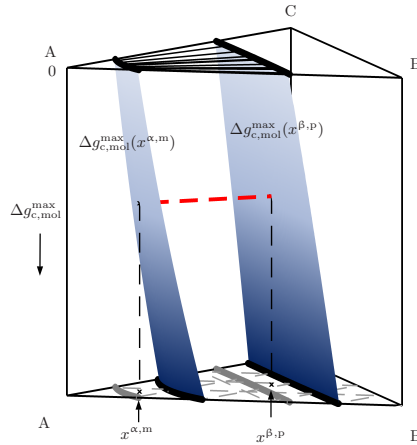


Figure 5.4: Maximum change in chemical Gibbs energy $\Delta g_{c,\text{mol}}^{\text{max}}(x^{\alpha,\text{m}})$ as function of the matrix concentration $x^{\alpha,\text{m}}$ for a ternary system A-B-C with phases α and β (a surface in this figure; cf. Figure 5.2). The corresponding composition relation $x^{\beta,\text{p}}(x^{\alpha,\text{m}})$ between the β -precipitate phase and the α -matrix phase is here represented as a plot of the surface $\Delta g_{c,\text{mol}}^{\text{max}}(x^{\beta,\text{p}}(x^{\alpha,\text{m}}))$. Each composition pair $(x^{\beta,\text{p}}, x^{\alpha,\text{m}})$ is related by a tie-line (the dashed red line represents the tie-line for the case depicted in Figure 5.2). For $\Delta g_{c,\text{mol}}(x^{\alpha,\text{m}}) = 0$, i.e. zero chemical driving force, the ternary equilibrium between the α - and β -bulk phases is obtained (cf. Figure 5.3).

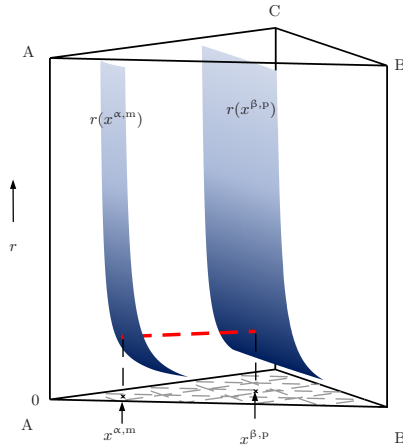


Figure 5.5: The relation $r(x^{\alpha,m}, \gamma, \Delta g_{el})$ as function of the matrix composition $x^{\alpha,m}$ in a ternary A-B-C system with phases α and β , calculated from the maximum change in chemical Gibbs energy $\Delta g_{c,mol}^{\max}(x^{\alpha,m})$ as shown in Figure 5.4 by use of Equation (5.5), with arbitrarily chosen values for γ and Δg_{el} (for $\Delta g_{el} = 0$, this figure corresponds to the so-called “Gibbs-Thomson phase diagram” as presented in [105]). The corresponding composition relation $x^{\beta,p}(x^{\alpha,m})$ is represented by a plot of the surface $r(x^{\beta,p}(x^{\alpha,m}), \gamma, \Delta g_{el})$. Corresponding relations pertaining to different values of γ and Δg_{el} can be easily re-obtained from the $\Delta g_{c,mol}^{\max}(x^{\alpha,m})$ -data via Equation (5.5). When considering nucleation, the critical radius $r^* = r(x^{\alpha,m}, \gamma, \Delta g_{el})$ and the composition of the nucleus $x^{\beta,p}(x^{\alpha,m})$ can directly be obtained from $r(x^{\alpha,m}, \gamma, \Delta g_{el})$, equivalent to the binary case (cf. Figure 5.3). In case of growth, direct inverse evaluation of $r(x^{\alpha,m}, \gamma, \Delta g_{el})$ in order to determine $x^{\alpha,int}(r)$ and $x^{\beta,int}(r)$ is not possible (in contrast with the binary case, Figure 5.3 (c)): For a given value of r , an infinite number of composition pairs $(x^{\beta,p}, x^{\alpha,m})$ exists (equivalent to equilibrium between bulk phases, i.e. for $r \rightarrow \infty$ and $\Delta g_{el} = 0$). For modelling of particle growth in a multi-component system under assumption of equilibrium at the particle-matrix interface, particle radius and as well as compositions must therefore be tracked. Size and compositions then follow coupled trajectories on the $r(x^{\alpha,m}, \gamma, \Delta g_{el})$ - and $r(x^{\beta,p}(x^{\alpha,m}), \gamma, \Delta g_{el})$ -surfaces defined by the diffusion kinetics of the different components in the matrix phase.

compositions under the equilibrium constraint provided by Equation (5.10) (see e.g. [100]). This constraint corresponds to subjecting the size-composition trajectory of the particle to the relations $r(x^{\alpha,\text{m}}, \gamma, \Delta g_{\text{el}})$ and $x^{\beta,\text{p}}(x^{\alpha,\text{m}})$ obtained via the inverse evaluation method (Figure 5.5): particle size and the compositions at the interface then follow a path, governed by the growth kinetics of the multi-component system [100], on the size-composition surfaces determined by thermodynamics (the $r(x^{\alpha,\text{m}})$ - and $r(x^{\beta,\text{p}})$ -surfaces in Figure 5.5; cf. [98, 99]).

The equivalence of nucleation and growth thermodynamics in principle also allows application of a reverse procedure to obtain the thermodynamic relations between particle size and phase compositions: In a first step, the evaluation of the growth thermodynamics via Equation (5.10) could be performed for chosen values of r to determine $x^{\alpha,\text{int}} = x^{\alpha,\text{m}}(r, \gamma, \Delta g_{\text{el}})$ and $x^{\beta,\text{int}} = x^{\beta,\text{p}}(r, \gamma, \Delta g_{\text{el}})$, for given interface energy γ and elastic energy contribution Δg_{el} . Then, in a second step, the corresponding relation $r^* = r(x^{\alpha,\text{m}}, \gamma, \Delta g_{\text{el}})$, required for description of the nucleation kinetics, could be obtained by inverse evaluation. However, upon assumption of constant γ and Δg_{el} , determination of the thermodynamic relations as presented above is much more convenient than this reverse procedure: Evaluation of the thermodynamics of growth as a first step would require a complete evaluation of thermodynamic equilibrium via Equation (5.10) for each value of γ , Δg_{el} and r [104–106]. The approach via nucleation thermodynamics, by contrast, allows to split the thermodynamic evaluation into two independent steps: Once the chemical driving force for nucleation $-\Delta g_{\text{c,mol}}^{\text{max}}(x^{\alpha,\text{m}})$ and the relation $x^{\beta,\text{p}}(x^{\alpha,\text{m}})$ have been derived from the thermodynamic assessment of the system (determination of critical, equilibrium phase compositions), the numerically simple Equation (5.5) can be easily (re-)evaluated for given values of γ and Δg_{el} to obtain the numerical relation $r(x^{\alpha,\text{m}}, \gamma, \Delta g_{\text{el}})$ pertaining to these values (determination of critical, equilibrium particle size). The method proposed in this paper, with evaluation of the nucleation thermodynamics as a first step, thus represents a potent and numerically efficient way of handling the numerical thermodynamic data and allows for instance to use the interface energy γ as a fit parameter in a computational algorithm (see [117]) or to efficiently incorporate a size dependency of the interface energy¹¹ $\gamma = \gamma(r)$.

The proposed treatment builds on the separability of the chemical Gibbs energy contribution, the interface energy contribution and elastic energy contribution (Equation (5.9) \rightarrow Equation (5.10)), which allows application of the maximum chemical driving force method to independently determine the

¹¹Note that in this case, Equation (5.5) (and, correspondingly, also Equation (5.10)) does not hold in the usual form as given in Section 5.2; it must be derived from Equation (5.4) with $\gamma = \gamma(r)$.

chemical contribution. Accordingly, the presented approach breaks down as soon as interface energy and elastic energy (and the molar volume of the precipitate phase) show a composition dependency which cannot be neglected, thus prohibiting application of the maximum chemical driving force method [103]. Analysis of the thermodynamics of nucleation and growth would then require determination of equilibrium on the basis of a more general consideration of the total energy (cf. Equation 5.8). However, the fundamental equivalence of the thermodynamics of nucleation and of growth, as two aspects of the same fundamental thermodynamic equilibrium principle, still remains intact and allows inverse evaluation of the thermodynamic relations, thus avoiding inconsistent, unnecessarily separate thermodynamic evaluations of nucleation and growth.

5.4 Example

To visualise the usage of the inverse evaluation method upon modelling the kinetics of precipitation reactions, thus avoiding inconsistent thermodynamic descriptions for nucleation and growth, the precipitation kinetics were simulated for a binary A-B model system (using for the kinetics a KWN-type approach as frequently employed for practical applications; for details on the kinetic modelling, see [117]).

The properties of the A-B system were chosen to mimic the system Cu-Co, a classical model system for precipitation reactions (see e.g. [8,35,39]): Upon annealing of supersaturated Cu-rich alloys, spherical Co-rich precipitate particles of fcc structure are formed which are (initially) fully coherent with the fcc Cu-rich matrix phase. Thermodynamic data was taken from a recent CALPHAD assessment of the system Cu-Co [29] at $T = 763$ K (and $p = 10^5$ Pa): From the chemical Gibbs energy curves (Figure 5.1 (b)), employing the maximum chemical driving force method, $-\Delta g_{c,mol}^{max}(x^{\alpha,m})$ and the precipitate particle composition $x^{\beta,p}(x^{\alpha,m})$ were derived as function of the matrix composition $x^{\alpha,m}$ (Figure 5.3). Due to the small lattice misfit between fcc Cu and fcc Co [118], the elastic energy contribution Δg_{el} is relatively small (but not negligible, cf. [42]): At the chosen alloy composition of Cu 0.5 at.% Co, Δg_{el} (here calculated using Eshelby's model [119]) amounts to about 14 % of the initial maximum chemical driving force. Further parameters employed for kinetic modelling are given in Table 5.1.

The precipitation kinetics were simulated for two different scenarios: (i) Consistent scenario: use of the relation $r(x^{\alpha,m}, \gamma, \Delta g_{el})$ as determined via Equation (5.5) from the maximum chemical driving force $-\Delta g_{c,mol}^{max}(x^{\alpha,m})$ (Figure 5.3 (b),(c)) and of the relation $x^{\beta,p}(x^{\alpha,m})$ (Figure 5.3 (a)) for *both* nuc-

Table 5.1: Data employed for simulation of the precipitation kinetics in a binary model system A-B mimicking a Cu-0.5 at.% Co alloy at $T = 763$ K. γ : interfacial energy; Q , D_0 : activation energy for diffusion, corresponding pre-exponential factor (used for both nucleation and growth); V_{mol} : molar volume; E : Young's modulus (elastic isotropy approximation), G : shear modulus.

parameter	value	source, remark
γ	220 mJm^{-2}	(assessed)
Q	214 kJmol^{-1}	[73]
D_0	$4.3 \times 10^{-5} \text{ m}^2\text{s}^{-1}$	[73]
fcc Cu		
V_{mol}	$7.3 \times 10^{-6} \text{ m}^3\text{mol}^{-1}$	[118]
E	$18.1 \times 10^{10} \text{ Pa}$	[120], $T = 750 \text{ K}$
G	$6.6 \times 10^{10} \text{ Pa}$	[120], $T = 750 \text{ K}$
fcc Co		
V_{mol}	$6.8 \times 10^{-6} \text{ m}^3\text{mol}^{-1}$	[118]
E	$31.1 \times 10^{10} \text{ Pa}$	[121], $T = 710 \text{ K}$
G	$11.0 \times 10^{10} \text{ Pa}$	[121], $T = 710 \text{ K}$

leation and growth via the inverse evaluation method (consistent thermodynamic model). (ii) Inconsistent scenario: use of the relations $r(x^{\alpha,\text{m}}, \gamma, \Delta g_{\text{el}})$ and $x^{\beta,\text{p}}(x^{\alpha,\text{m}})$ for particle nucleation only; description of the Gibbs-Thomson effect for growth, i.e. of $x^{\alpha,\text{int}}(r)$, by use of Equation (5.3). The composition of the particle $x^{\beta,\text{int}}(r) = x^{\beta,\text{p}}(r)$ is then equal to 1, and the contribution of elastic energy is neglected for particle growth (inconsistent thermodynamic model).

The resulting precipitation kinetics according to both scenarios are shown in Figure 5.6. Pronounced differences of the results for both scenarios can be observed: Only in the very early stages, the mean matrix composition $\bar{x}^{\alpha,\text{m}}(t)$, the mean radius $\bar{r}(t)$, the critical radius $r^*(t)$ and the no-growth radius $r^c(t)$ (i.e. the particle radius for which $x^{\alpha,\text{int}}(r) = \bar{x}^{\alpha,\text{m}}(t)$ and $dr/dt = 0$, Equation (5.2)), and the particle number density $N(t)$ show a relatively similar evolution for both cases. Note that for scenario (ii), due to employing an inconsistent thermodynamic model, the critical radius and the no-growth radius are not identical: an existing particle of size equal to the critical particle size, or even of somewhat smaller size, still exhibits a *positive* growth rate (see footnote in Section 5.1), whereas a nucleating particle of critical size is

in (unstable) equilibrium with the matrix. Application of the classical Gibbs-Thomson equation in scenario (ii) thus results in an acceleration of the *growth* kinetics as compared to scenario (i). As a consequence, towards later stages, the enhanced growth kinetics in scenario (ii) lead to a markedly faster decrease of $\bar{x}^{\alpha,m}(t)$ and thus to a deceleration of the *nucleation* kinetics and a lower particle number density $N(t)$. When the mean matrix composition $\bar{x}^{\alpha,m}(t)$ approaches the limiting composition of so-called coherent equilibrium (i.e. accounting for the elastic energy contribution Δg_{el} , see Figure 5.3), in scenario (i) the critical radius for nucleation r^* and the no-growth radius r^c (which are in this case identical) continuously increase and eventually approach the mean particle radius \bar{r} , correlated with the onset of distinct particle coarsening, i.e. dissolution of particles with $r < r^c = r^*$. In scenario (ii), by contrast, $\bar{x}^{\alpha,m}$ can fall below the matrix composition for coherent equilibrium, which is now only limiting for particle nucleation. Consequently, the critical radius for nucleation r^* first strongly increases and is then no longer defined when $\bar{x}^{\alpha,m}$ falls below this composition value. The kinetic model of inconsistently coupled nucleation and growth thus degenerates to a model of particle growth (and coarsening) only, with $\bar{x}^{\alpha,m}$ slowly approaching the limiting matrix composition for incoherent equilibrium.

Finally, above discussed discrepancies between the consistent and the inconsistent scenario pertain to the real case Cu-Co, a model system of only modest misfit strain development. Pronounced cases of large(r) misfit abound and can lead to much larger discrepancies.

5.5 Conclusions

A general approach for evaluation of the thermodynamics of nucleation and growth, based on the thermodynamic equilibrium consideration common to both mechanisms [4], is proposed which allows to

- evaluate the thermodynamics of nucleation and growth on a consistent basis, thus excluding the corruption of kinetic modelling by incongruent description of thermodynamics,
- easily incorporate a (composition-independent) contribution of elastic energy for both nucleation and growth, or a size-dependent interface energy,
- efficiently handle numerical thermodynamic data for implementation into kinetic modelling.

Employing inconsistent thermodynamic descriptions for the evaluation of the nucleation barrier and the Gibbs-Thomson effect, as frequently done upon

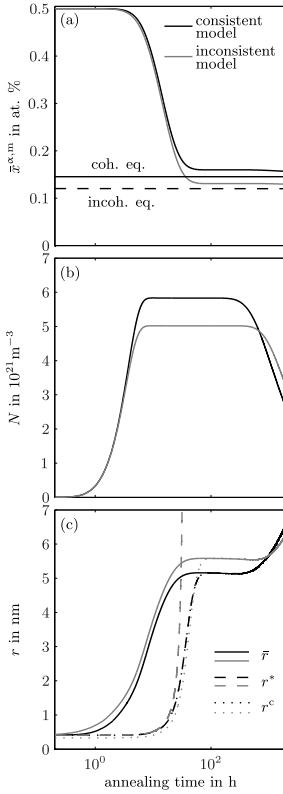


Figure 5.6: Simulation of the precipitation kinetics in a binary A-B model system (Cu-0.5 at.% Co, $T = 763$ K, $p = 10^5$ Pa) as function of time for two different cases of thermodynamic modelling of nucleation and growth (cf. Figure 5.3 (c)): (i) consistent thermodynamic model based on the relations $r(x^{\alpha,m}, \gamma, \Delta g_{el})$ and $x^{\beta,P}(x^{\alpha,m})$ for both nucleation and growth (black curves); (ii) inconsistent thermodynamic model assuming the classical Gibbs-Thomson equation (Equation (5.3)) for growth (grey curves). (a) Evolution of the mean matrix composition $\bar{x}^{\alpha,m}(t)$; for case (i), $\bar{x}^{\alpha,m}(t)$ approaches the composition of the matrix phase for coherent equilibrium, for case (ii) $\bar{x}^{\alpha,m}(t)$ approaches the composition for *incoherent* equilibrium (cf Figure 5.3). (b) Evolution of the particle number density $N(t)$. (c) Evolution of the mean radius $\bar{r}(t)$, critical radius $r^*(t)$ and no-growth radius $r^c(t)$. For the consistent scenario (i), r^* and r^c , both derived from the fundamental relation $r(x^{\alpha,m}, \gamma, \Delta g_{el})$, are identical. For the inconsistent scenario (ii), $r^*(t)$ first strongly increases when $\bar{x}^{\alpha,m}(t)$ approaches the matrix composition for coherent equilibrium and is then undefined when $\bar{x}^{\alpha,m}(t)$ drops below this composition value. The model of initially combined nucleation and growth thus degenerates to a model of particle growth only.

modelling the kinetics of nucleation and growth, can easily lead to dramatic consequences for the predicted precipitation kinetics: as demonstrated in this work, inconsistent thermodynamic modelling, manifested by, e.g., the non-identity of r^* and r^c , results in inadvertent, artificial enhancement or attenuation of either nucleation or growth, accompanied by a breakdown of the model of initially coupled nucleation and growth.

Chapter 6

Analysis of Precipitation Kinetics on the Basis of Particle-Size Distributions

Bastian Rheingans, Eric J. Mittemeijer

Abstract

A model for the description of precipitation kinetics is presented and applied to experimental data for the evolution of the particle-size distribution in a dilute model system (Cu-Co) upon isothermal annealing at different temperatures. For coupling nucleation kinetics and growth kinetics, the model includes a recently proposed inverse evaluation method for consistent and numerically efficient evaluation of the thermodynamics of both nucleation and growth. Using the experimental data for the evolution of the PSDs, obtained at least at two different temperatures, as a reference, unique and physically reasonable values for, at least, the interface energy and the activation energies for nucleation and growth can be obtained. The sensitivity of the kinetic model fitting to precise description of the thermodynamics of the particle-matrix system and the inferiority of kinetic model fitting to average data, such as data for the mean particle radius, have been highlighted.

6.1 Introduction

The kinetics of heterogeneous precipitation reactions in dilute systems is frequently described in terms of *nucleation* and *growth* of solute-rich precipitates, however, often departing from different and thus inconsistent thermodynamic bases for nucleation and growth [122]. Most of these models originate from the Kampmann-Wagner numerical (KWN)-approach [15]: In this approach, the evolution of the particle size distribution (PSD) is modelled for discrete time steps and discrete particle-size classes adopting the classical theory of nucleation [5, 6] and long-range solute diffusion controlled growth of (spherical) particles [25, 26]. The changes in particle number densities and particle sizes during one time step are calculated by numerical integration of the rate of nucleation and the rates of growth of the individual size classes which are functions of the (time-dependent) mean matrix composition. Such models can thus be classified as mean-field models for precipitation kinetics, constituted by two types of coupled kinetic rate equations, a nucleation rate and a growth rate, which are numerically solved on a discrete time-particle size grid.

The inconsistent nature of the thermodynamic treatments employed for nucleation and growth originates from the thermodynamic stability consideration for the particle-matrix system being treated separately and differently for nucleation and for growth: For nucleation, the nucleation barrier for formation of a stable second phase particle is evaluated from the release in chemical energy upon formation of the second-phase particle (the chemical driving force for nucleation) and the increase of energy due to formation of an interface between matrix and precipitate particle, and other energy contributions such as an elastic energy contribution in case of a volume misfit between precipitate and matrix. For growth, in order to describe particle coarsening in later stages of the precipitation, the Gibbs-Thomson effect is taken into account, i.e. the compositions of particle and matrix at the particle-matrix interface are taken as functions of the size of the particle, which leads to the dissolution of smaller particles once the value of the mean matrix composition falls below the size-dependent matrix composition at the particle-matrix interface. Inconsistency of the thermodynamic descriptions arises if the nucleation barrier and the Gibbs-Thomson effect are evaluated on the basis of different thermodynamic models, e.g. involving differing descriptions for the chemical Gibbs energies of the matrix phase and the precipitate phase, or an elastic energy contribution which is considered for nucleation but then neglected for growth without further reasoning. This widespread usage of inconsistent thermodynamic models for nucleation and for growth (e.g. [15, 96, 109]) can lead to unintended, pronounced biasing of the kinetic model towards artificially en-

hanced or attenuated nucleation or growth¹, as shown in [122].

In fact, the nucleation barrier and Gibbs-Thomson effect can be retraced to the same consideration of thermodynamic equilibrium for a particle-matrix system [4, 122]. This allows, as explicitly demonstrated in [122], an evaluation of the thermodynamics of nucleation and growth on a consistent basis by application of an “inverse evaluation method” [122], and provides, for typical assumptions for the interface energy and elastic misfit energy contribution, an efficacious and numerically efficient way to incorporate numerical data for the chemical driving force as derived from a thermodynamic assessment without any necessity for approximations.

The precipitation of Co-rich particles from supersaturated, dilute CuCo represents a model case of precipitation reactions: upon annealing, Co-rich particles of spherical shape are formed (more or less) randomly distributed within the Cu-rich matrix. For small particle sizes, the Co-rich particles are of fcc crystal structure and show full coherency with the surrounding matrix [56] owing to the small lattice mismatch of fcc-Cu and fcc-Co of about -1.7 %. In later stages of the precipitation reaction, upon increase in particle size, loss of coherency and transition to an octahedral particle shape have been observed [123]. Due to its showcase precipitation behaviour in the early stages of precipitation, the decomposition reaction of supersaturated Cu-Co alloys has been the object of numerous experimental studies in the past, e.g. [31–38, 62, 40, 41]. The impetus of most studies was, apart from application of novel techniques for microstructural analysis, investigating the applicability of the classical theory of (homogeneous) nucleation for precipitation in the solid state by comparing experimental results and theoretical predictions for critical particle size and (the evolution of) the particle-number density (see esp. [32, 42, 43, 8]). Some studies also accounted for concurring nucleation and growth (e.g. [39, 35]), but experiments and modelling were restricted to a single alloy composition and a single annealing temperature. Extensive simulations of the precipitation kinetics in dilute CuCo alloys employing a KWN-type approach were performed in [96, 124, 60, 125], mainly using as reference the experimental particle-density data of [32], determined by transmission electron microscopy (TEM). However, these computations were based on approximate and (again) inherently inconsistent thermodynamic models for nucleation and growth, and, moreover, the effect of elastic misfit energy was generally neglected.

In the present paper, adopting the general approach sketched in the first paragraph above, but now incorporating the recently proposed inverse eval-

¹In extreme cases, the unphysical scenario can emerge that a particle once generated by nucleation is inherently unstable with respect to growth and, in this flawed model scenario, immediately begins to dissolve.

uation method for evaluation of the thermodynamics of both nucleation and growth [122], a kinetic model is developed and applied to detailed experimental data for the development of the size distribution of Co-rich precipitate particles in a dilute Cu-Co alloy, determined in this work by TEM, upon isothermal annealing at different temperatures for various annealing times. Thereby, a high sensitivity for testing the validity of the kinetic model used is achieved. With the experimental data for the evolution of the PSDs serving as a reference, the effect of different thermodynamic approximations on the behaviour of the kinetic model, the relation between the extracted kinetic model parameters and the quantity and quality of the experimental data, and the general applicability of the mean-field approach is investigated.

6.2 Theoretical background

6.2.1 Kinetic model

Classical nucleation theory [5,6] yields an expression for the rate of formation of stable second-phase particles from a supersaturated parent phase. Particles are considered stable once they have reached a critical size, corresponding to an energy barrier for nucleation. Nucleation is assumed to occur homogeneously, i.e. in the present case of a solid solution, the formation of a nucleus is the result of short-range concentration fluctuations within the supersaturated matrix. The nucleation rate \dot{N} in a binary alloy can be expressed as

$$\dot{N} = X_1 \beta^* Z \exp\left(-\frac{\Delta G^*}{kT}\right) \times \exp\left(-\frac{\tau}{t}\right), \quad (6.1)$$

with the fraction X_1 of solute clusters of size 1, for binary alloys equal to the atomic fraction x^α of non-clustered solute atoms in the matrix, the solute capturing rate β^* of a particle of critical size, the Zeldovich factor Z , the Gibbs energy² change ΔG^* for formation of a particle of critical size, and the time lag τ required to establish a steady-state size distribution of solute clusters. k , T and t denote Boltzmann's constant, temperature and time, respectively. The solute capturing rate β^* describes the probability for the addition of a solute atom of the matrix to the particle, depending on the particle-matrix interface area, the area density of solute atoms in the matrix and the atomic jump frequency. For a spherical particle of critical size, i.e. of radius r^* , β^*

²In the present work, the Gibbs energy is used to describe the energy content change of the system considered because of experimental control of p and T .

can be expressed as

$$\beta^* = k' \times 4\pi r^{*2} \times \frac{x^\alpha}{(a^\alpha)^2} \times \frac{D_N}{(a^\alpha)^2} \quad (6.2)$$

where a^α is the lattice parameter of the matrix phase³ and k' is a proportionality factor which is generally set to one. $D_N = D_{N,0} \exp\left(-\frac{Q_N}{RT}\right)$ describes the temperature dependency of the jump frequency, defined by an activation energy Q_N and a pre-exponential factor $D_{N,0}$. For nucleation in the solid state, D_N is often identified with the (self or impurity) diffusion coefficient D_D for volume diffusion of the solute component, although classical nucleation theory does not consider (long-range) volume diffusion of solute in the matrix, but only the addition step of a solute atom to the (sub-)critical particle as a rate-limiting step; therefore, Q_N and $D_{N,0}$ can differ from the activation energy Q_D and the pre-exponential factor $D_{D,0}$ pertaining to volume diffusion of the solute component. The Zeldovich factor Z is given by

$$Z = \left(\frac{\Delta G^*}{3\pi k T n^{*2}} \right)^{1/2}, \quad (6.3)$$

where $n^* = 4/3 \pi r^{*3} / V^\beta$ is the number of atoms within a particle of critical size. For the time lag τ , Feder's approximation [126]

$$\tau = \frac{6kTn^{*2}}{\beta^* \Delta G^*} \quad (6.4)$$

is used.

Determination of nucleation barrier ΔG^* and critical size r^* requires evaluation of the change in energy ΔG of the system upon formation of a precipitate particle. Typically, ΔG is subdivided into (i) a (negative) chemical Gibbs energy contribution Δg_c (per unit volume of β) due to the decomposition of the supersaturated α matrix phase into a solute-depleted α matrix phase and a solute-rich β precipitate phase, with $-\Delta g_c$ as the (positive) chemical driving force for nucleation; (ii) a (positive) interface energy contribution γ (per unit area of interface) and (iii) a (positive) deformation energy contribution in case of a volume misfit between nucleus and matrix. In the following, only elastic accommodation of the misfit, as pertaining to the initial stages of precipitation in the system Cu-Co (see Sections 6.1, 6.4 and 6.5), will be considered. In order to simplify the thermodynamic analysis it is usually as-

³Lattice parameters a^j and atomic volumes V^j of the phases $j = \alpha, \beta$ are taken as being composition-independent.

sumed that (i) the matrix composition x^α remains constant upon formation of a β -phase particle (i.e. that the matrix phase is infinitely large or the precipitate particle is infinitesimally small), and that (ii) the contributions of interface energy (per unit area) and elastic energy (per unit volume) do not vary strongly within the ranges of composition assumed by the α phase and the β phase, and can therefore be treated as independent of the composition of α and β . These assumptions allow to *separately* evaluate the change in chemical Gibbs energy upon nucleation from a thermodynamic assessment of the bulk phases (see [122]): By use of the so-called maximum chemical driving force method [103], the (maximum) chemical driving force $-\Delta g_c = -\Delta g_c(x^\alpha)$ and the corresponding composition $x^\beta = x^\beta(x^\alpha)$ of the β phase can be derived from the chemical Gibbs energies of the α phase and the β phase as function of the composition x^α of the α -phase matrix, independent of the interface energy and elastic energy contributions. Determination of the nucleation barrier ΔG^* then reduces to finding the extremum of ΔG as function of particle size only. Adopting the sharp interface model with an isotropic interface energy γ per unit area and with Δg_{el} as the elastic energy contribution per unit volume of the particle, it follows for a spherical shape of the particle

$$\Delta G(r) = \frac{4}{3}\pi r^3 \times (\Delta g_c + \Delta g_{el}) + 4\pi r^2 \times \gamma. \quad (6.5)$$

For $(\Delta g_c(x^\alpha) + \Delta g_{el}) < 0$, $\Delta G(r)$ shows a maximum at $d(\Delta G(r))/dr = 0$ with the critical particle radius

$$r^* = -\frac{2\gamma}{\Delta g_c + \Delta g_{el}} = r(x^\alpha, \gamma, \Delta g_{el}) \quad (6.6)$$

and the nucleation barrier

$$\Delta G^* = \Delta G(r^*) = \frac{4}{3}\pi r^{*2}\gamma = \frac{16}{3} \frac{\gamma^3}{(\Delta g_c + \Delta g_{el})^2}. \quad (6.7)$$

Introducing Equations (6.2) to (6.7) into Equation (6.1), the nucleation rate can finally be expressed as

$$\begin{aligned} \dot{N} = & \frac{2x^{\alpha 2}V^\beta}{a^{\alpha 4}} \left(\frac{\gamma}{kT}\right)^{1/2} D_{0,N} \exp\left(-\frac{Q_N}{RT}\right) \times \\ & \exp\left(-\frac{16\pi}{3} \frac{\gamma^3}{(\Delta g_c + \Delta g_{el})^2 kT}\right) \exp\left(-\frac{8a\beta^4}{V\beta^2 x^\alpha D_N} \frac{\gamma kT}{(\Delta g_c + \Delta g_{el})^2} \frac{1}{t}\right). \end{aligned} \quad (6.8)$$

By employing the maximum chemical driving force to determine the critical radius r^* , the corresponding β particle of critical size r^* and composition $x^\beta(x^\alpha)$ (nucleus) is in (unstable) equilibrium with the α matrix phase of composition x^α (see, e.g., [103]).

These results allow the following generalisation: For given values of γ and Δg_{el} , the size relation $r(\Delta g_c(x^\alpha), \gamma, \Delta g_{el})$, obtained from Equation (6.6), and the composition relation $x^\beta(x^\alpha)$, directly obtained from the maximum chemical driving force method, completely characterise the thermodynamic equilibrium of the particle-matrix system in terms of the variables particle size and phase compositions [122]. This result will later be used for a consistent thermodynamic treatment of both nucleation and growth.

Upon particle growth, owing to the continuous solute depletion of the matrix around the growing solute-rich precipitate particle, the particle growth rate (eventually) becomes rate-controlled by diffusion of solute atoms through the solute-depleted matrix around the particle. Assuming a linear composition gradient within the matrix phase with the composition x^α of the undepleted α -phase matrix remote from the particle-matrix interface and the composition $x^{\alpha,int}$ of the matrix at the particle-matrix interface, for small degrees of supersaturation, the growth rate of a spherical particle of size r can be described by [25, 26]

$$\dot{r} = \frac{dr}{dt} = \frac{x^\alpha - x^{\alpha,int}}{\frac{V^\alpha}{V^\beta} x^{\beta,int} - x^{\alpha,int}} \frac{D_G}{r}, \quad (6.9)$$

with the (composition-independent) diffusion coefficient $D_G = D_{G,0} \exp\left(-\frac{Q_G}{RT}\right)$ of solute in the matrix with activation energy Q_G and pre-exponential factor $D_{G,0}$. In dilute systems, for D_G often the value of the impurity diffusion coefficient D_D of the solute in the matrix phase is taken. The compositions $x^{\alpha,int}$ and $x^{\beta,int}$ of the α phase and the β phase at the particle-matrix interface are typically evaluated assuming local establishment of thermodynamic equilibrium at the particle-matrix interface under consideration of the Gibbs-Thomson effect, i.e. accounting for the finite size of the β -phase particle. Resorting to the same thermodynamic model as used above for the description of nucleation thermodynamics, the relations $x^{\alpha,int}(r)$ and $x^{\beta,int}(r)$ as function of particle size r can directly⁴ be derived from the relations $r(\Delta g_c(x^\alpha), \gamma, \Delta g_{el})$ and $x^\beta(x^\alpha)$, determined for nucleation, which completely characterise the thermodynamics of the particle-matrix system (see above) [122]: by inverse evaluation of $r(\Delta g_c(x^\alpha), \gamma, \Delta g_{el})$, the composition relation $x^{\alpha,int}(r) = x^\alpha(r, \gamma, \Delta g_{el})$ for the α phase and, via $x^\beta(x^\alpha)$, the corresponding compos-

⁴in case of a binary system; for multinary systems cf. [122]

ition relation $x^{\beta,\text{int}}(r) = x^{\beta}(x^{\alpha} = x^{\alpha,\text{int}})$ for the β phase can be obtained.⁵ Using the proposed inverse evaluation method, separate evaluations of the thermodynamics of nucleation and of growth are rendered unnecessary – a single evaluation of the thermodynamics of the particle-matrix system is sufficient. In this case, the so-called no-growth radius r^c , the radius for which $x^{\alpha,\text{int}}(r) = x^{\alpha}$ and $\frac{dr}{dt} = 0$ (Equation (6.9)), and the critical radius for nucleation r^* at given x^{α} are truly identical, and inconsistent application of two differing thermodynamic descriptions of the particle-matrix system is thus avoided inherently (see [122]).

Both the rate equation for nucleation, equation (6.8), and the rate equation for growth, equation (6.9), are functions of the matrix composition x^{α} . Combining the two rate equations via a mean-field approach for the matrix composition, i.e. substituting the matrix composition x^{α} by the average matrix composition \bar{x}^{α} , the evolution of the particle-size distribution can be computed as function of time and temperature upon concurring particle nucleation and particle growth ([15], see Section 6.1). The incorporation of the Gibbs-Thomson effect in the model for growth implies that particle growth also comprises particle shrinkage if the mean matrix composition $\bar{x}^{\alpha}(t)$ falls below the size-dependent composition $x^{\alpha,\text{int}}(r)$ for a particle of certain size. Thus, particle coarsening is inherently included in this type of model (provided consistent thermodynamics apply to both nucleation and growth; cf. footnote in Section 6.1).

6.2.2 Model application

As for application of the preceding KWN-type models, in the present work it is assumed that the interface energy γ and, if present, the elastic misfit energy Δg_{el} contributions (as well as the atomic volumes) are independent of (varying) phase composition (see above), and that the properties of the α -matrix phase and the β -particle phase can be described adequately by the properties of the corresponding *bulk* phases. Thereby an independent determination of the (maximum) chemical driving force for nucleation from a thermodynamic assessment of the bulk phases (e.g. a CALPHAD assessment) becomes possible and the elastic misfit energy Δg_{el} contribution can be calculated from bulk elastic properties using an appropriate model. Values for the interface energy γ from independent (i.e. non-kinetic) measurements are typically not available and can only roughly be assessed from bulk properties, which is usually not sufficient for kinetic modelling owing to the high sensitivity of the nucleation

⁵A size dependency of the interface energy, as sometimes found to be necessary to model the growth kinetics in later stages of the precipitation reaction (e.g. [98]), can be implemented by re-deriving r^* from Equation (6.5) with $\gamma = \gamma(r)$.

rate for the value of γ (Equation (6.8), see also [15] on that aspect). The interface energy can therefore be used as an adaptable model parameter to achieve good agreement between kinetic model and experimental data.

6.3 Model implementation

For modelling the evolution of the PSD, the PSD is typically divided into l discrete particle size classes ($r_1, \dots, r_k, \dots, r_l$). In the current work, a class management similar to the ‘‘Lagrange-type’’ approach proposed in [127] was adopted: the radius r_k of a particle class k varies by positive or negative growth, while the population density N_k of the class is kept constant. By nucleation, in the i -th time step Δt_i a new particle class with particle size $r_{l+1,i} = r_i^* + \Delta r_N$ and particle density $N_{l+1,i}$ is generated and added to the l existing classes, where Δr_N is an initial growth step to render the particle super-critical (here Δr_N is set equivalent to the addition of one (fcc Co) atom). The radius $r_{k,i}$ of an existing particle size class k grows (or shrinks) by $\Delta r_{k,i}$ during one time step. A particle class is removed from the simulation if its radius falls below a threshold $r_{\text{cut-off}}$ to avoid numerical problems for $r \rightarrow 0$ (see Equation (6.9); $r_{\text{cut-off}}$ is here set equivalent to five (fcc Co) atoms). Additional class management to maintain a certain minimum number of classes upon dissolution of particles was in the present case not necessary, since experiments and model application were restricted to early stages before onset of substantial (dominant) particle coarsening and dissolution.

The particle density $N_{l+1,i}$ of the newly generated class and the radius changes $\Delta r_{k,i}$ of existing classes are calculated from the rate of nucleation $\dot{N} = dN/dt$ (Equation (6.8)) and the growth rate $\dot{r} = dr/dt$ (Equation (6.9)), respectively, by numerical integration. \dot{N} and \dot{r} are ordinary differential equations (ODEs) of first order, coupled by their dependence on the mean matrix concentration $\bar{x}^\alpha(t)$. Here, the ODEs were numerically solved using a fourth-order Runge-Kutta algorithm for coupled ODEs with an adaptive time step length Δt_i to increase numerical efficiency. Two criteria for a maximum time step length were imposed: (i) a maximum relative change in mean matrix composition of 2×10^{-4} during a time step; and (ii) a maximum number of two classes being removed from the simulation during one time step by coarsening (i.e. dissolution of smallest particles). To speed up the computation, the length of the adaptive time step was determined in a preceding estimator step using a linear finite-difference approximation before calculation of the final values with the fourth-order Runge-Kutta algorithm.

The mean concentration of the matrix at certain time $t_j = \left(\sum_{i=1}^{j-1} \Delta t_i \right) + \Delta t_j$,

either after completion of the time step Δt_j or for the intermediate time steps of the Runge-Kutta algorithm, is obtained from the mass balance

$$\bar{x}^\alpha(t_j) = x^{\alpha,0} - \sum_{k=1}^l N_{k,j} \frac{4}{3} \pi r_{k,j}^3 x^\beta(r_{k,j}), \quad (6.10)$$

where $x^{\alpha,0}$ is the total solute content, with summation over all currently existing size classes k , presuming a homogeneous composition within the particle (i.e. infinitely fast diffusion within the particle phase) with $x^\beta(r_{k,j})$ equal to $x^{\beta,\text{int}}(r_{k,j})$, the composition of the β -phase particle at the particle-matrix interface.

The assumption of composition-independent contributions of interface energy γ and elastic energy Δg_{el} allows to independently determine the (maximum) chemical driving force $-\Delta g_c(x^\alpha)$ and the composition relation $x^\beta(x^\alpha)$ at given temperature from a thermodynamic assessment of the chemical Gibbs energies of the phases (Section 6.2), thus substantially reducing the computationally costly access to the thermodynamic database to its minimum. The thermodynamic input data was extracted from a recent CALPHAD assessment of the system Cu-Co [29] (Figure 6.1).

If a full thermodynamic assessment for the α phase and the β phase⁶ is not available, the change in chemical Gibbs energy upon nucleation is often derived using analytical equations based on simple thermodynamic models, e.g. ideal or regular solution models, which allow to determine $-\Delta g_c(x^\alpha)$ as function of the matrix composition x^α based on the phase compositions $x^{\alpha,\text{eq}}$ and $x^{\beta,\text{eq}}$ for equilibrium of the bulk phases (as given in a temperature-composition phase diagram at constant pressure). Presuming ideal or regular behaviour of the α solution phase and a β phase of fixed composition, $-\Delta g_c(x^\alpha)$ can be assessed via [101]

$$-\Delta g_c^{\text{approx.}}(x^\alpha) = + \frac{RT}{V^\beta} \left[x^{\beta,\text{eq}} \ln \left(\frac{x^\alpha}{x^{\alpha,\text{eq}}} \right) + (1 - x^{\beta,\text{eq}}) \ln \left(\frac{1 - x^\alpha}{1 - x^{\alpha,\text{eq}}} \right) \right]; \quad (6.11)$$

see Figure 6.1 for $\Delta g_c^{\text{approx.}}(x^\alpha)$ at 773 K, used in Section 6.6.2 for investigating the influence of the thermodynamic model on the predicted kinetics.

Upon kinetic modelling, for given values of the interface energy γ and of the elastic energy Δg_{el} , the relation $r(\Delta g_c(x^\alpha), \gamma, \Delta g_{\text{el}})$ (cf. Equation 6.6) can then be (re-) evaluated straightforwardly, providing a description for the critical radius $r^*(x^\alpha) = r(\Delta g_c(x^\alpha), \gamma, \Delta g_{\text{el}})$ as function of the matrix compos-

⁶i.e. a description of the chemical Gibbs energies of α and β , or of the corresponding activity coefficients, as function of alloy composition and temperature

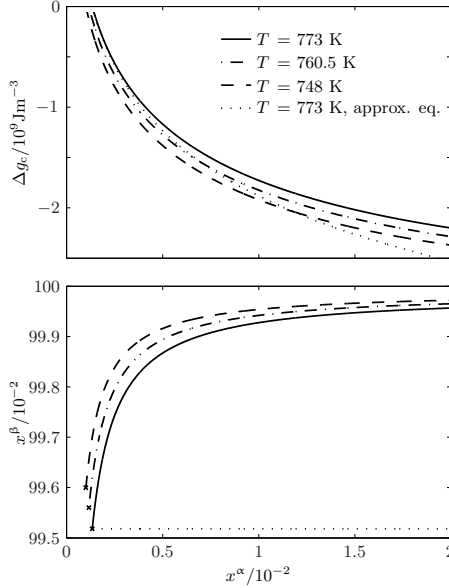


Figure 6.1: The chemical Gibbs energy change $\Delta g_c(x^\alpha) = \Delta g_c(x^{(\text{Cu})})$ and the composition relation $x^\beta(x^\alpha) = x^{(\text{Co})}(x^{(\text{Cu})})$ as function of the matrix composition $x^\alpha = x^{(\text{Cu})}$, derived from a CALPHAD assessment of the system Cu-Co [29] for the experimental annealing temperatures $T = (773, 760.5, 748) \text{ K}$ (initial composition $x^{(\text{Cu}),0} = 0.57 \text{ at. \%}$). The dotted line represents the chemical Gibbs energy change for $T = 773 \text{ K}$ as determined by application of an approximate equation (Equation (6.11)) based on the phase compositions for equilibrium between bulk phases.

ition x^α and, by application of the inverse evaluation method, the relations $x^{\alpha,\text{int}} = x^\alpha(r, \gamma, \Delta g_{\text{el}})$ and $x^{\beta,\text{int}} = x^\beta(x^\alpha)$ required for calculation of the particle-growth rate. During the actual numerical computation routine, the necessary data pertaining to the instantaneous mean matrix concentration $\bar{x}^\alpha(t)$ and to a certain particle radius r_k can thus be accessed rapidly via a table-lookup.

The elastic energy contribution caused by a misfitting coherent spherical particle (as holds for the Co precipitates in this work) was calculated according to [119]

$$\Delta g_{\text{el}} = 2\mu^\alpha \frac{3K^\beta}{3K^\beta + 4\mu^\alpha} \frac{(V^\alpha - V^\beta)^2}{3V^\beta} \quad (6.12)$$

with the shear modulus μ^α of the α -phase matrix and the effective bulk modulus K^β of the β -phase particle, adopting elastic isotropy of both matrix and precipitate phase. In the present case, the elastic constants and atomic volumes of the pure bulk components were employed. Due to the small mutual solubility of Co and Cu (cf. Figure 6.1), the thus introduced errors can be neglected. The values used for the elastic constants of Co and Cu, the atomic volumes/lattice parameters and the impurity diffusion coefficient of Co in fcc Cu have been listed in Table 6.1.

The above outlined efficient usage of thermodynamic data, largely due to the usage of the proposed inverse evaluation method, allows to employ an automatic optimisation algorithm for fitting the kinetic model to the experimental data within reasonable computation time. Since both experimentally determined PSD and calculated PSD consist of usually differing, discrete particle size classes, for model fitting (and visualisation) of the data the PSDs were described by kernel density estimates (KDEs)⁷ employing a Gaussian kernel with a band width of 2×10^{-10} m (cf. experimental error of the radius determination; see Section 6.4). As cost function for fitting, the sum of the mean squared differences of experimental KDE and calculated KDE was used, with summation over all considered experimental PSD data series obtained at different annealing times and, when applicable, at different annealing temperatures.

6.4 Experimental procedure

A Cu-0.57 at.% Co master alloy was prepared by inductive melting from pure Cu and pure Co (Cu: 99.999 at.% purity, Co: 99.98 at.% purity). To achieve a

⁷As compared to a representation of the data as histograms, the KDE approach avoids classification of the PSD into fixed, discrete particle size classes.

Table 6.1: Property parameters of Cu and Co used for the kinetic modelling. Q_D : activation energy for impurity diffusion of Co in fcc Cu; $D_{D,0}$: corresponding pre-exponential factor; V : atomic volume; E : Young's modulus, μ : shear modulus.

parameter	value	source, remark
Q_D	214 kJmol ⁻¹	[73]
$D_{D,0}$	4.3×10^{-5} m ² s ⁻¹	[73]
fcc Cu		
V	(T -dependent)	[118]
E	18.1×10^{10} Pa	[120], $T = 750$ K
μ	6.6×10^{10} Pa	[120], $T = 750$ K
fcc Co		
V	(T -dependent)	[118]
E	31.1×10^{10} Pa	[121], $T = 710$ K
μ	11.0×10^{10} Pa	[121], $T = 710$ K

homogeneous distribution of Co, the alloy rod was annealed under protective Ar atmosphere for 70 h at 1300 K within the single phase region and afterwards quenched in ice water. The Co concentration of the homogenised master alloy was determined by inductively coupled plasma optical emission spectroscopy (ICP-OES) to be (0.571 ± 0.007) at.% Co.

Afterwards, the master alloy rod was swaged down to 3 mm diameter and cut into specimen rods of about 20 mm length. To achieve a large average grain size and a low defect density, a second homogenisation treatment at 1300 K for 100 h was performed, followed by quenching in ice water to preserve a super-saturated solid solution (the presence of a homogeneous solid solution after quenching was checked by additional magnetisation measurements showing only diamagnetic behaviour).

Annealing was performed in a fluidised sand bath to ensure fast up-heating of the specimens and good temperature stability during isothermal holding. Temperature during annealing was monitored using a Pt resistance thermometer. The actual temperature was within ± 0.7 K of the preset temperature with a standard deviation of the mean temperature of less than ± 0.03 K. Specimen rods were annealed at annealing temperatures of $T = (773, 760.5, 748)$ K for various different times, followed by a quench in ice water.

For TEM analysis, disks were cut from the specimen rods and ground down

to approx. 120 μm thickness. Preparation of electron transparent foils was performed by electrolytic thinning using a Struers Tenupol 5 polishing unit and a phosphoric acid electrolyte (55 vol. % demineralised water, 30 vol. % 85 vol. %-phosphoric acid, 15 vol. % ethylene glycol; best results were obtained for polishing at a voltage of 3 V). To reduce surface oxidation, the foils were prepared immediately before TEM investigation and were kept immersed in ethanol before insertion into the microscope. For TEM analysis, a Zeiss 912 Ω TEM operating at 120 kV accelerating voltage was used. The instrument is equipped with an electron energy loss spectroscopy (EELS) filter which allows the determination of the foil thickness of the investigated area by application of the log-ratio method [66, 128]. Digital TEM bright-field (BF) images were recorded for low-order zone axis (ZA) beam incidence (typically $\langle 100 \rangle$, $\langle 110 \rangle$ or $\langle 111 \rangle$ zone axes of Cu). Under BFZA conditions, coherent Co-rich particles are visible by a dark circular strain contrast [38, 59]; for the system Cu-Co, the mass contrast caused by the local enrichment in Co atoms is negligible for small Co-rich particles). The detection of Co-rich precipitates within a Cu-rich matrix by BFZA TEM is effectively limited by its strain contrast: For particles with radius smaller than about 1 nm, the strain contrast becomes too weak to be reliably detected [38]. Upon applying the present kinetic model to the experimental data, model fitting (see Section 6.3) was therefore restricted to particle-size regions above 1 nm.

By quantitative evaluation of the digital TEM images, the (two-dimensional) particle positions, particle radii and particle (number) density per area were determined. Introducing the thickness information obtained with the log-ratio method, the particle numbers per sampled volume were derived. According to strain-contrast simulations for coherent Co particles in a Cu matrix under BFZA-conditions [38], particle radii derived from the strain-contrast are within ± 0.1 nm of the true particle radii; this range clearly exceeds the experimental uncertainty of the TEM BF magnification calibration. In practice, the accuracy of the particle-size measurement is determined by the analysis of the digital TEM micrograph: technically, the precision of the radius determination is limited by the digital image resolution (here typically 0.18 nm/pixel), with some additional arbitrariness introduced by human evaluation. The error of the radius values was thus assessed as 0.2 nm. The accuracy of the thickness values derived with the log-ratio method is about 20 % [66]. This has an only linear effect on the accuracy of the particle-density values (the error of the image area determination can, in comparison, be neglected). Thus, the inaccuracies of the radius measurement and of the thickness measurement have relatively small effect on the PSDs, the mean particle radii and the particle densities. However, their effect is much stronger for the volume fraction of precipitates in view of its r^3 -dependency. The volume fraction determined

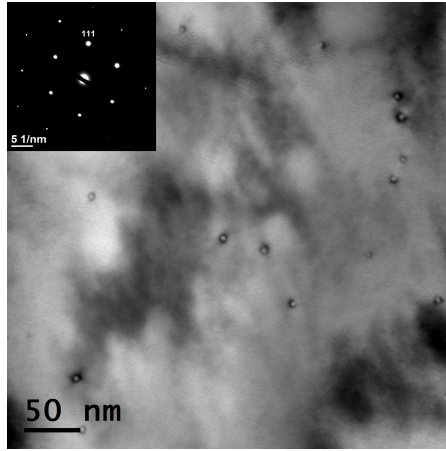


Figure 6.2: TEM image of Cu 0.57 at.% Co after annealing at 773 K for 4 h. The image is recorded under bright-field zone-axis conditions (fcc Cu (111) electron beam incidence; see diffraction pattern in the inset). The coherent Co-rich particles are (indirectly) visible because of the dark strain contrast rings resulting from the lattice misfit of fcc Cu and fcc Co.

by TEM image analysis is thus a relatively unreliable parameter to trace the progress of the precipitation reaction.

6.5 Experimental results

A typical TEM BFZA image of Cu-0.57 at.% Co after isothermal annealing of the supersaturated alloy within the two-phase region is shown in Figure 6.2. The formation of spherical Co-rich particles of about 3 nm to 7 nm in diameter is indicated by the dark strain-contrast rings. Consistent with TEM BF contrast calculations [38] particles below a lower limit of 0.8 nm to 1.0 nm were not detected.

Quantitative analysis of the TEM BFZA micrographs primarily yields the individual particle sizes and the number of particles per sampled volume. The mean particle size \bar{r} , particle density N_V and volume fraction f_V of the second-phase particles can then be derived directly from these discrete experimental data (Figure 6.3). The observed particle-number densities of the present study are comparable to TEM-based particle-number densities for precipitation reactions in dilute Cu-Co alloys obtain under similar experimental conditions in [32].

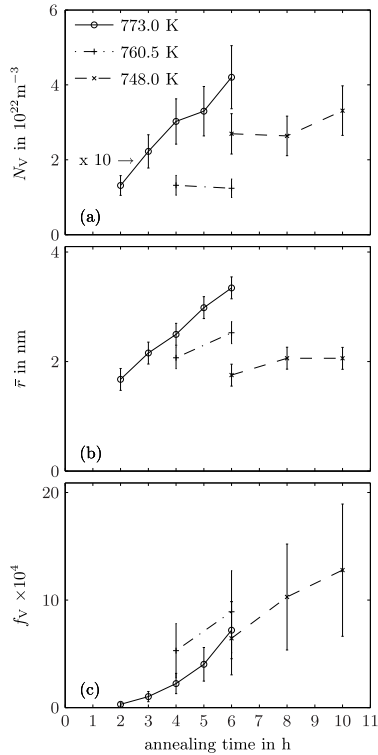


Figure 6.3: Evolution of (a) particle number density (multiplied by factor 10 for $T = 773.0$ K), (b) mean particle radius and (c) volume fraction of precipitates as function of annealing time upon isothermal annealing of Cu-0.57 at.% Co alloys at 773.0 K (\circ), 760.5 K ($+$) and 748.0 K (\times), respectively.

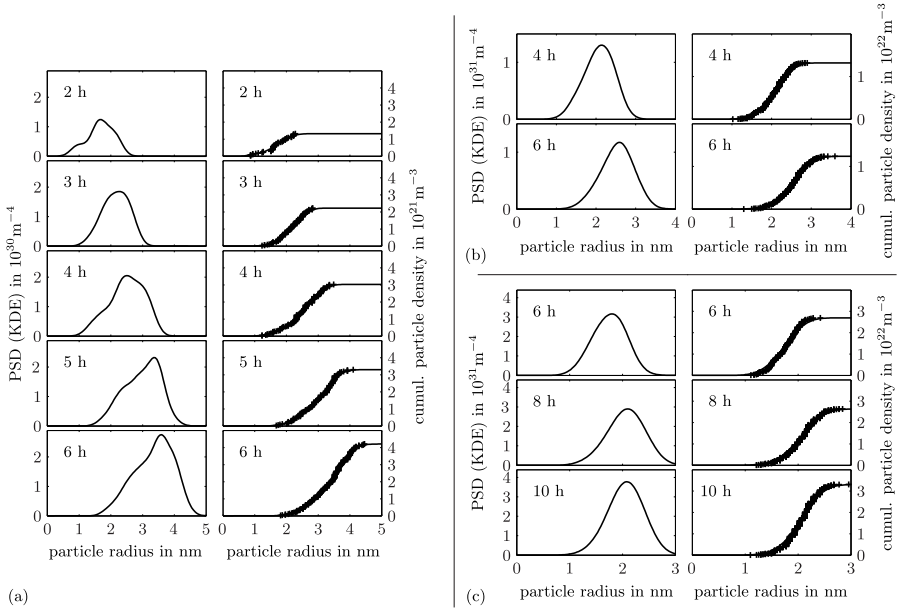


Figure 6.4: Evolution of the particle-size distribution for annealing of Cu 0.57 at.% Co alloys at different isothermal annealing temperatures as derived from TEM BFZA micrographs: (a) $T = 773.0$ K, (b) $T = 760.5$ K, (c) $T = 748.0$ K. Left columns: representation of the experimental data as kernel density estimate (KDE) of the PSD (cf. Section (6.3)); right columns: comparison of the cumulative KDEs (lines) and the cumulative of the discrete number densities of particles of certain size per volume (crosses) as directly derived from the experimental data.

The kernel density estimates (KDEs) of the PSDs (cf. Section 6.3) derived from the experimental data are shown in Figure 6.4. A comparison of the cumulative KDEs and the cumulative number of particles per volume, as derived directly from the discrete experimental data without classification of particle size, is also presented in Figure 6.4. It follows that the experimental data are represented adequately by the KDEs.

The evolution of particle size and particle-number density at different isothermal annealing temperatures clearly displays the influence of supersaturation: with decreasing annealing temperature and thus increasing degree of supersaturation (and increasing chemical driving force), the particle density strongly increases while the average particle size decreases (Figure 6.3 (a),(b); cf. Equations (6.6) and (6.8)). The effect of temperature decrease on the thermal activation of the nucleation process and the growth process, which

by itself would lead to an overall retardation of the precipitation kinetics, is not directly apparent in the temperature range under investigation (cf. Figure 6.3, also see discussion in Section 6.6.4). In contrast to the evolutions of mean particle size \bar{r} and density N_V , which strongly depends on temperature, the evolution of the volume fraction f_V (Figure 6.3 (c)) seems much less dependent on temperature. This indicates that the volume fraction of precipitates is not a very sensitive experimental parameter to trace the progress of the precipitation reaction (also see remark on the accuracy of f_V in Section 6.4).

The drastic influence of supersaturation on particle size and number density leads to a confined window of annealing time and temperature (as well as composition, see [32]) in which experimental (TEM-based) investigation of the precipitation kinetics is possible: For short annealing times at high temperatures, the number of particles per sample volume is too low to allow reliable detection and thus statistically sound derivation of the PSD. This is the case for the PSD derived for $t = 2$ h at $T = 773$ K in Figure 6.4 (a); this data set is therefore left out in further kinetic analysis. On the other hand, upon annealing at lower temperatures, the initially very small particle sizes inhibit a TEM-based analysis of the very early stage of the precipitation process owing to the experimental detection limit set by the strain-contrast conditions for small particles (see Section 6.4).

6.6 Modelling results and discussion

6.6.1 General model behaviour

Using the experimental data for the evolution of the particle-size distribution as a reference, a series of exemplary cases for model application can be addressed.

Following the modelling approach as described in Sections 6.1 and 6.2, the model is in a first step applied to the experimental data for the highest isothermal annealing temperature with the interface energy γ as only adaptable model parameter, i.e. setting the diffusional rate coefficients D_N for nucleation (Equation 6.8) and D_G for growth (Equation 6.9) to the value for the impurity diffusion coefficient D_D of Co in Cu ([73], see Table 6.1). Thus fitting the model to the dataset for annealing at $T = 773$ K leads to an overall good agreement between simulated PSDs and experimentally determined PSDs at 773 K (Figure 6.5, case A in Table 6.2; for discussion of the modelling results with respect to the system Cu-Co, see below): the size distributions cover similar size ranges with similar population density. For the shorter annealing times (2 h to 4 h), somewhat larger discrepancies between experimentally de-

terminated and modelled PSDs are present for small particle sizes around the detection limit equal to 1 nm, which was used as lower size limit for fitting. For the longer annealing times, i.e. upon continued particle growth, the discrepancies become smaller and very good agreement between simulation and experiment is achieved. Restricting the model fit to the experimental data for the shorter annealing times of 3 h and 4 h (the data for the shortest annealing time cannot be considered; see discussion of Figure 6.4 (a) in Section 6.5) leads to the same value for the interface energy and thus to no better description of the experimental data. This inability of the model to describe the experimental data more precisely might indicate that the model would principally not be capable to adequately describe the precipitation kinetics for short annealing times. However, this is incompatible with the observed good agreement for longer annealing times. Hence, it appears more plausible that the experimental data for the shorter annealing times is considerably biased by the – in practice not necessarily sharp – experimental detection limit around $r \approx 1$ nm.

With the effect of the experimental detection limit again taken into account, i.e. omitting all particle size classes with radius below 1 nm, the evolution of the average parameters, the particle-number density, the mean radius and the volume fraction of precipitates, is matched very well (see Figure 6.5).

The experimentally observed bimodal shape of the PSDs can be well described by the kinetic model and thus, according to the model, is a straightforward consequence of the size-dependency of the rate equation for growth, Equation (6.9), in combination with nucleation (see [96]): it follows from Equation (6.9) that the size-dependent growth rate must show a maximum at a certain particle size $r > r^* = r^c$ close to r^* (see Figure 6.6). In the early stages of the precipitation reaction, the population density of the PSD in size regions slightly larger than r^* is continuously increased by continuous nucleation of particles. After first experiencing a moderate (positive) growth rate (dominated by the Gibbs-Thomson effect), particles then enter a size region associated with the maximum growth rate and thus grow rapidly until the growth rate becomes attenuated due to its inverse proportionality to particle size. This leads to a local minimum of the population density in the size region associated with the maximum growth rate and thus to a bimodal shape of the PSD.

The development of a bimodal PSD may only be observable in the early stages of the modelled precipitation reaction: in advanced stages of precipitation, the relative contribution of recently nucleated particles to the total number of particles decreases, (also) owing to the decrease of the nucleation rate due to matrix depletion, and the bimodality disappears. In case of inconsistent thermodynamic modelling, leading to non-identity of r^* and r^c (cf.

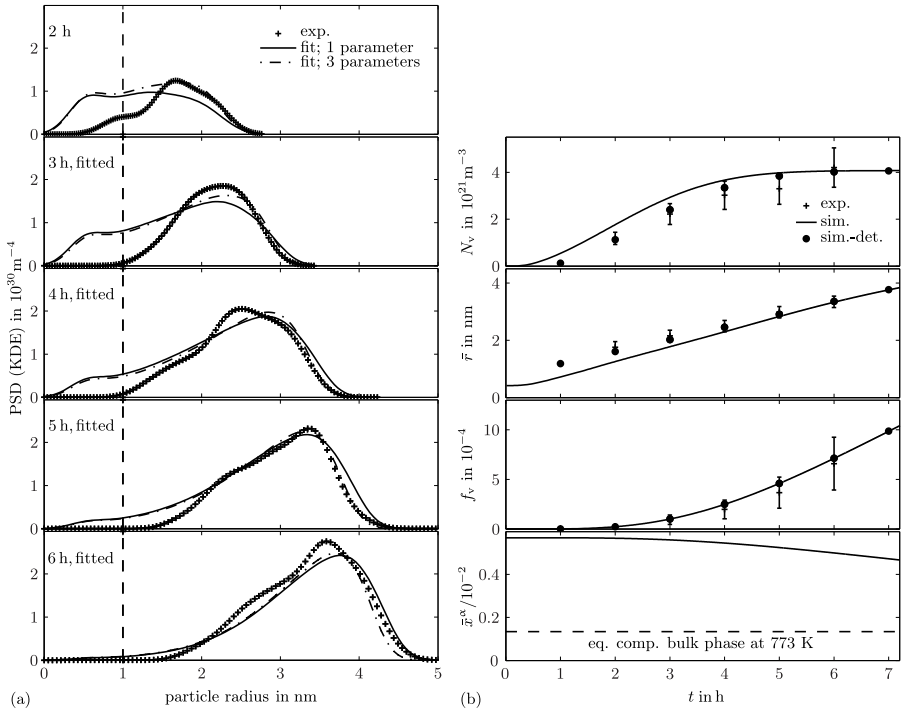


Figure 6.5: (a) Model fits of the experimentally determined evolution of the PSD at 773 K. Solid lines: using the interface energy γ as only fit parameter and setting the rate coefficients D_N and D_G to the value D_D for the impurity diffusion coefficient of Co in Cu (case A in Table (6.2)). Dash-dotted lines: using the interface energy γ and the pre-exponential factors of D_N and D_G , i.e. $D_{N,0}$ and $D_{G,0}$, as fit parameters (case F in Table (6.2)). Markers: experimental data. Dashed vertical lines: lower limit of the fitting range, accounting for the experimental detection limit for particle radii around 1 nm (data for $t = 2$ h was not considered upon fitting). Especially for the longer annealing times of 5 h and 6 h, good agreement of model and experimental data is achieved. (b) Evolution of the average parameters particle-number density N_V , mean radius \bar{r} and volume fraction of precipitates f_V , and of the mean matrix composition \bar{x}^α as follows from the one-parameter fit. Solid lines: results of the model fit in (a). Data with error bars: experimental data. Circles: calculated from fit results subject the lower limit of the fitting range at 1 nm.

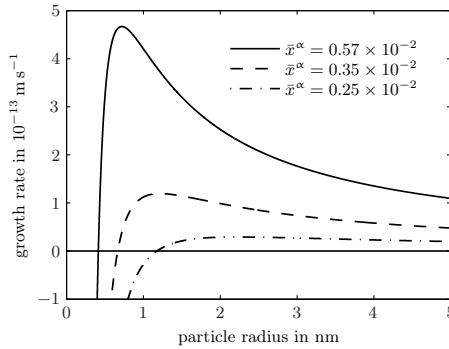


Figure 6.6: Particle growth rate $\frac{dr}{dt}$ (Equation (6.9)) as function of particle size r for different values of the matrix composition (for case A in Table (6.2)). For large particle size, the growth velocity is dominated by the term $v \propto r^{-1}$. For a particle radius equal to the critical size $r^* = r^c$, the growth rate equals zero owing to the Gibbs-Thomson effect. At intermediate particle size, the growth rate assumes a maximum; evidently, the particles quickly outgrow this size region.

Section 6.2), the particle size of a particle newly generated by nucleation may, in terms of growth, (non-physically) already be considerably larger than the no-growth radius and lie within the region of maximum growth rate, thus erroneously precluding the emergence of a bimodal size distribution (see also footnote in Section 6.1).

6.6.2 Influence of the thermodynamic description

The nucleation rate and the growth rate are strongly dependent on the model adopted to describe the thermodynamics of the particle-matrix system, represented by the relations $r(\Delta g_c(x^\alpha), \gamma, \Delta g_{el})$ and $x^\beta(x^\alpha)$. These relations, providing a complete characterisation of the thermodynamics of the particle-matrix system (see Section 6.2), define the critical particle size $r^* = r(\Delta g_c(x^\alpha), \gamma, \Delta g_{el})$ for nucleation and the composition of the nucleus, as well as the compositions of particle and matrix at the particle-matrix interface $x^{\alpha, \text{int}} = x^\alpha(r, \gamma, \Delta g_{el})$ and $x^{\beta, \text{int}} = x^\beta(x^\alpha)$ under consideration of the Gibbs-Thomson effect. The value the interface energy γ assumes upon model fitting thus necessarily depends on the chemical energy contribution $\Delta g_c(x^\alpha)$ and the elastic misfit energy contribution Δg_{el} , as derived from literature data for the bulk system (see, e.g., [129, 130]).

As can be inferred from the fair agreement between kinetic model and experiment obtained above (case A in Table 6.2, Figure 6.5), the thermodynamic

model used in the present study appears to be of sufficient quality to adequately describe the system properties for application in a kinetic model. To assess the consequences of the choice of a specific thermodynamic model for nucleation and growth on the kinetics of nucleation and growth, two different scenarios can be investigated:

(i) *Sensitivity for chemical driving force:* In the present case, thermodynamic data for the (maximum) chemical driving force $-\Delta g_c(x^\alpha)$ and the phase-composition relation $x^\beta(x^\alpha)$ was extracted from a recent CALPHAD assessment of the binary system [29]. If a thermodynamic assessment of the alloy system is not available, the chemical driving force is often derived using analytical equations based on simple thermodynamic solution models (see Section 6.3, Equation (6.11)). Employing such an expression for the present case, a somewhat different dependency of $\Delta g_c(x^\alpha)$ on the matrix composition x^α is obtained (see Figure 6.1). Upon fitting the kinetic model with this modified thermodynamic input data to the experimental data for $T = 773$ K, an acceptable description of the experimental data can still be achieved (case B in Table 6.2), however, with a considerably different value for γ . This illustrates the sensitivity of the value assumed by γ in the kinetic model for the precise thermodynamics of the system [8]. The good agreement of kinetic model and experiment still obtained in case B, albeit using a less appropriate description for the chemical driving force $-\Delta g_c(x^\alpha)$, does not hold generally and here is due to the small mutual solubility of fcc Cu and fcc Co.

(ii) *Sensitivity for misfit-strain energy:* An often made simplification of the thermodynamic model for analysing precipitation kinetics (in the system Cu-Co) is to neglect the contribution of the elastic misfit energy Δg_{el} (e.g. [124]). In the present case, Δg_{el} , computed with a simple Eshelby model ([119], Section 6.3) amounts to less than 10 % of the initial chemical driving force at $t = 0$. Performing a model fit with Δg_{el} set to zero results in a drastic change of γ (case C in Table 6.2): The model reacts by considerably increasing the value of the interface energy to emulate the effect of a net driving force reduced by the elastic energy contribution. Moreover the corresponding model description is of reduced quality⁸ (see Table 6.2).

The dependence of the interface-energy values, as obtained from kinetic analysis, on the precise thermodynamics of the system renders direct, quantitative comparison of values for γ derived from kinetic studies based on differing thermodynamic descriptions difficult, if not impossible.

The pronounced consequences of applying inconsistent thermodynamic descriptions in kinetic models, as resulting from a combination of different ap-

⁸This is in particular caused by the different dependency of the size relation $r(\Delta g_c(x^\alpha), \gamma, \Delta g_{el})$ on γ and Δg_{el} (Equation (6.6)).

proximate expressions for nucleation thermodynamics and growth thermodynamics, or from consideration of an elastic strain energy contribution only for nucleation but not for growth, have been demonstrated in [122].

6.6.3 Limitations of kinetic model fitting to averaged experimental data

Comparison of model and experiment has in the literature often been restricted to only the evolution of the particle-number density and/or the mean particle radius, i.e. the analysis has been restricted to *average* PSD parameters which do not provide a comprehensive characterisation of the underlying PSD.⁹ In such a case good agreement between model and experiment can be achieved for the average parameters, but the modelled PSD parameters can be incompatible with the in reality occurring underlying particle-size distributions. Such good agreement for the average parameters then actually occurs only for the range of experimental data considered in the model fitting.

To reveal the significance of kinetic model fitting to full PSDs, the kinetic model was fitted in the current work also to only the experimental data for the particle-number density N_V or those for the mean radius \bar{r} (in both cases, again only particle-size classes above 1 nm were considered in order to account for the experimental detection limit, cf. Section 6.4). Again using the interface energy γ as only fit parameter, results identical to those obtained upon fitting the full PSD were obtained for the case of taking N_V as reference (case D in Table 6.2), but not for the case of taking \bar{r} as reference (case E in Table 6.2): Although good agreement between model and experimental data is achieved for \bar{r} , the underlying calculated PSDs and the experimental PSDs differ strongly (see Figure 6.7). Evidently, the particle-number density and the mean particle radius show different sensitivity towards changes of the value for the interface energy: while the nucleation rate, and thus the particle-number density, depends very sensitively on the value assumed by γ , the evolution of the mean particle radius as function of time and temperature is predominantly controlled by the diffusion coefficient and to a much lesser extent by the Gibbs-Thomson effect, and thus by the value of γ . Hence, at least in the present case, fitting to the experimental data for the evolution of the mean particle radius does not allow to define the kinetic model parameters (here only γ) to correctly describe the precipitation kinetics.

⁹This, of course, can be ascribed to the experimentally cumbersome determination of the evolution of the PSD as function of annealing time and temperature by using direct imaging techniques (as employed in the present case) or by its extraction from primary experimental data (e.g. in case of scattering experiments) [101].

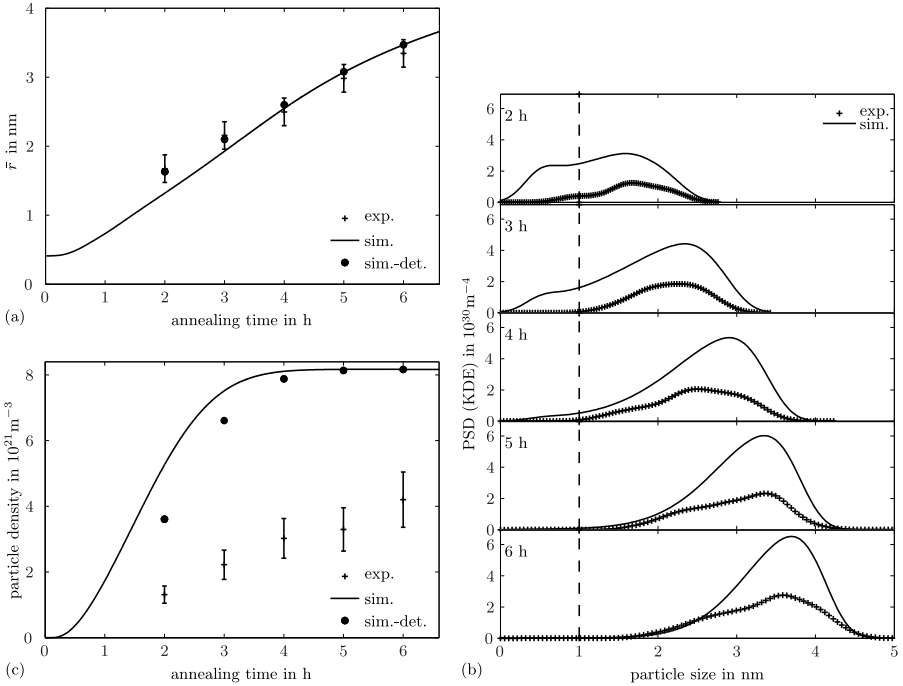


Figure 6.7: Results of fitting the kinetic model to only the experimentally determined evolution of the mean radius \bar{r} at $T = 773 \text{ K}$ using the interface energy γ as fit parameter and with $D_N = D_G = D_D$ (case E in Table (6.2)). While the evolution of the mean radius (a), evolution for model fitting, is described quite accurately with $\gamma = 223 \text{ mJ m}^{-2}$, the evolution of the underlying PSD as then follows from the kinetic model (b) and thus also the evolution of the particle number density N_V (c) strongly disagree with the experimental data.

6.6.4 Independent variation of nucleation and growth kinetics; utilising the full PSDs at different temperatures

Usage of only the interface energy as an adaptive parameter to achieve good agreement of model prediction and experimental data affects in a prescribed way both nucleation kinetics and growth kinetics simultaneously via the characteristic thermodynamic relation $r(\Delta g_c, \gamma, (x^\alpha), \Delta g_{el})$ (see Section 6.2). For a more flexible kinetic analysis, and then (again) utilising the full PSDs, the model can be employed in a less constrained mode with independent variation of the nucleation rate and the growth rate.

A linear, temperature-independent scaling of nucleation rate and growth rate in the kinetic model can e.g. be realised by allowing the pre-exponential factors $D_{N,0}$ and $D_{G,0}$, associated with the nucleation rate (Equation (6.8))¹⁰, and the growth rate (Equation (6.9)), respectively, to vary, i.e. to deviate from the pre-exponential factor values $D_{D,0}$ determined experimentally for the diffusion coefficient of the solute component. At constant temperature, variation of the pre-exponential factors is of course equivalent to a corresponding variation of the activation energies Q_N and Q_G associated with nucleation and growth.¹¹

Especially in case of the nucleation rate, adjustment of the value assumed by the pre-exponential factor $D_{N,0}$ appears well justified in view of the only proportional relationship derived between the solute-capturing rate β^* and the rate coefficient $D_N = D_{N,0} \exp(-\frac{Q_N}{RT})$ in Equation (6.2) (cf. Section 6.2). In any case, flexibility of the model description for the nucleation rate and for the growth rate, with D_N or D_G deviating from the (impurity) diffusion coefficient D_D , is desired, because it appears likely that the diffusional mechanism involved in the nucleation process or in the growth process is not in general adequately represented by (impurity) solute diffusion in a homogeneous matrix. Allowing independent variation of nucleation and growth rates for example permits to account for an acceleration of the nucleation and growth kinetics caused by the presence of excess vacancies due to quenching from the homogenisation temperature (cf. [32, 8]), or to account, at least to some extent, for the composition dependence of the diffusion coefficient for growth which is neglected in the growth rate, Equation (6.9).

With the increased number of now three freely adaptable model parameters, either γ , $D_{N,0}$ and $D_{G,0}$, or γ , Q_N and Q_G (cases F and G, respectively,

¹⁰In case of the nucleation rate, changes in $D_{N,0}$ also affect the time lag τ (with $\exp(-\tau/t)$ varying between 0 and 1); the nucleation rate thus does not scale exactly linearly with $D_{N,0}$.

¹¹A variation of both activation energy and corresponding pre-factor is numerically undetermined at constant T .

in Table 6.2, Figure 6.5), the value assumed by the interface energy γ , by fitting the model to the PSDs determined at $T = 773$ K is now considerably larger than the value assumed by γ in the single-parameter fit (Section 6.6.1); a change of γ from 229 mJ m^{-2} to 240 mJ m^{-2} would lead to a decrease of the (initial) nucleation rate by more than factor 10. This effect is fully compensated by a strong increase of the pre-exponential factor $D_{N,0}$ (or by a decrease of the activation energy Q_N) for nucleation, which now deviates significantly from $D_{D,0}$ (or Q_D). By comparison, the value of the pre-exponential factor $N_{G,0}$ (or the activation energy Q_G) for growth remains almost unchanged; only small changes are necessary to compensate for a larger initial particle size after particle nucleation, defined by the value of the interface energy γ (Equation (6.6)).

Such large deviations in $D_{N,0}$ (or Q_N) from $D_{D,0}$ or Q_D may be considered implausible in the present case: As compared to more generally formulated models for transformation kinetics, such as obtained by the modular model approach [1, 11], the present model, as all KWN-type models, is a relatively restrictive kinetic model: The equations employed in the present model for the nucleation rate and the growth rate are derived in a very stringent way from elementary reaction steps – the movement of single solute atoms in the matrix phase (in case of nucleation, clustering of single solute atoms [5, 6]; in case of growth, long-range diffusion of single solute atoms [25]). The corresponding rate equations thus both contain an Arrhenius-type expression $D = D_0 \exp(-\frac{Q}{RT})$ which directly originates from the concerned elementary step, the movement of single solute atoms (see Equations (6.8) and (6.9)). By contrast, in the modular model, as an example for more general kinetic models, relatively abstract, (simple) rate equations for nucleation and growth, can be employed, suitable to describe the kinetic problem at hand. This constitutes the high flexibility of such general models (e.g. [89, 131, 132]).

For model application/model fitting, this has the following consequences: model descriptions based on the modular approach, as e.g. Johnson-Mehl-Avrami-Kolmogorov-like models [1, 11], have a high flexibility, but the values assumed by the kinetic parameters, such as activation energies for nucleation and growth, upon model fitting may not be interpreted straightforwardly. In the present model, by contrast, the activation energies must be somewhere close to the activation energy for diffusion of the solute component in the matrix. Largely different values for the activation energies (as in the cases F and G) therefore rather hint that the model is inapplicable, or applied in a wrong way.

Indeed, in the present case, the deviations of $D_{N,0}$ (or Q_N) from $D_{D,0}$ (or Q_D) are caused by a (factual) direct interdependence of the parameters γ and $N_{N,0}$ (or Q_N) at the specific temperature considered (i.e. the fit is undercon-

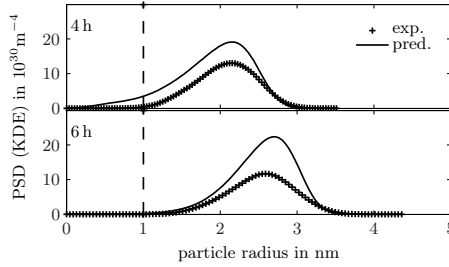


Figure 6.8: Evolution of the PSD at 760.5 K predicted on the basis of the kinetic model parameters (here γ , $D_{N,0}$ and $D_{G,0}$) determined in an underconstrained model fit of the experimental data at 773 K (case F in Table (6.2)). Although good agreement of model and experiment was achieved for the higher temperature (cf. Figure (6.5)), the thus determined model parameters are inapplicable at lower temperature, leading to vast overestimation of the number of precipitate particles.

strained; cf. Equation (6.8)). For the same values of γ and $D_{N,0}$ (or Q_N), at a different temperature, no such balancing of γ and $N_{N,0}$ (or Q_N) can occur. Consequently, usage of the model parameters, determined by fitting to the experimental data at 773 K, to predict the evolution of the PSD at another temperature, as here the intermediate annealing temperature of $T = 760.5$ K, yields considerable discrepancies of model prediction and experimental data (Figure 6.8).

Hence, to determine the kinetic parameters γ , $D_{N,0}$ (or Q_N) and $D_{G,0}$ (or Q_G) requires fitting of the kinetic model to PSDs measured at at least two different temperatures. Indeed, in this way, unique values for the parameters γ , $D_{N,0}$ (or Q_N) and $D_{G,0}$ (or Q_G) can be obtained (cases H and I in Table 6.2, Figure 6.9), which are practically identical with the corresponding values for impurity diffusion of Co in Cu.

As a matter of fact, it can be suggested that all five parameters γ , $D_{N,0}$, Q_N , $D_{G,0}$ and Q_G can be considered as fit parameters. Fitting the model with these five fit parameters simultaneously to the datasets at two temperatures, i.e. at $T = 773$ K and $T = 760.5$ K, again provides a good description of the evolution of the PSDs at both annealing temperatures (case J in Table 6.2). However, in the present case, a unique determination of all parameters was not possible: it was found that model descriptions of same quality but with largely different values for the pre-exponential factors and activation energies (but the same value for the interface energy) could be obtained (cf. case K and case J). This effect is ascribed to the small temperature difference of $\Delta T = 12.5$ K between the two experimental datasets, which does not allow to fully separate

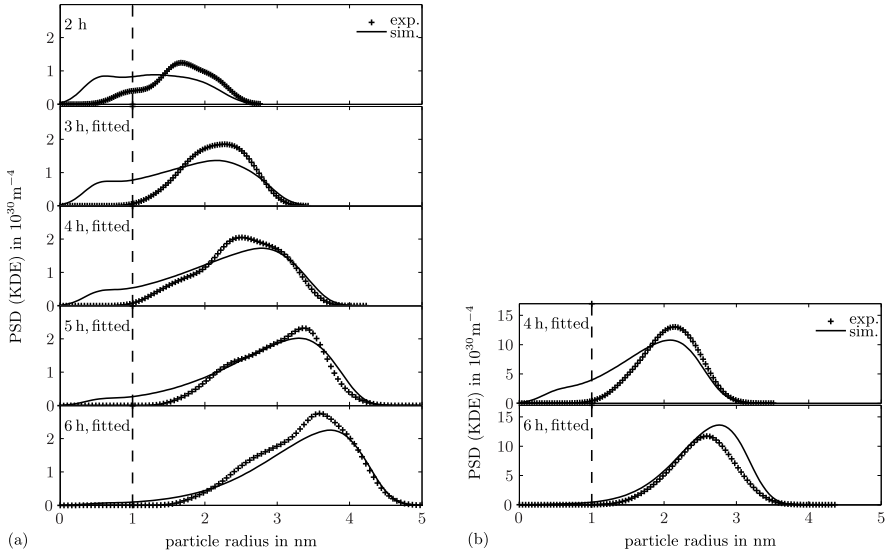


Figure 6.9: Results of fitting the kinetic model simultaneously to series of experimental PSDs at two temperatures: (a) isothermal annealing at $T = 773$ K and (b) isothermal annealing at $T = 760.5$ K, using three free model parameters, the interface energy γ and the activation energies Q_N and Q_G associated with nucleation and growth, respectively (Case H in Table (6.2)). Both datasets can be described reasonably well with one set of kinetic model parameters (compare Figure (6.8)). Employing instead of the activation energies Q_N and Q_G the pre-exponential factors $N_{N,0}$ and $N_{G,0}$ as fit parameters yields equivalent results (Case I in Table (6.2)).

the effects of changes in the activation energy and the corresponding pre-exponential factor, for both the nucleation rate and the growth rate: upon lowering the annealing temperature from $T = 773$ K to $T = 760.5$ K, the term $\exp(-Q_N/(RT))$ associated with the diffusional step for nucleation decreases by less than a factor 2 (for $D_N = D_D$). The resulting modest effect on the evolution of the PSD at the different temperatures does obviously not allow to determine independent values for the pre-exponential factors and corresponding activation energies. By contrast, strong variation of the precipitation kinetics (cf. Figure 6.3) is caused by the nucleation-barrier term $\exp(-\Delta G^*/(kT))$ of the nucleation rate, defined by the temperature-dependent chemical driving force, which increases by a factor 10 upon temperature decrease from 773 K to 760.5 K (for $\gamma = 230$ kJmol⁻¹).

Table 6.2: Results for fitting the kinetic model to experimental data for $T = 773$ K (cases A-G) and for fitting the kinetic model simultaneously to the experimental data for $T = 773$ K and $T = 760.5$ K (cases H-L). Parameter values in brackets were kept constant upon fitting, set to the values pertaining to impurity diffusion of Cu in Co [73]. γ : interface energy per unit area; Q_N , Q_G : activation energies for nucleation and growth, respectively; $D_{N,0}$, $D_{G,0}$: corresponding pre-exponential factors; ref.: error value used as reference for similar fits (cases A-L are discussed in Section 6.6).

Case	$\frac{\gamma}{\text{mJ m}^{-2}}$	$\frac{Q_N}{\text{kJ mol}^{-1}}$	$\frac{Q_G}{\text{kJ mol}^{-1}}$	$\frac{D_{N,0}}{10^{-5} \text{m}^2 \text{s}^{-1}}$	$\frac{D_{G,0}}{10^{-5} \text{m}^2 \text{s}^{-1}}$	norm. error	remark
A	229	(214)	(214)	(4.3)	(4.3)	1.0 (ref.)	
B	240	(214)	(214)	(4.3)	(4.3)	1.0	approx. $\Delta g_c(x^\alpha)$
C	253	(214)	(214)	(4.3)	(4.3)	2.3	$\Delta g_{el} = 0$
D	229	(214)	(214)	(4.3)	(4.3)	—	N_V only
E	223	(214)	(214)	(4.3)	(4.3)	—	\bar{r} only
F	240	(214)	(214)	29.8	3.7	0.7	underconstr.
G	245	195	215	(4.3)	(4.3)	0.7	underconstr.
H	229	214	214	(4.3)	(4.3)	1.0 (ref.)	
I	230	(214)	(214)	4.2	4.5	1.0	
J	230	214	199	4.5	0.42	1.0	underconstr.
K	229	184	244	0.041	455	1.0	underconstr.
L	259	209	215	(4.3)	(4.3)	0.7	$\Delta g_{el} = 0$

It can be concluded that, although the present experimental data do not comprise sufficient temperature variation to determine the five potential fit parameters considered in a unique way, the present experimental data in the form of the PSD evolution at different temperatures do contain sufficient information to determine unique values for at least either the activation energies or the pre-exponential factors independently, in addition to the interface energy. The excellent agreement of the values obtained for Q_N and Q_G , or $D_{N,0}$ and $D_{G,0}$, with literature data for impurity diffusion of Co in Cu indicates that the diffusional processes involved in nucleation and growth in the present case are indeed of a nature very similar to that of volume diffusion, in an undisturbed matrix of homogeneous composition. The value of $\gamma \approx 230 \text{ mJ m}^{-2}$ finally assumed by the interface energy (cases H and I) agrees well with the range of interface-energy values reported in literature (e.g. [130, 39, 124], cf. comments in Section 6.6.2).

The good agreement of experiment and model may be ascribed on the one hand to the chosen experimental conditions of low supersaturation and determination of the PSDs in coarse-grained specimens of low defect density, providing conditions as ideal as possible for homogeneous nucleation to occur in a crystalline solid solution, and on the other hand to the model properties of the Cu-Co system: the small mutual solubility of Cu and Co, allowing to investigate precipitation reactions in a very dilute system, and the formation of initially fully coherent spherical precipitates due to the relatively small lattice mismatch between fcc Cu and fcc Co.

Finally, repeating the model fit as above with γ , Q_N and Q_G as freely adaptable parameters, but with the elastic energy contribution Δg_{el} set to zero (similar to case C in Section 6.6.2), yields considerably different values not only for the interface energy (cf. case C), but also for the activation energy Q_N for nucleation (case L in Table 6.2). This clearly indicates that in order to describe the precipitation kinetics in Cu-Co in a physically reasonable way, the elastic misfit energy must be incorporated into the kinetic model, for both nucleation and growth (which contrasts with previous works; see e.g. [96, 124, 60, 125]). This is now greatly facilitated by use of the inverse evaluation method, for the first time applied to experimental data in this study.

6.6.5 Predictive capability; limitations

Knowledge of the kinetic model parameters, obtained either from fitting the kinetic model to experimental data or from adequate literature data, should in principle allow to predict the evolution of the particle-size distribution for arbitrary annealing times and temperatures. To test the predictive capability of the kinetic model when employing the kinetic parameters determined

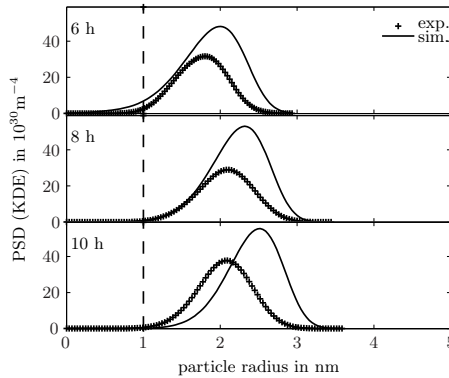


Figure 6.10: The evolution of the PSD at the lowest annealing temperature $T = 748$ K. Markers: Experimental data. Solid lines: Prediction on the basis of the kinetic model parameters determined by fitting the model simultaneously to the experimental data at two higher temperatures (case J in Table (6.2)). The predicted PSDs largely overestimate the total number of particles and suggest a faster evolution of the PSD towards larger particle sizes.

above by fitting the model to the PSDs at two temperatures ($T = 773$ K and $T = 760.5$ K, cases H and I in Table 6.2), the thus far ignored experimental dataset for the evolution of the particle-size distribution at the lowest annealing temperature $T = 748$ K, featuring the highest values of particle-number density and volume fraction of precipitates (Figures 6.3 and 6.4), can be compared against the predictions of the kinetic model: Despite the generally good agreement between model and experiment achieved upon fitting the kinetic model to the experimental data at the higher temperatures, considerable discrepancies can be observed comparing model prediction and experiment at $T = 748$ K (Figure 6.10): The model predicts a much higher particle-number density and a more dynamic evolution of the particle-size distribution towards larger particle size. The quality of the experimental data for 748 K is comparable to the two datasets employed to determine the kinetic parameters. Also, large changes in the kinetic parameters appear improbable in view of the small temperature range of 25 K covered in this study.¹²

It can thus be suggested that the kinetic model is incapable to describe the evolution of the PSD at the high degree of solute depletion as realised at the lowest annealing temperature. Disagreement between KWN-type model

¹²Indeed, even with the full flexibility of the kinetic model provided by three fit parameters, it was not possible to achieve a model description for the experimental data at $T = 748$ K of a quality similar to that achieved at the higher temperatures.

prediction and experiment was observed before for later stages of the precipitation reaction within the late growth-coarsening regime (e.g. [133,98]). In these cases, better agreement was achieved by adopting an interface energy increasing with particle size. At least in the present case, this approach does not appear reasonable, since the experimental series at all three annealing temperatures feature comparable particle sizes. Recognising that the discrepancies of the model with the experiments appear mainly for high volume fractions of particles, i.e. high degrees of solute depletion of the matrix, these discrepancies may rather be considered as an artifact owing to application of the mean-field approach for the matrix composition: the mean-field approach only considers individual interaction of a particle (class) with a matrix of average composition and cannot account for direct particle-particle interaction via their surrounding diffusion fields (note that the mean composition approach also inherently clashes with the growth rate equation (6.9) which is derived assuming a *linear concentration gradient* in the matrix).

In addition to particle-particle interaction via diffusion fields, in the present case of coherent Co-rich particles exhibiting a volume mismatch with the matrix, particle-particle interaction also occurs via interaction of the elastic strain fields surrounding each particle. Assessment of the effects of strain-field interaction is complex; such interaction may either (locally) promote or inhibit nucleation and growth of particles. The effect of strain-field interaction was suggested to lead to chain-like arrays of Co-rich precipitate particles along elastically soft directions of the Cu-rich matrix as observed for Cu-Co, albeit for alloys of considerably higher solute content featuring much high particle-number densities (10^{23} m^{-3} to 10^{25} m^{-3}) [41,134]. In view of the decline of elastic strain proportional to $(r/(r+d))^3$ with distance d from the particle-matrix interface [3], the effect of strain-field interaction may in first approximation be neglected for the relatively small volume fractions of precipitates and low particle-number densities observed in the present case.

It can be concluded that in the first stage of nucleation and growth, at low degrees of solute depletion, deficiency of the mean field approach to describe the solute depletion has an only small effect on the kinetics of nucleation and growth, leading to good agreement between kinetic model and experiment, as indeed observed especially for the dataset determined at the highest annealing temperature of 773 K. In late stages with higher volume fractions of precipitates, as holds for the dataset at 748 K, the mean-field approach appears inadequate to correctly account for direct particle-particle interactions via their surrounding diffusion fields, thus demanding the spatial distribution of precipitates in the matrix and their interactions to be explicitly expressed in the kinetic model.

6.7 Conclusions

A kinetic model for precipitation reactions, on the basis of the recently proposed “inverse evaluation method” which allows inherently consistent, accurate and computationally efficient evaluation of the thermodynamics for nucleation and growth, was presented and applied to experimental data for the particle-size distributions (PSDs) evolving as function of time in a dilute Cu-Co alloy at different isothermal annealing temperatures.

- Good agreement of kinetic model and experimental data was obtained for the early stages of nucleation and growth. In later stages of the precipitation reaction, differences emerged as a consequence of a breakdown of the mean-field approach to describe the solute depletion of the matrix.
- It was shown that if experimental data for the evolution of the PSDs at at least two different temperature is available, unique, physically reasonable values for the interface energy and for the activation energies of nucleation and growth, or for the corresponding pre-exponential factors (and potentially for both activation energies and both pre-exponential factors), can be determined by fitting the kinetic model simultaneously to the experimental datasets at different temperatures. Such a modelling approach is especially helpful when the diffusional mechanisms involved in the nucleation and growth process deviate from impurity diffusion of the solute component in the matrix phase.
- Incorporation of the elastic misfit energy contribution, for *both* nucleation and growth, was found to be mandatory to achieve good agreement of model and experiment and to obtain physically reasonable values for the kinetic model parameters.

Acknowledgements

The Stuttgart Center for Electron Microscopy, Max Planck Institute for Intelligent Systems, Stuttgart, is gratefully acknowledged for access to TEM facilities. Dr. T. Bublat, formerly Max Planck Institute for Intelligent Systems, Stuttgart, is acknowledged for performing magnetisation measurements. One of the authors, BR, would like to thank Dr. E.A. Jäggle, Max Planck Institute for Iron Research, Düsseldorf, for many fruitful discussions.

Chapter 7

Summary

7.1 Summary in the English language

In this thesis, the kinetics of heterogeneous solid-state phase transformations in different prototype experimental systems are investigated with emphasis on the development of new strategies for kinetic modelling using mean-field kinetic models.

Based on the assumption of certain transformation mechanisms (usually the *nucleation* and *growth* of product-phase particles), mean-field kinetic models describe the evolution of chosen (experimentally accessible) parameters as function of time and generally also of temperature, e.g. the evolution of the transformed volume fraction, of average particle size and number density, or of the size distribution of particles. In the framework of this thesis, two different types of mean-field kinetic models are employed: a general modular modelling approach for phase transformation kinetics [11] and a KWN-(Kampmann-Wagner-Numerical)-type [15] multi-class model specialised on the description of precipitation kinetics in dilute supersaturated systems.

The modular model, a generalisation of the classical JMAK-(Johnson-Mehl-Avrami-Kolomogorov)-model [12–14], provides a flexible framework for modelling the evolution of the transformed volume fraction $f(t)$, allowing to combine various different kinetic expressions for particle nucleation and particle growth which can range from very general, abstract expressions (e.g. Arrhenius-type rate equations; see, e.g., [13]) to highly case-specific ones. However, kinetic analysis on the basis of only the transformed fraction does often not allow to separately determine the kinetics of nucleation and of growth: For example in case of the classical JMAK-equation, a special case within the modular model approach, the kinetic model only provides a description of the phase transformation kinetics in terms of effective, overall kinetic parameters, e.g. an effective activation energy for the transformation. Such a model description does not convey individual information on the kinetics of particle nucleation and particle growth and hence does not allow to predict the number and size of the product particles. In this thesis, different strategies to arrive at separate kinetic descriptions for nucleation and growth applying the modular model approach are presented (Chapters 2 to 4).

In KWN-type multi-class models, the evolution of the size distribution of product particles upon precipitation of solute-rich particles from a supersaturated matrix phase is modelled for discrete time steps and for discrete particle size classes. The kinetic descriptions for the mechanisms of nucleation and growth are based on classical nucleation theory [5,6] and growth of solute-rich particles controlled by volume diffusion of the solute components [25,26], respectively. Both descriptions involve an evaluation of the thermodynamics of the system: The nucleation rate is a function of the nucleation barrier ΔG^* , which depends on the chemical driving force and thus on the composition of parent matrix and precipitate particle, and the particle growth rate includes a consideration of the Gibbs-Thomson effect, i.e. the (equilibrium) composition of particle and matrix at the particle-matrix interface are functions of the particle size. In the framework of this thesis, the coupling of KWN-type kinetic models to the thermodynamics of the system is addressed and the relation between the kinetic model description and the the quality and quantity of the available experimental data is analysed (Chapters 5 and 6).

In **Chapter 2**, the kinetics of the precipitation reaction in a quenched, highly supersaturated Cu-1 at.% Co alloy upon isochronal heating are investigated using power-compensating differential scanning calorimetry (DSC). Employing the modular model, the evolution of the volume fraction of precipitates can be described well in a JMAK-type mode with kinetic rate equations of Arrhenius-type, yielding an overall, effective activation energy of $Q_{\text{eff}} = (133 \pm 8) \text{ kJmol}^{-1}$.

In order to obtain separate kinetic descriptions for particle nucleation and particle growth, quantitative information on the microstructure – the number density of precipitate particles as determined with transmission electron microscopy (TEM) at the end of the precipitation reaction (part) as observed with DSC – is directly implemented into the kinetic model fit (Figure 7.1). This additional information allows to separate the effective activation energy into an activation energy for the particle nucleation mechanism of $Q_{\text{N}} = 50 \text{ kJmol}^{-1}$ and an activation energy for the particle growth mechanism of $Q_{\text{G}} = 177 \text{ kJmol}^{-1}$. Thus, by incorporation of additional information on the microstructure into the modular model approach, a full characterisation of particle nucleation kinetics and particle growth kinetics is possible.

Remark on Chapter 2: The values of both Q_{N} and Q_{G} determined in this study are considerably smaller than the activation energy for (impurity) diffusion of Co in fcc Cu with $Q_{\text{D}} = 214 \text{ kJmol}^{-1}$ [73], a value which was also determined for the activation energies of nucleation and growth using a KWN-type model for analysis of the precipitation kinetics in dilute Cu-Co upon isothermal annealing (in Chapter 6 of this thesis). In the study as presented in Chapter 2, the comparatively small values of Q_{N} and Q_{G} are attributed to

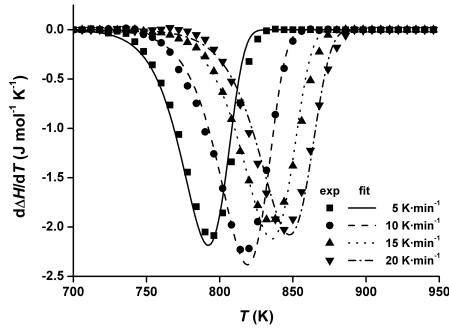


Figure 7.1: Precipitation of Co-rich particles from supersaturated Cu-0.95 at.% Co upon isochronal heating (Chapter 2): The rate of heat release determined by DSC for different heating rates (symbols), normalised on the heating rate and proportional to the transformation rate, and the model description (lines), obtained by fitting the modular model to the experimental data under the additional constraint that the experimentally determined particle number density is reproduced. This modelling approach allows to derive separate kinetic descriptions for nucleation and growth.

the presence of quenched-in excess vacancies, accelerating the diffusion-carried precipitation process. However, it may also be possible that the assumption of simple, Arrhenius-type rate equations over-simplifies the physical background of the precipitation kinetics. In this case, the kinetic model only provides a good mathematical description of the experimentally observed precipitation kinetics (which may be sufficient for practical applications), but does not provide deeper insight into the physical processes of the precipitation reaction, e.g. does not allow to relate the activation energies of the mechanisms of nucleation and growth to an elemental underlying physical process such as volume diffusion of Co in fcc Cu.¹

In **Chapter 3**, the crystallisation kinetics of amorphous Fe₄₀Ni₄₀B₂₀ upon isothermal annealing are investigated, again applying DSC, supported by X-ray diffraction (XRD) analysis and TEM. XRD and TEM indicate that upon crystallisation of amorphous Fe₄₀Ni₄₀B₂₀, grains with lamellar microstructure are formed by coupled growth of two crystalline phases, an fcc (Fe,Ni)-phase and an orthorhombic (Fe,Ni)₃B-phase. The experimental data, the evolution of the transformed fraction at different isothermal annealing temperatures, can

¹In this context, a re-evaluation of the experimental data on the basis of the KWN-type kinetic model employed in Chapter 2 could be of interest, but may actually be thwarted by the use of the classical nucleation theory in this type of model, which loses its theoretical justification for high driving forces [43], as are indeed present upon isochronal heating of quenched, supersaturated alloys.

again be described well in the framework of the modular model in terms of only effective kinetic model parameters. To achieve a separate description of the nucleation kinetics and growth kinetics, in this case additional experimental information is produced by artificially altering the experimental crystallisation kinetic via a pre-annealing treatment at lower temperatures: This additional treatment step is intended to lead to the generation of a certain number of nuclei already present at the beginning of the main annealing step, which then contribute to the transformation only by particle growth [21]. By fitting the modular model with a combination of two nucleation modes, a continuous nucleation rate and a certain number of pre-existing nuclei, simultaneously to both datasets, again separate kinetic model parameters for nucleation and for growth can be determined (Figure 7.2). In addition, varying values for the effective kinetic parameters reported in studies of the crystallisation kinetics of $\text{Fe}_{40}\text{Ni}_{40}\text{B}_{20}$ based on the classical JMAK approach can thus be explained by varying contributions of pre-existing nuclei, for instance owing to an insufficient specimen preparation process.

In **Chapter 4**, a review of the modelling strategies presented in Chapter 2 and Chapter 3 for separating the contributions of nucleation and growth within the modular approach is given, extended by an example of the modular model serving as a flexible framework for dedicated, case-specific kinetic expressions for nucleation kinetics and growth kinetics [44].

In **Chapter 5**, the coupling of KWN-type models for precipitation kinetics to the thermodynamics of the system is analysed: The thermodynamic concepts employed in this type of model, the nucleation barrier and the Gibbs-Thomson effect, originate from the same thermodynamic consideration – the equilibrium in a particle-matrix system associated with a certain particle-matrix interface energy (as first discussed by Gibbs in [4]). However, in KWN-type kinetic models, this connection is most frequently ignored and unnecessarily complicated and numerically costly (see, e.g., [104,105,99]) and/or thermodynamically inconsistent (see, e.g., [15,96,109]) treatments for nucleation barrier and Gibbs-Thomson effect are applied, which can lead to inadvertent, artificial enhancement or attenuation of either nucleation kinetics or growth kinetics. Therefore, it is first shown how typically used concepts for nucleation barrier and Gibbs-Thomson effect can be retraced to the same consideration of thermodynamic equilibrium. On this basis, an approach for inherently consistent evaluation of nucleation barrier and Gibbs-Thomson effect is formulated. For typical approximations introduced upon kinetic modelling of precipitation reactions (composition-independent contributions of interface energy and elastic misfit energy), a numerically highly efficient method for introducing thermodynamic data, as e.g. derived from a CALPHAD assessment of the alloy system, into the kinetic model is presented.

In **Chapter 6**, the thermodynamic evaluation method presented in Chapter 5 is implemented into a KWN-type kinetic model for precipitation kinetics. This kinetic model is applied to experimental data for the evolution of the PSD in a Cu-0.6 at.% Co upon isothermal annealing at different temperatures, determined using TEM (Figure 7.3). The usage of an accurate thermodynamic description, especially a consideration of the elastic misfit energy which has been omitted in almost all kinetic studies of the precipitation reaction in Cu-Co, is found to be mandatory to achieve a good agreement of model description and experiment. By fitting the kinetic model simultaneously to PSD data determined at different temperatures, separate values for the activation energies of nucleation and growth (or for the corresponding pre-exponential factors) are obtained which are identical with the value of the activation energy for impurity diffusion of Co in fcc Cu (or with the value of the corresponding pre-exponential factor). If applied to experimental data for the evolution of the PSDs at different temperatures, the kinetic model developed in this study, incorporating the thermodynamic evaluation method presented in Chapter 5, thus allows to derive physically plausible values for the activation energies of the nucleation mechanism and the growth mechanism which can be directly related to the underlying elemental reaction mechanism, the volume diffusion of solute atoms.

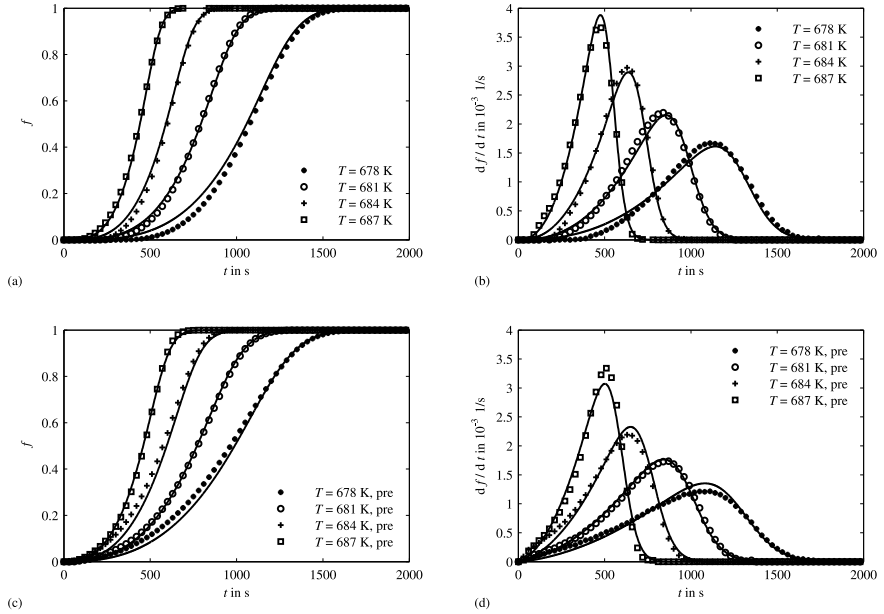


Figure 7.2: Crystallisation of amorphous $\text{Fe}_{40}\text{Ni}_{40}\text{B}_{20}$ upon isothermal annealing (Chapter 3): transformed fraction curves and transformation-rate curves for annealing without pre-annealing treatment ((a) and (b)) and after application of a pre-annealing treatment at $T_{\text{pre}} = 658$ K for 1200 s ((c) and (d)). Markers: experimental data; solid lines: model fit. The modular model is fitted simultaneously to all transformation-rate curves of both experimental datasets, only allowing the relative contributions of continuous nucleation and pre-existing nuclei to differ for the two datasets. This method again allows to determine separate kinetic descriptions for nucleation and growth.

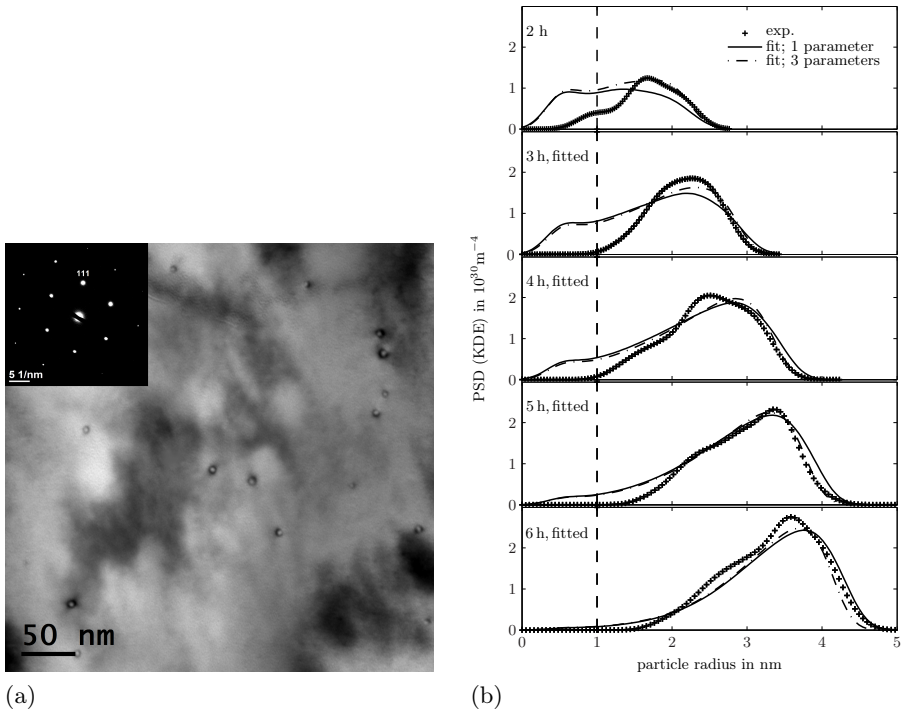


Figure 7.3: Precipitation of Co-rich particles from supersaturated Cu-0.6 at.% Co upon isothermal annealing (Chapter 6): (a) TEM image after annealing at 773 K for 4 h, recorded under bright-field zone-axis conditions (fcc Cu $\langle 111 \rangle$ electron beam incidence; see diffraction pattern in the inset). A number of particles with radii of about 1.5 nm to 3 nm is visible. (b) The evolution of the particle size distribution at 773 K as function of annealing time (PSDs represented by kernel density estimates). Markers: experimental PSDs. Solid lines and dash-dotted lines: model fits (using one or three fit parameters; for further information on the different fitting approaches see Chapter 6, Cases A and F). Dashed vertical lines: lower limit of the fitting range, accounting for the experimental detection limit which lies at around 1 nm [38]. Especially for longer annealing times, leading to larger particle sizes well above the experimental detection limit, good agreement between modelled and experimental PSDs can be achieved.

7.2 Zusammenfassung in deutscher Sprache

Diese Arbeit befasst sich mit der Untersuchung der Kinetik heterogener Festkörperphasenumwandlungen in verschiedenen experimentellen Modellsystemen; ihr Schwerpunkt liegt dabei auf der Entwicklung neuer Strategien für kinetische Modellierungen mittels kinetischer *mean-field*-Modelle.

Basierend auf der Annahme bestimmter Umwandlungsmechanismen (üblicherweise *Keimbildung* und *Wachstum* von Teilchen der Produktphase(n)), bieten kinetische *mean-field*-Modelle eine Beschreibung ausgewählter (experimentell zugänglicher) Parameter als Funktion der Zeit und (in der Regel) der Temperatur, zum Beispiel eine Beschreibung des zeitlichen Verlaufs des umgewandelten Volumenanteils, der mittleren Teilchengröße und der Teilchendichte, oder der Größenverteilung der Teilchen. Im Rahmen dieser Arbeit finden zwei unterschiedliche Arten von *mean-field*-Modellen Anwendung: ein allgemeiner, modularer Modellansatz zur Beschreibung der Umwandlungskinetik [11] und ein Multiklassen-Modell basierend auf dem KWN-(Kampmann-Wagner-Numerical)-Ansatz [15], zugeschnitten auf die Beschreibung der Ausscheidungskinetik in verdünnten übersättigten Systemen.

Der modulare Modellansatz stellt eine Verallgemeinerung des klassischen JMAK-(Johnson-Mehl-Avrami-Kolomogorov)-Modells [12–14] für den umgewandelten Volumenanteil $f(t)$ dar und ermöglicht die Kombination verschiedenster kinetischer Beschreibungen für Keimbildung und Wachstum, ausgehend von sehr allgemein gehaltenen Ausdrücken (z.B. Arrhenius-artigen Rategleichungen; vgl. [13]) bis hin zu fallspezifischen kinetischen Modellen für Keimbildung und Wachstum. Der modulare Modellansatz bietet somit einen höchst anpassungsfähigen Rahmen zur Modellierung des umgewandelten Volumenanteils $f(t)$. Ein Nachteil der Beschreibung der Umwandlungskinetik allein auf Basis des umgewandelten Volumenanteils liegt jedoch darin, dass eine getrennte Betrachtung der Beiträge von Keimbildung und Wachstum oftmals nicht möglich ist. Als Beispiel dafür kann die klassische JMAK-Gleichung (ein spezieller Fall innerhalb des modularen Modellansatzes) herangezogen werden, mit welcher sich die Umwandlungskinetik allein mittels effektiver, mittlerer Modellparameter, z.B. mittels einer effektiven Aktivierungsenergie Q_{eff} , beschreiben lässt. Diese Art der Beschreibung beinhaltet keine gesonderte Information bezüglich der Keimbildungskinetik und der Wachstumskinetik und lässt daher keine Vorhersagen über Anzahl und Größe der gebildeten Teilchen zu. In dieser Arbeit werden unterschiedliche Strategien im Rahmen des modularen Ansatzes vorgestellt, welche eine separate Beschreibung der Keimbildungskinetik und der Wachstumskinetik ermöglichen (Kapitel 2 bis 4).

Multiklassen-Modelle auf Basis des KWN-Ansatzes bieten eine Beschreibung der zeitlichen Entwicklung der Teilchengrößenverteilung von Ausschei-

dungen aus einer übersättigten Matrixphase, welche für diskrete Zeitschritte und Größenklassen modelliert wird. Zur Beschreibung der Keimbildungskinetik wird die klassische Keimbildungstheorie [5, 6] verwendet (bisweilen in abgewandelter Form). Die Beschreibung der Wachstumskinetik erfolgt unter der Annahme, dass das Wachstum der Ausscheidung durch Volumendiffusion der gelösten Komponente(n) zur Ausscheidung hin kontrolliert wird [25, 26]. Die kinetische Beschreibung beider Mechanismen beinhaltet eine Auswertung der thermodynamischen Eigenschaften des Systems: Die Keimbildungsrate ist eine Funktion der Keimbildungsbarriere ΔG^* , welche selbst von der chemischen Triebkraft und somit von der chemischen Zusammensetzung von Matrix und Ausscheidung abhängt. Die Beschreibung der Wachstumsrate wiederum berücksichtigt den Gibbs-Thomson-Effekt, d.h. die (Gleichgewichts-) Zusammensetzung der Ausscheidungsphase und der Matrixphase an der Grenzfläche zwischen Teilchen und Matrix ist abhängig von der Teilchengröße. Im Rahmen dieser Arbeit wird die Verknüpfung von kinetischen Modellen basierend auf dem KWN-Ansatz mit der thermodynamischen Beschreibung des Systems, sowie die Beziehung zwischen dem kinetischen Modell und der Quantität und Qualität der experimentellen Datengrundlage untersucht (Kapitel 5 und 6).

Kapitel 2 beinhaltet die Untersuchung der Bildungskinetik Co-reicher Ausscheidungen in einer abgeschreckten und stark übersättigten Cu-1 at.% Co-Legierung mittels leistungskompensierender dynamischer Differenzkalorimetrie (DSC) für unterschiedliche konstante Aufheizraten. Im Rahmen des modularen Modellansatzes lässt sich die Entwicklung des ausgeschiedenen Anteils $f(T(t))$ mittels einer JMAK-artigen Modellformulierung auf Basis von Arrhenius-artiger Reaktionsraten beschreiben, wobei sich eine effektive Aktivierungsenergie von $Q_{\text{eff}} = (133 \pm 8) \text{ kJmol}^{-1}$ ergibt.

Um eine separate Beschreibung der Keimbildung und des Wachstums zu erzielen, werden zusätzlich zum experimentellen Verlauf von $f(T(t))$ quantitative Daten zur Entwicklung der Mikrostruktur, hier die mit Hilfe von Transmissionselektronenmikroskopie (TEM) bestimmte Teilchendichte nach Ende der mittels DSC beobachteten Reaktion, in die numerische Anpassung des kinetischen Modells integriert (Abbildung 7.4). Diese zusätzliche Information ermöglicht es, die effektive Aktivierungsenergie in ihre einzelnen Bestandteile, die Aktivierungsenergie des Keimbildungsmechanismus mit $Q_{\text{N}} = 50 \text{ kJmol}^{-1}$ und die Aktivierungsenergie des Wachstumsmechanismus mit $Q_{\text{G}} = 177 \text{ kJmol}^{-1}$, zu zerlegen. Die Integration zusätzlicher Information zur Mikrostruktur-Entwicklung in den modularen Modellansatz ermöglicht es somit, die Kinetik der Keimbildung und des Wachstums separat zu charakterisieren.

Anmerkung zu Kapitel 2: Die Werte für Q_{N} und Q_{G} , die in dieser Studie bestimmt wurden, sind erheblich kleiner als der Wert der Aktivierungsenergie

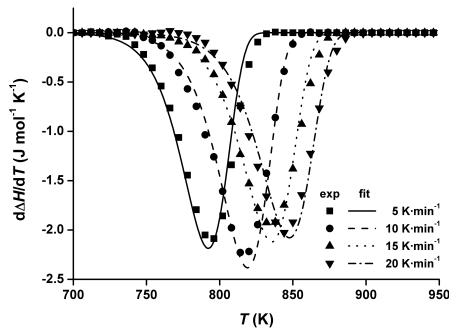


Abbildung 7.4: Ausscheidung Co-reicher Teilchen in einer übersättigten Cu-0.95 at.% Co-Legierung unter Aufheizen mit konstanter Heizrate (Kapitel 2). Symbole: die mittels DSC gemessene Raten der Wärmefreisetzung, normalisiert auf die Heizrate (und proportional zur Umwandlungsrate). Linien: die sich aus numerischer Anpassung des modularen Modells an die experimentellen Kurven ergebenden Raten unter der zusätzlichen Bedingung, dass auch die experimentell bestimmte Teilchendichte korrekt wiedergegeben wird. Diese Art von Modellanpassung erlaubt die separate Bestimmung sowohl der Keimbildungskinetik als auch der Wachstumskinetik.

für die Diffusion von Co in fcc Cu, welche bei $Q_D = 214 \text{ kJ mol}^{-1}$ (bei unendlicher Verdünnung von Co, [73]) liegt. Im Rahmen der in Kapitel 6 präsentierten Untersuchung der isothermer Ausscheidungskinetik in Cu-Co wurden, unter Anwendung eines KWN-artigen Modells, Werte für Aktivierungsenergien von Keimbildung und Wachstum erzielt, die genau dem Wert der Aktivierungsenergie für die Diffusion von Co in fcc Cu entsprechen. In der in Kapitel 2 vorgestellten Untersuchung wurden die vergleichsweise kleinen Werte von Q_N und Q_G auf die Anwesenheit von Überschussleerstellen, resultierend aus der raschen Abschreckung der Proben zur Einstellung des übersättigten Zustands, zurückgeführt, welche zu einer Beschleunigung des diffusionsgetragenen Ausscheidungsprozesses führen sollten. Es ist allerdings ebenfalls denkbar, dass durch die Annahme von Arrhenius-artigen Reaktionsraten die physikalischen Hintergründe der Ausscheidungsreaktion zu stark vereinfacht werden. In diesem Fall stellt die Modellbeschreibung nur eine mathematisch gute Beschreibung der experimentell beobachteten Ausscheidungskinetik dar (was für praktische Anwendungen durchaus ausreichen mag), ermöglicht jedoch keinen tieferen Einblick in die physikalischen Prozesse der Ausscheidungsreaktion; die Aktivierungsenergien Q_N und Q_G der angenommenen Keimbildungs- und Wachstumsmechanismen hätten demzufolge keinen Bezug zur einem grundlegenden physikalischen Prozess wie der der Volumendiffusion von Co in fcc

Cu.²

In **Kapitel 3** wird die Kinetik der Kristallisation einer amorphen $\text{Fe}_{40}\text{Ni}_{40}\text{B}_{20}$ -Legierung bei isothermer Auslagerung untersucht, wiederum mittels DSC und ergänzt durch Röntgenbeugung (XRD) und TEM. Letztere zeigen, dass bei der Kristallisation Körner mit lamellarer Mikrostruktur gebildet werden, welche durch gekoppeltes Wachstum der beteiligten kristallinen Produktphasen, einer (Fe,Ni)-Phase mit fcc-Struktur und einer orthorhombischen $(\text{Fe,Ni})_3\text{B}$ -Phase, entsteht.

Die zeitliche Entwicklung des experimentell bestimmten umgewandelten Volumenanteils bei unterschiedlichen Auslagerungstemperaturen lässt sich auch hier wieder im Rahmen des modularen Modellansatzes allein mittels effektiver Modellparameter beschreiben. Um eine separate kinetische Beschreibung der Keimbildung und des Wachstums zu realisieren, wird in diesem Fall die experimentelle Datengrundlage durch eine künstlich erzeugte Änderung der Umwandlungskinetik vergrößert: Durch eine vorhergehende Auslagerung der Proben bei einer niedrigeren Auslagerungstemperatur soll vorab eine gewisse Anzahl von Keimen generiert werden, die während des eigentlichen Auslagerungsschrittes nur durch Wachstum zur Umwandlungskinetik beiträgt [21]. Die gleichzeitige Anpassung des modularen Modells an beide Datensätze mit einer Kombination zweier Keimbildungsmechanismen – teils kontinuierliche Keimbildung, teils bereits existierende Keime – ermöglicht wieder die Bestimmung separater Modellparameter für Keimbildung und Wachstum (Abbildung 7.5). Zudem kann hiermit die Menge an unterschiedlichen Werten für die effektiven kinetischen Parameter, welche in der Literatur in Studien der $\text{Fe}_{40}\text{Ni}_{40}\text{B}_{20}$ -Kristallisationskinetik basierend auf der klassischen JMAK-Gleichung angegeben werden, durch jeweils variierende Anteile von bereits vorliegender Keime, z.B. verursacht durch eine unzulängliche Probenherstellung, erklärt werden.

Kapitel 4 bietet einen Überblick zu den beiden in Kapitel 2 und Kapitel 3 vorgestellten Methoden zur Separierung der Beiträge von Keimbildung und Wachstum innerhalb des modularen Ansatzes. Zusätzlich wird ein Beispiel vorgestellt, in welchem der modulare Modellansatz als flexibler Rahmen für spezifische kinetische Modelle für Keimbildung und Wachstum dient [44].

In **Kapitel 5** wird die Verknüpfung von Modellen für die Ausscheidungskinetik basierend auf dem KWN-Ansatz mit der thermodynamischen Beschreibung des Systems näher untersucht: Die thermodynamischen Konzepte

²In dieser Hinsicht könnte eine erneute Auswertung der experimentellen Daten auf Basis des KWN-artigen Modells aus Kapitel 6 von Interesse sein. Dessen Anwendbarkeit ist jedoch durch die Verwendung der klassischen Keimbildungstheorie eingeschränkt, welche für große Triebkräfte bzw. hohe Übersättigungen, wie sie beim Aufheizen abgeschreckter Proben zwangsläufig vorliegen, ihre theoretische Grundlage verliert [43].

Keimbildungsbarriere und Gibbs-Thomson-Effekt, welche in dieser Art von Modell Anwendung finden, basieren beide auf der gleichen thermodynamischen Grundlage – der Betrachtung des thermodynamischen Gleichgewichts im System Teilchen-Matrix, assoziiert mit einer gewissen Exzess-Energie der Teilchen-Matrix-Grenzfläche (wie bereits von Gibbs in [4] diskutiert). In kinetischen Modellen des KWN-Typs wird dieser Zusammenhang zwischen Keimbildungsbarriere und Gibbs-Thomson-Effekt jedoch meist ignoriert und die thermodynamischen Auswertung erfolgt mittels unnötig komplizierter und numerisch aufwändiger (siehe z.B. [104, 105, 99]) und/oder inkonsistenter (siehe z.B. [15, 96, 109]) Verfahren, wobei letztere zu einer unbeabsichtigten, künstlichen Verstärkung oder Abschwächung der Keimbildungskinetik oder der Wachstumskinetik führen. Es wird daher zunächst gezeigt, wie häufig angewandte Konzepte für eine getrennte Auswertung von Keimbildungsbarriere und Gibbs-Thomson-Effekt auf ein und dieselbe thermodynamische Gleichgewichtsbetrachtung zurückgeführt werden können. Auf dieser Basis wird ein Ansatz für eine inhärent konsistente Auswertung von Keimbildungsbarriere und Gibbs-Thomson-Effekt formuliert. Für häufig getroffene vereinfachende Annahmen (zusammensetzungsunabhängige Beiträge der Grenzflächenenergie und der elastischen Fehlpassungsenergie), wird eine Methode vorgestellt, mittels welcher numerische Daten für die thermodynamischen Eigenschaften, z.B. basierend auf einer CALPHAD-Beschreibung des Legierungssystems, auf konsistente Weise und numerisch effizient in das kinetische Modell integriert werden können.

In **Kapitel 6** wird die in Kapitel 5 vorgestellte Methode in ein kinetisches Modell auf Basis des KWN-Ansatzes integriert, welches zur Beschreibung der experimentell bestimmten Entwicklung der Teilchengrößenverteilung in Cu-0.6 at.% Co bei verschiedenen Auslagerungstemperaturen herangezogen wird (Abbildung 7.6). Es wird gezeigt, dass die Verwendung einer akkuraten thermodynamischen Beschreibung, insbesondere unter Berücksichtigung der für das System Cu-Co meist vernachlässigten elastischen Fehlpassungsenergie, in diesem Fall zwingend notwendig ist um eine gute Übereinstimmung von Modell und Experiment zu erreichen. Durch Anpassen des kinetischen Modells an Teilchengrößenverteilungen bestimmt für unterschiedliche Auslagerungstemperaturen lassen sich (unabhängige) Werte für die Aktivierungsenergien von Keimbildung und Wachstum (oder für die entsprechenden prä-exponentiellen Faktoren) bestimmen, welche identisch sind mit dem Wert der Aktivierungsenergie für die Diffusion von Co in fcc Cu (bzw. dem Wert des prä-exponentiellen Faktors). Angewandt auf Teilchengrößenverteilungen bestimmt für unterschiedliche Temperaturen, ermöglicht das in dieser Studie entwickelte Modell auf Basis der thermodynamischen Auswertemethode aus Kapitel 5 somit die Bestimmung physikalisch plausibler Werte für Aktivierungsenergien

von Keimbildung und Wachstum, welche einen direkten Bezug der angenommenen Keimbildungs- und Wachstumsmechanismen auf den zugrundeliegenden elementaren Reaktionsmechanismus, die Volumendiffusion von Atomen der gelösten Komponente, zulassen.

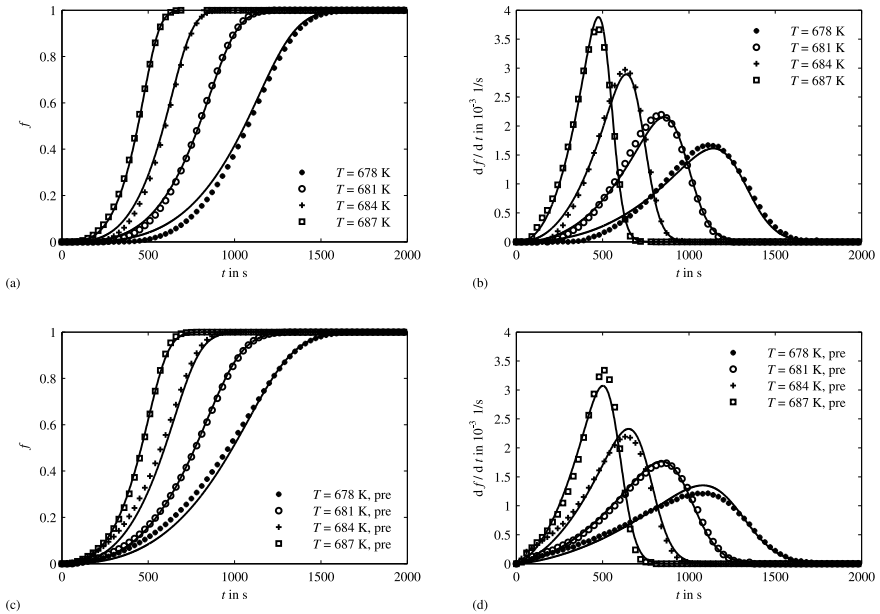


Abbildung 7.5: Kristallisation einer amorphen $\text{Fe}_{40}\text{Ni}_{40}\text{B}_{20}$ -Legierung bei isothermer Auslagerung (Kapitel 3): umgewandelter Anteil und Umwandlungsrate bei Auslagerung ohne vorhergehenden Auslagerungsschritt bei niedrigeren Temperaturen ((a) und (b)) und nach einer Vorauslagerung bei $T_{\text{pre}} = 658 \text{ K}$ für 1200 s ((c) und (d)). Symbole: experimentelle Daten; Linien: Ergebnisse der gleichzeitigen Anpassung des Modells an alle Umwandlungsraten beider Datensätze, wobei nur die relativen Beiträge von kontinuierlicher Keimbildung und bereits existierender Keime für beide Datensätze unabhängig variiert werden dürfen. Diese Methode ermöglicht ebenfalls eine separate kinetische Beschreibung für Keimbildung und Wachstum.

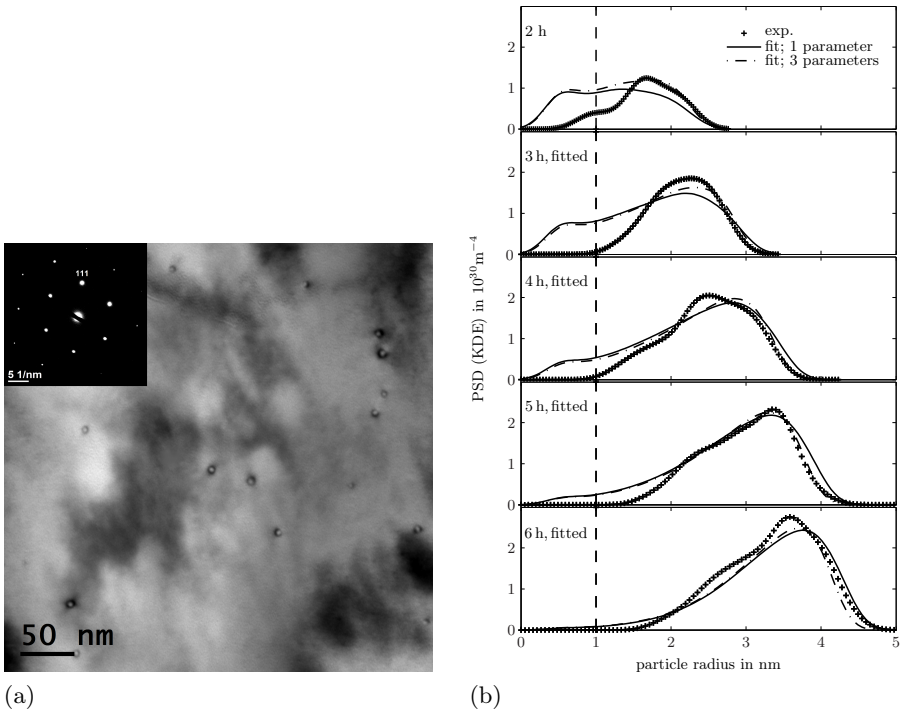


Abbildung 7.6: Die Ausscheidung Co-reicher Teilchen in einer übersättigten Cu-0.6 at.% Co-Legierung bei isothermer Auslagerung (Kapitel 6): (a) TEM Hellfeld-Bild einer Probe nach einer Auslagerungsdauer von 4 h bei 773 K (fcc Cu-(111) Zonenachse; s. eingefügtes Beugungsbild). Eine Anzahl Teilchen mit Radius r zwischen ca. 1.5 nm und 3 nm sind sichtbar. (b) Die zeitliche Entwicklung der Teilchengrößenverteilung bei 773 K (Verteilungen dargestellt durch Kerndichteschätzungen/kernel density estimates). Symbole: experimentell bestimmte Verteilungen. Durchgezogene Linien und Strichpunkt-Linien: Modellanpassungen (mit einem oder drei freien Modellparametern, s. Kapitel 6, Fall A und F). Gestrichelte vertikale Linien: untere Grenze des für die Modellanpassung gewählten Bereichs, zur Berücksichtigung des experimentellen Detektionslimits bei $r \approx 1$ nm [38]. Insbesondere für längere Auslagerungszeiten mit einhergehendem Anstieg der Teilchengröße kann eine gute Übereinstimmung von Modell und experimentellen Daten erreicht werden.

Bibliography

- [1] E. J. Mittemeijer, *Fundamentals of Materials Science*. Springer Verlag, Heidelberg, 2010.
- [2] D. Raabe, *Computational Materials Science*. Wiley-VCH, 1998.
- [3] J. W. Christian, *The Theory of Transformations in Metals and Alloys*. Pergamon Press, 2002.
- [4] J. W. Gibbs, *The Collected Works of J. Willard Gibbs*. Longmans, Green and Co., 1906.
- [5] M. Volmer and A. Weber, “Keimbildung in übersättigten Gebilden,” *Z. Phys. Chem.*, vol. 119, no. 3/4, pp. 277–301, 1926.
- [6] R. Becker and W. Döring, “Kinetische Behandlung der Keimbildung in übersättigten Dämpfen,” *Ann. Phys.*, vol. 24, no. 5, pp. 719–752, 1935.
- [7] D. Turnbull, “Phase Changes,” *Solid State Physics*, vol. 3, pp. 225–306, 1956.
- [8] H. I. Aaronson and F. K. Legoues, “An Assessment of Studies on Homogeneous Diffusional Nucleation Kinetics on Binary Metallic Alloys,” *Metall. Trans. A*, vol. 23, no. 7, pp. 1915–1945, 1992.
- [9] G. Martin, “Reconciling the Classical Nucleation Theory and Atomic Scale Observations and Modeling,” *Adv. Eng. Mater.*, vol. 8, pp. 1231–1236, 2006.
- [10] E. A. Jaegle and E. J. Mittemeijer, “The Kinetics of and the Microstructure Induced by the Recrystallization of Copper,” *Metall. Mater. Trans. A*, vol. 43A, no. 4, pp. 1117–1131, 2012.
- [11] F. Liu, F. Sommer, C. Bos, and E. J. Mittemeijer, “Analysis of Solid State Phase Transformation Kinetics: Models and Recipes,” *Int. Mater. Rev.*, vol. 52, no. 4, pp. 193–212, 2007.
- [12] A. N. Kolmogorov, “Zur Statistik der Kristallisationsvorgänge in Metallen,” *Izv. Akad. Nauk SSSR, M.*, vol. 3, pp. 355–359, 1937.

- [13] M. Avrami, "Kinetics of Phase Change I - General Theory," *J. Chem. Phys.*, vol. 7, no. 12, pp. 1103–1112, 1939.
- [14] W. A. Johnson and R. F. Mehl, "Reaction Kinetics in Processes of Nucleation and Growth," *Trans. Am. Inst. Min. Metall. Eng.*, vol. 135, pp. 416–442, 1939.
- [15] R. Kampmann and R. Wagner in *Decomposition of Alloys: the Early Stages* (P. Haasen, V. Gerold, R. Wagner, and M. F. Ashby, eds.), ch. Kinetics of Precipitation in Metastable Binary Alloys -Theory and Application to Cu 1.9 at.% Ti and Ni 14 at.% Al, pp. 91–103, Pergamon Press, 1984.
- [16] M. F. Ashby, "Physical Modeling of Materials Problems," *Mater. Sci. Technol.*, vol. 8, no. 2, pp. 102–111, 1992.
- [17] C. Bos, F. Sommer, and E. J. Mittemeijer, "An Atomistic Analysis of the Interface Mobility in a Massive Transformation," *Acta Mater.*, vol. 53, no. 20, pp. 5333–5341, 2005.
- [18] M. Avrami, "Kinetics of Phase Change. II. Transformation-Time Relations for Random Distribution of Nuclei," *J. Chem. Phys.*, vol. 8, pp. 212–224, 1940.
- [19] M. Avrami, "Granulation, Phase Change, and Microstructure - Kinetics of Phase Change. III," *J. Chem. Phys.*, vol. 9, no. 2, pp. 177–184, 1941.
- [20] H. E. Kissinger, "Reaction Kinetics in Differential Thermal Analysis," *Anal. Chem.*, vol. 29, no. 11, pp. 1702–1706, 1957.
- [21] A. T. W. Kempen, F. Sommer, and E. J. Mittemeijer, "The Isothermal and Isochronal Kinetics of the Crystallisation of Bulk Amorphous Pd₄₀Cu₃₀P₂₀N₁₀," *Acta Mater.*, vol. 50, no. 6, pp. 1319–1329, 2002.
- [22] K. Fan, F. Liu, X. N. Liu, Y. X. Zhang, G. C. Yang, and Y. H. Zhou, "Modeling of Isothermal Solid-State Precipitation Using an Analytical Treatment of Soft Impingement," *Acta Mater.*, vol. 56, no. 16, pp. 4309–4319, 2008.
- [23] M. J. Starink, "A New Model for Diffusion-Controlled Precipitation Reactions Using the Extended Volume Concept," *Thermochim. Acta*, vol. 596, pp. 109 – 119, 2014.
- [24] F. S. Ham, "Theory of Diffusion-Limited Precipitation," *J. Phys. Chem. Solids*, vol. 6, no. 4, pp. 335–351, 1958.

- [25] C. Zener, "Theory of Growth of Spherical Precipitates from Solid Solution," *J. Appl. Phys.*, vol. 20, no. 10, pp. 950–953, 1949.
- [26] H. B. Aaron, D. Fainstein, and G. R. Kotler, "Diffusion-Limited Phase Transformations - a Comparison and Critical Evaluation of Mathematical Approximations," *J. Appl. Phys.*, vol. 41, no. 11, pp. 4404–4410, 1970.
- [27] A. L. Greer, "Metallic Glasses," *Science*, vol. 267, no. 5206, pp. 1947–1953, 1995.
- [28] M. F. Ashby and A. L. Greer, "Metallic Glasses as Structural Materials," *Scr. Mater.*, vol. 54, no. 3, pp. 321–326, 2006.
- [29] M. Palumbo, S. Curiotto, and L. Battezzati, "Thermodynamic Analysis of the Stable and Metastable Co-Cu and Co-Cu-Fe Phase Diagrams," *CALPHAD: Comput. Coupling Phase Diagrams Thermochem.*, vol. 30, no. 2, pp. 171–178, 2006.
- [30] M. F. Ashby and L. M. Brown, "Diffraction Contrast from Spherically Symmetrical Coherency Strains," *Philos. Mag.*, vol. 8, no. 91, pp. 1083–1103, 1963.
- [31] I. S. Servi and D. Turnbull, "Thermodynamics and Kinetics of Precipitation in the Copper-Cobalt System," *Acta Metall. Mater.*, vol. 14, no. 2, pp. 161–169, 1966.
- [32] F. K. Legoues and H. I. Aaronson, "Influence of Crystallography upon Critical Nucleus Shapes and Kinetics of Homogeneous fcc-fcc Nucleation .4. Comparisons between Theory and Experiment in Cu-Co Alloys," *Acta Metall.*, vol. 32, no. 10, pp. 1855–1864, 1984.
- [33] M. Brey, W. Gust, and B. Predel, "Wachstum und Vergrößerung Co-reicher Ausscheidungsteilchen in verdünnten Cu-Co-Legierungen," *Z. Metallkd.*, vol. 82, pp. 279–288, 1991.
- [34] W. Wagner, "The Influence of Precursor Fluctuations on the Kinetics of α -Co Precipitation in Dilute CuCo Alloys," *Acta Metall. Mater.*, vol. 38, no. 12, pp. 2711–2719, 1990.
- [35] T. Ebel, R. Kampmann, and R. Wagner, "Nucleation in a Cu-0.8 at-percent-Co Alloy - Polarized Neutron-scattering Investigation and Clusterdynamics Description," *J. Phys. IV*, vol. 3, no. C8, pp. 295–298, 1993.

- [36] G. Goerigk, H. G. Haubold, and W. Schilling, "Kinetics of Decomposition in Copper-Cobalt: a Time-Resolved ASAXS Study," *J. Appl. Crystallogr.*, vol. 30, no. 6, pp. 1041–1047, 1997.
- [37] X. D. Jiang, W. Wagner, and H. Wollenberger, "FIM-AP Investigation of the Early Stage of Decomposition in a Cu 0.8 at.% Co Alloy," *Z. Metallkd.*, vol. 82, no. 3, pp. 192–197, 1991.
- [38] R. Hattenhauer and F. Haider, "Improved Imaging of Small Coherent Precipitates by Bright Field Zone Axis Incidence TEM," *Scr. Metall. Mater.*, vol. 25, no. 5, pp. 1173–1178, 1991.
- [39] R. Hattenhauer and P. Haasen, "The Decomposition Kinetics of Cu-1 at. percent-Co at 823 K, Studied by Bright-Field Zone-Axis-Incidence Transmission Electron-Microscopy," *Philos. Mag. A*, vol. 68, no. 6, pp. 1195–1213, 1993.
- [40] R. P. Setna, A. Cerezo, J. M. Hyde, and G. D. W. Smith, "Atomic-Scale Characterization of Precipitation in Copper Cobalt Alloys," *Appl. Surf. Sci.*, vol. 76, no. 1-4, pp. 203–212, 1994.
- [41] A. Heinrich, T. Al-Kassab, and R. Kirchheim, "Investigation of new Aspects in the Initial Stages of Decomposition of Cu 2 at.% Co with the Tomographic Atom Probe and the Field Ion Microscope," *Surf. Interface Anal.*, vol. 39, no. 2-3, Sp. Iss. SI, pp. 240–245, 2007.
- [42] F. K. Legoues, H. I. Aaronson, and Y. W. Lee, "Influence of Crystallography upon Critical Nucleus Shapes and Kinetics of Homogeneous fcc-fcc Nucleation .3. The Influence of Elastic Strain-Energy," *Acta Metall.*, vol. 32, no. 10, pp. 1845–1853, 1984.
- [43] F. K. Legoues, Y. W. Lee, and H. I. Aaronson, "Influence of Crystallography upon Critical Nucleus Shapes and Kinetics of Homogeneous fcc-fcc Nucleation .2. The Non-Classical Regime," *Acta Metall.*, vol. 32, no. 10, pp. 1837–1843, 1984.
- [44] R. Bauer, E. A. Jaegle, W. Baumann, and E. J. Mittemeijer, "Kinetics of the Allotropic hcp-fcc Phase Transformation in Cobalt," *Philos. Mag.*, vol. 91, no. 3, pp. 437–457, 2011.
- [45] E. J. Mittemeijer and F. Sommer, "Solid State Phase Transformation Kinetics: A Modular Transformation Model," *Z. Metallkd.*, vol. 93, no. 5, pp. 352–361, 2002.

- [46] A. T. W. Kempen, H. Nitsche, F. Sommer, and E. J. Mittemeijer, "Crystallization Kinetics of Amorphous Magnesium-Rich Magnesium-Copper and Magnesium-Nickel Alloys," *Metall. Mater. Trans. A*, vol. 33, no. 4, pp. 1041–1050, 2002.
- [47] H. Nitsche, F. Sommer, and E. J. Mittemeijer, "Nucleation and Growth Modes Deduced from Particle Density Distributions: Nanocrystallization of fcc Al in Amorphous $\text{Al}_{85}\text{Ni}_8\text{Y}_5\text{Co}_2$," *Metall. Mater. Trans. A*, vol. 37A, no. 3, pp. 621–632, 2006.
- [48] H. Nitsche, M. Stanislawski, F. Sommer, and E. J. Mittemeijer, "Kinetics of Crystallization of Amorphous $\text{Mg}_{80}\text{Cu}_{10}\text{Y}_{10}$," *Z. Metallkd.*, vol. 96, no. 12, pp. 1341–1350, 2005.
- [49] H. Nitsche, F. Sommer, and E. J. Mittemeijer, "The Al Nano-Crystallization Process in Amorphous $\text{Al}_{85}\text{Ni}_8\text{Y}_5\text{Co}_2$," *J. Non-Cryst. Solids*, vol. 351, no. 49–51, pp. 3760–3771, 2005.
- [50] F. Liu, F. Sommer, and E. J. Mittemeijer, "Determination of Nucleation and Growth Mechanisms of the Crystallization of Amorphous Alloys; Application to Calorimetric Data," *Acta Mater.*, vol. 52, no. 11, pp. 3207–3216, 2004.
- [51] A. T. W. Kempen, F. Sommer, and E. J. Mittemeijer, "The Kinetics of the Austenite-Ferrite Phase Transformation of Fe-Mn: Differential Thermal Analysis during Cooling," *Acta Mater.*, vol. 50, no. 14, pp. 3545–3555, 2002.
- [52] Y. C. Liu, F. Sommer, and E. J. Mittemeijer, "Abnormal Austenite-Ferrite Transformation Behaviour in Substitutional Fe-Based Alloys," *Acta Mater.*, vol. 51, no. 2, pp. 507–519, 2003.
- [53] Y. C. Liu, F. Sommer, and E. J. Mittemeijer, "The Austenite-Ferrite Transformation of Ultralow-Carbon Fe-C Alloy; Transition from Diffusion- to Interface-Controlled Growth," *Acta Mater.*, vol. 54, no. 12, pp. 3383–3393, 2006.
- [54] W. Baumann, A. Leineweber, and E. J. Mittemeijer, "Failure of Kissinger(-like) Methods for Determination of the Activation Energy of Phase Transformations in the Vicinity of the Equilibrium Phase-Transformation Temperature," *J. Mater. Sci.*, vol. 45, no. 22, pp. 6075–6082, 2010.

- [55] T. Nishizawa and K. Ishida, "The Co-Cu (Cobalt-Copper) System," *Bull. Alloy Phase Diagrams*, vol. 5, no. 2, pp. 161–165, 1984.
- [56] V. A. Phillips and J. D. Livingston, "Direct Observation of Coherency Strains in a Copper-Cobalt Alloy," *Philos. Mag.*, vol. 7, no. 78, pp. 969–980, 1962.
- [57] J. B. Hess and C. S. Barrett, "Transformation in Cobalt-Nickel Alloys," *Journal of Metals*, vol. 4, no. 6, pp. 645–647, 1952.
- [58] P. Villars and L. D. Calvert, *Pearson's Handbook of Crystallographic Data for Intermetallic Phases 2*. ASM International, 1996.
- [59] S. Matsumura, M. Toyohara, and Y. Tomokiyo, "Strain Contrast of Coherent Precipitates on Bright-Field Images under Zone Axis Incidence," *Philos. Mag. A*, vol. 62, no. 6, pp. 653–670, 1990.
- [60] J. D. Robson, "Modelling the Evolution of Particle Size Distribution during Nucleation, Growth and Coarsening," *Mater. Sci. Technol.*, vol. 20, no. 4, pp. 441–448, 2004.
- [61] R. Kampmann, T. Ebel, M. Haese, and R. Wagner, "A Combined Cluster-Dynamic and Deterministic Description of Decomposition Kinetics in Binary-Alloys with a Tendency for Clustering," *Phys. Status Solidi B*, vol. 172, no. 1, pp. 295–308, 1992.
- [62] R. P. Setna, J. M. Hyde, A. Cerezo, G. D. W. Smith, and M. F. Chisholm, "Position-Sensitive Atom-Probe Study of the Decomposition of a Cu-2.6at-percent-Co Alloy," *Appl. Surf. Sci.*, vol. 67, no. 1-4, pp. 368–379, 1993.
- [63] E. J. Mittemeijer, "Analysis of the Kinetics of Phase-Transformations," *J. Mater. Sci.*, vol. 27, no. 15, pp. 3977–3987, 1992.
- [64] C. Wert and C. Zener, "Interference of Growing Spherical Precipitate Particles," *J. Appl. Phys.*, vol. 21, no. 1, pp. 5–8, 1950.
- [65] A. T. W. Kempen, F. Sommer, and E. J. Mittemeijer, "Determination and Interpretation of Isothermal and Non-Isothermal Transformation Kinetics; The Effective Activation Energies in Terms of Nucleation and Growth," *J. Mater. Sci.*, vol. 37, no. 7, pp. 1321–1332, 2002.
- [66] R. Egerton, *Electron Energy-Loss Spectroscopy in the Electron Microscope*. Plenum Press, 1996.

- [67] M. B. Berkenpas, J. A. Barnard, R. V. Ramanuian, and H. I. Aaronson, "A Critique of Activation-Energies for Nucleation, Growth and Overall Transformation Kinetics," *Scr. Metall.*, vol. 20, no. 3, pp. 323–328, 1986.
- [68] F. Liu, S. J. Song, F. Sommer, and E. J. Mittemeijer, "Evaluation of the Maximum Transformation Rate for Analyzing Solid-State Phase Transformation Kinetics," *Acta Mater.*, vol. 57, no. 20, pp. 6176–6190, 2009.
- [69] F. Liu, F. Sommer, and E. Mittemeijer, "An Analytical Model for Isothermal and Isochronal Transformation Kinetics," *J. Mater. Sci.*, vol. 39, no. 5, pp. 1621–1634, 2004.
- [70] A. T. Dinsdale, "SGTE Data for Pure Elements," *Calphad*, vol. 15, no. 4, pp. 317–425, 1991.
- [71] D. A. Porter and K. E. Easterling, *Phase Transformations in Metals and Alloys*, 2nd ed. Taylor & Francis Group, 2004.
- [72] M. A. Turchanin and P. G. Agravall, "Phase Equilibria and Thermodynamics of Binary Copper Systems with 3d-Metals. V. Copper - Cobalt System," *Powder Metall. Met. Ceram.*, vol. 46, no. 1-2, pp. 77–89, 2007.
- [73] R. Döhl, M. P. Macht, and V. Naundorf, "Measurement of the Diffusion-Coefficient of Cobalt in Copper," *Phys. Status Solidi A*, vol. 86, no. 2, pp. 603–612, 1984.
- [74] A. Varschavsky and E. Donoso, "DSC Study of Precipitation Processes in Cu-Co-Si Alloys," *J. Therm. Anal. Calorim.*, vol. 74, no. 1, pp. 41–56, 2003.
- [75] E. Donoso, G. Diaz, and J. M. Criado, "Kinetics Analysis of Precipitation in a Quasi-Binary Cu-1 At.% CoTi Alloy," *J. Therm. Anal. Calorim.*, vol. 91, no. 2, pp. 491–495, 2008.
- [76] L. A. Girifalco and H. Herman, "A Model for Growth of Guinier-Preston Zones - Vacancy Pump," *Acta Metall.*, vol. 13, no. 6, pp. 583–590, 1965.
- [77] B. Steffen and G. Liedtke, "X-ray-Investigation of the Crystallization of the Metallic Glass Fe₄₀Ni₄₀B₂₀," *Z. Metallkd.*, vol. 72, no. 12, pp. 849–853, 1981.
- [78] G. Fagherazzi, S. Polizzi, P. Riello, and A. Benedetti, "XRD Investigation of the Crystallization Process in Fe₄₀Ni₄₀B₂₀ Metallic Glass," *Journal of Non-crystalline Solids*, vol. 151, no. 1-2, pp. 59–65, 1992.

- [79] K. Müller and M. von Heimendahl, “TEM Investigation of Crystallization Phenomena in the Metallic Glass Vitrovac 0040 ($\text{Fe}_{40}\text{Ni}_{40}\text{B}_{20}$),” *J. Mater. Sci.*, vol. 17, no. 9, pp. 2525–2532, 1982.
- [80] V. S. Raja, Kishore, and S. Ranganathan, “Microstructural and Kinetic Aspects of Devitrification of $\text{Fe}_{40}\text{Ni}_{40}\text{B}_{20}$ Metallic-Glass,” *J. Mater. Sci.*, vol. 25, no. 11, pp. 4667–4677, 1990.
- [81] P. Duhaj and P. Svec, “Transmission Electron-microscopy Study of Crystallization in Amorphous $\text{Fe}_{40}\text{Ni}_{40}\text{B}_{20}$ Alloy,” *Phys. Status Solidi A*, vol. 80, no. 1, pp. 231–236, 1983.
- [82] G. Wei and B. Cantor, “The Effect of Heat-Treatment and Surface-Treatment on the Crystallization Behavior of Amorphous $\text{Fe}_{40}\text{Ni}_{40}\text{B}_{20}$,” *Acta Metall.*, vol. 37, no. 12, pp. 3409–3424, 1989.
- [83] R. S. Debiiasi and A. A. R. Fernandes, “Crystallization of the Amorphous Alloy $\text{Fe}_{40}\text{Ni}_{40}\text{B}_{20}$ - A Ferromagnetic-Resonance Study,” *J. Mater. Sci.*, vol. 24, no. 1, pp. 41–44, 1989.
- [84] F. Liu, S. J. Song, F. Sommer, and E. J. Mittemeijer, “Evaluation of the Maximum Transformation Rate for Analyzing Solid-State Phase Transformation Kinetics (vol 57, pg 6176, 2009),” *Acta Mater.*, vol. 58, no. 6, pp. 2291–2291, 2010.
- [85] A. Coelho, “TOPAS: General Profile and Structure Analysis Software for Powder Diffraction Data.” Bruker AXS GmbH, Karlsruhe.
- [86] J. Horvath and H. Mehrer, “Tracer Diffusion of Fe-59 in Amorphous $\text{Fe}_{40}\text{Ni}_{40}\text{B}_{20}$,” *Cryst. Lattice Defects and Amorphous Mater.*, vol. 13, no. 1, pp. 1–14, 1986.
- [87] A. K. Tyagi, M. P. Macht, and V. Naundorf, “Diffusion-Coefficients of Ni-63 in $\text{Fe}_{40}\text{Ni}_{40}\text{B}_{20}$ Metallic-Glass,” *Acta Metall. Mater.*, vol. 39, no. 4, pp. 609–617, 1991.
- [88] J. W. Cahn, “The Kinetics of Cellular Segregation Reactions,” *Acta Metall.*, vol. 7, no. 1, pp. 18–28, 1959.
- [89] B. Rheingans, Y. Ma, F. Liu, and E. J. Mittemeijer, “Crystallisation Kinetics of $\text{Fe}_{40}\text{Ni}_{40}\text{B}_{20}$ Amorphous Alloy,” *J. Non-Cryst. Solids*, vol. 362, pp. 222–230, 2013.

- [90] E. J. Mittemeijer and F. Sommer, "Solid State Phase Transformation Kinetics: Evaluation of the Modular Transformation Model," *Int. J. Mater. Res.*, vol. 102, no. 7, pp. 784–795, 2011.
- [91] E. A. Jäggle and E. J. Mittemeijer, "Interplay of Kinetics and Microstructure in the Recrystallization of Pure Copper: Comparing Mesoscopic Simulations and Experiments," *Metall. Mater. Trans. A*, vol. 43A, no. 7, pp. 2534–2551, 2012.
- [92] G. B. Olson and M. Cohen, "General Mechanism of Martensitic Nucleation .1. General Concepts and fcc-hcp Transformation," *Metall. Trans. A*, vol. 7, no. 12, pp. 1897–1904, 1976.
- [93] M. F. Lin, G. B. Olson, and M. Cohen, "Distributed-Activation Kinetics of Heterogeneous Martensitic Nucleation," *Metall. Mater. Trans. A*, vol. 23, no. 11, pp. 2987–2998, 1992.
- [94] R. Bauer, B. Rheingans, and E. J. Mittemeijer, "The Kinetics of the Precipitation of Co from Supersaturated Cu-Co Alloy," *Metall. Mater. Trans. A*, vol. 42A, pp. 1750–1759, 2011.
- [95] E. A. Jäggle and E. J. Mittemeijer, "Predicting Microstructures from Phase Transformation Kinetics: The Case of Isochronal Heating and Cooling from a Supersaturated Matrix," *Model Simul Mater Sc*, vol. 18, p. 065010, 2010.
- [96] J. D. Robson, "Modelling the Overlap of Nucleation, Growth and Coarsening during Precipitation," *Acta Mater.*, vol. 52, no. 15, pp. 4669–4676, 2004.
- [97] M. Perez, "Gibbs-Thomson Effects in Phase Transformations," *Scr. Mater.*, vol. 52, no. 8, pp. 709–712, 2005.
- [98] Q. Du, W. J. Poole, and M. A. Wells, "A Mathematical Model Coupled to CALPHAD to Predict Precipitation Kinetics for Multicomponent Aluminum Alloys," *Acta Mater.*, vol. 60, no. 9, pp. 3830–3839, 2012.
- [99] L. Rougier, A. Jacot, C.-A. Gandin, P. Di Napoli, P.-Y. Thery, D. Ponsen, and V. Jaquet, "Numerical Simulation of Precipitation in Multicomponent Ni-base Alloys," *Acta Mater.*, vol. 61, no. 17, pp. 6396–6405, 2013.
- [100] Q. Chen, J. Jeppsson, and J. Ågren, "Analytical Treatment of Diffusion During Precipitate Growth in Multicomponent Systems," *Acta Mater.*, vol. 56, no. 8, pp. 1890–1896, 2008.

- [101] R. Wagner, R. Kampmann, and P. W. Voorhees, “Homogeneous Second Phase Precipitation,” in *Phase Transformations in Materials* (G. Kostorz, ed.), ch. 5 Homogeneous Second Phase Precipitation, pp. 309–408, Wiley-VCH, 2001.
- [102] B. Sundman, B. Jansson, and J. O. Andersson, “The Thermo-Calc Databank System,” *CALPHAD: Comput. Coupling Phase Diagrams Thermochem.*, vol. 9, no. 2, pp. 153–190, 1985.
- [103] M. Hillert, “Application of Gibbs Energy-Composition Diagrams,” in *Lectures on the Theory of Phase Transformations (1975), 2nd Edition* (H. I. Aaronson, ed.), ch. 1, pp. 1–33, The Minerals, Metals and Materials Society, 1999.
- [104] S. Shahandeh and S. Nategh, “A Computational Thermodynamics Approach to the Gibbs-Thomson Effect,” *Mater. Sci. Eng. A*, vol. 443, no. 1-2, pp. 178–184, 2007.
- [105] Q. Du, M. Perez, W. J. Poole, and M. Wells, “Numerical Integration of the Gibbs-Thomson Equation for Multicomponent Systems,” *Scr. Mater.*, vol. 66, no. 7, pp. 419–422, 2012.
- [106] Thermo-Calc Software AB, Stockholm, Sweden, “TC-PRISMA User’s Guide and Examples, Version 2.0,” 2013.
- [107] J. Svoboda, F. D. Fischer, P. Fratzl, and E. Kozeschnik, “Modelling of Kinetics in Multi-Component Multi-Phase Systems with Spherical Precipitates - I: Theory,” *Mater. Sci. Eng. A*, vol. 385, no. 1-2, pp. 166–174, 2004.
- [108] D. den Ouden, F. J. Vermolen, L. Zhao, C. Vuik, and J. Sietsma, “Modelling of Particle Nucleation and Growth in Binary Alloys under Elastic Deformation: An Application to a Cu-0.95 wt%Co Alloy,” *Comput. Mater. Sci.*, vol. 50, no. 8, pp. 2397–2410, 2011.
- [109] Z. Liu, V. Mohles, O. Engler, and G. Gottstein, “Thermodynamics Based Modelling of the Precipitation Kinetics in Commercial Aluminium Alloys,” *Comput. Mater. Sci.*, vol. 81, pp. 410–417, 2014.
- [110] M. Hillert and J. Ågren, “Effect of Surface Free Energy and Surface Stress on Phase Equilibria,” *Acta Mater.*, vol. 50, no. 9, pp. 2429–2441, 2002.
- [111] M. Hillert, *Phase Equilibria, Phase Diagrams and Phase Transformations, 2nd Edition*. Cambridge University Press, 2008.

- [112] H. I. Aaronson, M. Enomoto, and J. K. Lee, *Mechanisms of Diffusional Phase Transformations in Metals and Alloys*. CRC Press, 2010.
- [113] W. W. Mullins, “Thermodynamic Equilibrium of a Crystalline Sphere in a Fluid,” *J. Chem. Phys.*, vol. 81, no. 3, pp. 1436–1442, 1984.
- [114] J. W. Cahn and F. Larché, “Surface Stress and the Chemical Equilibrium of Small Crystals - II. Solid Particles Embedded in a Solid Matrix,” *Acta Metall. Mater.*, vol. 30, pp. 51–56, 1982.
- [115] C. Rottman, P. W. Voorhees, and W. C. Johnson, “The Gibbs-Thomson Equation for a Spherical Coherent Precipitate with Applications to Nucleation,” *Scr. Metall. Mater.*, vol. 22, pp. 293–298, 1988.
- [116] M. Qian, “The Gibbs-Thomson Effect in Dilute Binary Systems,” *Metall. Mater. Trans. A*, vol. 33, no. 4, pp. 1283–1287, 2002.
- [117] B. Rheingans and E. J. Mittemeijer, “Analysis of Precipitation Kinetics on the Basis of Particle-Size Distributions,” *under review*.
- [118] X. G. Lu, M. Selleby, and B. Sundman, “Assessments of Molar Volume and Thermal Expansion for Selected bcc, fcc and hcp Metallic Elements,” *CALPHAD: Comput. Coupling Phase Diagrams Thermochem.*, vol. 29, no. 1, pp. 68–89, 2005.
- [119] J. D. Eshelby, “The Continuum Theory of Lattice Defects,” *Solid State Phys.*, vol. 3, pp. 79–144, 1956.
- [120] Y. A. Chang and L. Himmel, “Temperature Dependence of Elastic Constants of Cu, Ag and Au above Room Temperature,” *J. Appl. Phys.*, vol. 37, no. 9, pp. 3567–3572, 1966.
- [121] B. Strauss, F. Frey, W. Petry, J. Trampenau, K. Nicolaus, S. Shapiro, and J. Bossy, “Martensitic Phase Transformation and Lattice Dynamics of fcc Cobalt,” *Phys. Rev. B*, vol. 54, no. 9, pp. 6035–6038, 1996.
- [122] B. Rheingans and E. J. Mittemeijer, “Modelling Precipitation Kinetics: Evaluation of the Thermodynamics of Nucleation and Growth,” *under review*.
- [123] M. Takeda, N. Suzuki, G. Shinohara, T. Endo, and J. van Landuyt, “TEM Study on Precipitation Behavior in Cu-Co Alloys,” *Phys. Status Solidi A*, vol. 168, no. 1, pp. 27–35, 1998.

- [124] M. J. Stowell, "Precipitate Nucleation: Does Capillarity Theory Work?," *Mater. Sci. Technol.*, vol. 18, no. 2, pp. 139–144, 2002.
- [125] J. D. Robson and M. J. Stowell, "The Maximum Precipitate Density," *Philos. Mag.*, vol. 84, no. 29, pp. 3101–3115, 2004.
- [126] J. Feder, K. C. Russell, J. Lothe, and G. M. Pound, "Homogeneous Nucleation and Growth of Droplets in Vapours," *Adv. Phys.*, vol. 15, no. 57, pp. 111–178, 1966.
- [127] M. Perez, M. Dumont, and D. Acevedo-Reyes, "Implementation of Classical Nucleation and Growth Theories for Precipitation," *Acta Mater.*, vol. 56, no. 9, pp. 2119–2132, 2008.
- [128] T. Malis, S. C. Cheng, and R. F. Egerton, "EELS Log-Ratio Technique for Specimen-Thickness Measurement in the TEM," *J. Electron. Microsc. Tech.*, vol. 8, no. 2, pp. 193–200, 1988.
- [129] Y. W. Lee, K. C. Russell, and H. I. Aaronson, "On the Evaluation of the Molar Regular Solution Constant," *Scr. Metall.*, vol. 15, no. 7, pp. 723–726, 1981.
- [130] G. J. Shiflet, Y. W. Lee, H. I. Aaronson, and K. C. Russell, "A Reassessment of the Comparison of Classical Homogeneous Nucleation Theory and Experiment in Cu-Co Alloys," *Scr. Metall.*, vol. 15, no. 7, pp. 719–722, 1981.
- [131] Y. Ma, B. Rheingans, F. Liu, and E. J. Mittemeijer, "Isochronal Crystallization Kinetics of Fe₄₀Ni₄₀B₂₀ Amorphous Alloy," *J. Mater. Sci.*, vol. 48, pp. 5596–5606, 2013.
- [132] B. Rheingans and E. J. Mittemeijer, "Phase Transformation Kinetics: Advanced Modeling Strategies," *JOM*, vol. 65, pp. 1145–1154, 2013.
- [133] J. D. Robson, M. J. Jones, and P. B. Prangnell, "Extension of the N-model to Predict Competing Homogeneous and Heterogeneous Precipitation in Al-Sc Alloys," *Acta Mater.*, vol. 51, no. 5, pp. 1453–1468, 2003.
- [134] A. Heinrich, *Zum Einfluss der elastischen Verzerrungsenergie auf die Frühstadien der Entmischung von Cu 2 at.% Co*. PhD thesis, Georg-August-Universität zu Göttingen, 2005.

List of Publications

1. R. Bauer, B. Rheingans, and E. J. Mittemeijer, "The Kinetics of the Precipitation of Co from Supersaturated Cu-Co Alloy," *Metall. Mater. Trans. A*, vol. 42A, pp. 1750–1759, 2011. (*Chapter 2 of this thesis*)
2. B. Rheingans, Y. Ma, F. Liu, and E. J. Mittemeijer, "Crystallisation Kinetics of Fe₄₀Ni₄₀B₂₀ Amorphous Alloy," *J. Non-Cryst. Solids*, vol. 362, pp. 222–230, 2013. (*Chapter 3 of this thesis*)
3. S. R. Meka, E. Bischoff, B. Rheingans, and E. J. Mittemeijer, "Octapod-Shaped, Nanosized, Amorphous Precipitates in a Crystalline Ferrite Matrix," *Philos. Mag. Lett.*, vol. 93, no. 4, pp. 238–245, 2013.
4. Y. Ma, B. Rheingans, F. Liu, and E. J. Mittemeijer, "Isochronal Crystallization Kinetics of Fe₄₀Ni₄₀B₂₀ Amorphous Alloy," *J. Mater. Sci.*, vol. 48, pp. 5596–5606, 2013.
5. B. Rheingans and E. J. Mittemeijer, "Phase Transformation Kinetics: Advanced Modeling Strategies," *JOM*, vol. 65, pp. 1145–1154, 2013. (*Chapter 4 of this thesis*)
6. J. Stein, R. E. Schacherl, M. Jung, S. R. Meka, B. Rheingans, and E. J. Mittemeijer, "Solubility of Nitrogen in Ferrite; The Fe-N Phase Diagram," *Int. J. Mater. Res.*, vol. 104, no. 11, pp. 1053–1065, 2013.
7. S. Löwy, B. Rheingans, S. R. Meka, and E. J. Mittemeijer, "Unusual Martensite-Formation Kinetics in Steels: Observation of Discontinuous Transformation Rates," *Acta Mater.*, vol. 64, pp. 93–99, 2014.
8. B. Rheingans and E. J. Mittemeijer, "Modelling Precipitation Kinetics: Evaluation of the Thermodynamics of Nucleation and Growth," *under review*. (*Chapter 5 of this thesis*)
9. M. Jung, S. R. Meka, B. Rheingans, and E. J. Mittemeijer, "Coupling Inward Diffusion and Precipitation Kinetics; the Case of Nitriding Iron-based Alloys," *under review*.
10. B. Rheingans and E. J. Mittemeijer, "Analysis of Precipitation Kinetics on the Basis of Particle-Size Distributions," *under review*. (*Chapter 6 of this thesis*)

Danksagung

Diese Arbeit entstand am Institut für Materialwissenschaft der Universität Stuttgart und am Max-Planck-Institut für Intelligente Systeme (ehemals Max-Planck-Institut für Metallforschung), Stuttgart. Zum Ende dieser Arbeit möchte ich die Gelegenheit nutzen mich bei allen zu bedanken, die zu ihrem Gelingen beigetragen haben.

An erster Stelle möchte ich mich bei Herrn Prof. Dr. Ir. E. J. Mittemeijer für die Überlassung des Themas meiner Doktorarbeit bedanken, für sein Engagement und seine Unterstützung, und nicht zuletzt auch dafür, mich im Rahmen dieses Themas meinen Weg finden zu lassen und mir dabei immer zu vermitteln, dass auch das was länger währt, zu einem guten Ende führen wird. Unsere ausgiebigen Diskussionen, von der wissenschaftlichen Arbeit bis hin zu den Feinheiten einer Formulierung, werden mir stets in guter Erinnerung bleiben.

Herrn Prof. Dr. Dr. h.c. G. Schmitz danke ich sehr für die freundliche Übernahme des Mitberichts und Herrn Prof. Dr. Th. Schleid für die ebenso freundliche Übernahme des Prüfungsvorsitzes.

Mein Dank gilt auch den Mitarbeitern des Max-Planck-Instituts für Intelligente Systeme und des Instituts für Materialwissenschaft, insbesondere meinen Kollegen aus der Abteilung Mittemeijer, für ihre Unterstützung und die angenehme Arbeitsatmosphäre. Namentlich bedanken möchte ich mich bei Eric Jäggle und Sairam Meka für ausgedehnte wissenschaftliche Diskussionen, auch über materialwissenschaftliche Themen hinaus, bei Ute Schestag für ihre moralische und tatkräftige praktische Unterstützung (du hast es doch vor mir geschafft...) und bei Katharina, Martin, Silke und Holger (für alles).

Zu guter Letzt möchte ich mich bei meinen Freunden (Überschneidungen mit dem oben genannten Personenkreis sind nicht gänzlich ausgeschlossen...) und meiner Familie bedanken, die meine "work-life balance" immer in die jeweils richtige Richtung zu verschieben wussten.

Curriculum Vitae

Persönliche Angaben

Geburtsdatum	14.06.1983
Geburtsort	Backnang
Nationalität	deutsch

Schulische Bildung

1990 – 1994	Grundschule Rudersberg
1994 – 2003	Limes-Gymnasium Welzheim

Universitäre Bildung

2004 – 2009	Universität Stuttgart, Studiengang Werkstoffwissenschaft mit Abschluss Diplom-Ingenieur
04/2009 – 09/2009	Diplomarbeit am Institut für Materialwissenschaft, 1. Lehrstuhl Prof. Dr. Ir. E. J. Mittemeijer; Thema “Kinetics of Cobalt Precipitation in Copper Cobalt Alloys”

Promotion

11/2009 – 12/2010	Max-Planck-Institut für Metallforschung, Stuttgart, und
01/2011 – 2015	Universität Stuttgart, Institut für Materialwissenschaft, 1. Lehrstuhl; Promotion zum Dr. rer. nat. über das Thema “Kinetics of Phase Transformations” bei Prof. Dr. Ir. E. J. Mittemeijer

Erklärung über die Eigenständigkeit der Dissertation

Ich versichere, dass ich die vorliegende Arbeit mit dem Titel *Kinetics of Phase Transformations* selbständig verfasst und keine anderen als die angegebenen Quellen und Hilfsmittel benutzt habe; aus fremden Quellen entnommene Passagen und Gedanken sind als solche kenntlich gemacht.

Declaration of Authorship

I hereby certify that the dissertation entitled *Kinetics of Phase Transformations* is entirely my own work except where otherwise indicated. Passages and ideas from other sources have been clearly indicated.

Name/Name: _____

Unterschrift/Signed: _____

Datum/Date: _____